IVW - Schriftenreihe Band 71

Institut für Verbundwerkstoffe GmbH - Kaiserslautern

Jinglei Yang

Characterization, Modeling and Prediction of the Creep Resistance of Polymer Nanocomposites

Characterization, Modeling and Prediction of the Creep Resistance of Polymer Nanocomposites

Beim Fachbereich für Maschinenbau und Verfahrenstechnik
der Technischen Universität Kaiserslautern
vorgelegte Dissertation
zur Erlangung des akademischen Grades

Doktor-Ingenieur (Dr.-Ing.)

von

M.Sc. Jinglei Yang

aus Handan, China

Tag der mündlichen Prüfung: 30 Mai 2006

Prüfungsvorsitzender: Prof. Dr.-Ing. Dieter H. Hellmann
1. Berichterstatter: Prof. Dr.-Ing. Dr. h.c. Klaus Friedrich
2. Berichterstatter: Prof. Dr. Zhong Zhang

D386

Acknowledgements

Kaiserslautern, June 2006   Jinglei Yang

Table of Contents

Abstract

The broad engineering applications of polymers and composites have become the state of the art due to their numerous advantages over metals and alloys, such as lightweight, easy processing and manufacturing, as well as acceptable mechanical properties. However, a general deficiency of thermoplastics is their relatively poor creep resistance, impairing service durability and safety, which is a significant barrier to further their potential applications. In recent years, polymer nanocomposites have been increasingly focused as a novel field in materials science. There are still many scientific questions concerning these materials leading to the optimal property combinations. The major task of the current work is to study the improved creep resistance of thermoplastics filled with various nanoparticles and multi-walled carbon nanotubes.

A systematic study of three different nanocomposite systems by means of experimental observation and modeling and prediction was carried out. In the first part, a nanoparticle/PA system was prepared to undergo creep tests under different stress levels (20, 30, 40 MPa) at various temperatures (23, 50, 80 °C). The aim was to understand the effect of different nanoparticles on creep performance. 1 vol. % of 300 nm and 21 nm TiO_2 nanoparticles and nanoclay was considered. Surface modified 21 nm TiO_2 particles were also investigated. Static tensile tests were conducted at those temperatures accordingly. It was found that creep resistance was significantly enhanced to different degrees by the nanoparticles, without sacrificing static tensile properties. Creep was characterized by isochronous stress-strain curves, creep rate, and creep compliance under different temperatures and stress levels. Orientational hardening, as well as thermally and stress activated processes were briefly introduced to further understanding of the creep mechanisms of these nanocomposites.

The second material system was PP filled with 1 vol. % 300 nm and 21 nm TiO_2 nanoparticles, which was used to obtain more information about the effect of particle size on creep behavior based on another matrix material with much lower T_g. It was found especially that small nanoparticles could significantly improve creep resistance. Additionally, creep lifetime under high stress levels was noticeably extended by smaller nanoparticles. The improvement in creep resistance was attributed to a very dense network formed by the small particles that effectively restricted the mobility of polymer chains. Changes in the spherulite morphology and crystallinity in specimens before and after creep tests confirmed this explanation.

In the third material system, the objective was to explore the creep behavior of PP reinforced with multi-walled carbon nanotubes. Short and long aspect ratio nanotubes with 1 vol. % were used. It was found that nanotubes markedly improved the creep resistance of the matrix, with reduced creep deformation and rate. In addition, the creep lifetime of the composites was dramatically extended by 1,000 % at elevated temperatures. This enhancement contributed to efficient load transfer between carbon nanotubes and surrounding polymer chains.

Finally, a modeling analysis and prediction of long-term creep behaviors presented a comprehensive understanding of creep in the materials studied here. Both the Burgers model and Findley power law were applied to satisfactorily simulate the experimental data. The parameter analysis based on Burgers model provided an explanation of structure-to-property relationships. Due to their intrinsic difference, the power law was more capable of predicting long-term behaviors than Burgers model. The time-temperature-stress superposition principle was adopted to predict long-term creep performance based on the short-term experimental data, to make it possible to forecast the future performance of materials.

Kurzfassung

Die breite Anwendung von Polymeren und deren Verbunden hat sich mittlerweile durchgesetzt, wegen einer Vielzahl an Vorteilen gegenüber Metallen und deren Legierungen. Als Vorzüge der Kunststoffe sind insbesondere die geringen Bauteilgewichte, eine einfache Verarbeitung und Herstellung bei akzeptablen mechanischen Eigenschaften zu nennen.

Leider ist der vergleichsweise schlechte Kriechwiderstand von Thermoplasten ein Nachteil, wodurch die Betriebsdauer und -sicherheit von Bauteilen beeinträchtigt und damit auch die weitere Anwendung verhindert wird.

In den letzten Jahren haben Nanokomposite die Aufmerksamkeit der Forschungsgemeinschaft auf sich gezogen. Doch sind immer noch wissenschaftliche Fragestellungen bezüglich der sich einstellenden optimalen Eigenschaftskombinationen offen. Die Hauptaufgabe der vorliegenden Arbeit ist die Analyse des verbesserten Kriechwiderstandes thermoplastischer Komposite, die mit verschiedenen Nanopartikeln und Multi-Wall Carbon Nanotubes verstärkt sind.

Eine systematische Studie von drei verschiedenen Nanokomposite-Systemen wurde durchgeführt, wobei die experimentellen Ergebnisse modelliert und das Materialverhalten vorhergesagt wurde.

Im ersten Teil wurde ein PA/Nanopartikel System in Kriechversuchen bei verschiedenen Spannungen (20, 30, 40 MPa) und verschiedenen Temperaturen (23, 50, 80°C) untersucht. Hier sollte der Einfluß von verschiedenen Nanopartikeln auf das Kriechverhalten analysiert werden. Verglichen wurden 1 vol. % von 300 nm und 21 nm großen TiO_2 Nanopartikel, sowie Nanoclay. Oberflächenmodifiziertes TiO_2 mit einer Partikelgröße von 21 nm wurde ebenfalls betrachtet.

Quasi-statische Zugversuche wurden bei den entsprechenden Temperaturen

durchgeführt. Es wurde festgestellt, daß der Kriechwiderstand durch die Nanopartikel in unterschiedlicher Ausprägung verbessert werden konnte, ohne zu Einbußen in den statischen mechanischen Eigenschaften zu führen.

Das Kriechen wurde durch isochrone Spannungs-Dehnungskurven, Kriechgeschwindigkeiten und Kriechnachgiebigkeiten bei verschiedenen Temperaturen und Spannungsleveln charakterisiert. Orientierungsbedingte Verfestigung sowie thermisch und spannungsbedingte Aktivierungsprozesse wurde betrachtet, um die Kriechmechanismen der Nanokomposite zu deuten.

Das zweite Materialsystem war PP, gefüllt mit 1 vol. % 300 nm und 21 nm großen TiO_2 Nanopartikeln. Hier sollten mehr Informationen über den Einfluß der Partikelgröße beim Kriechen an einem weiteren Matrixmaterial gesammelt werden, welches aber eine sehr viel niedrigere Glasübergangstemperatur T_g besitzt. Es stellte sich heraus, daß besonders die kleineren Nanopartikel das Kriechverhalten signifikant verbessern konnten.

Besonders die Standzeit bei hohen Spannungsniveaus konnte durch die kleineren Nanopartikel erhöht werden. Die Verbesserung des Kriechwiderstandes wurde einem dichten Partikelnetzwerk zugeschrieben, welches effektiv die Mobilität der Polymerketten einschränkte. Veränderungen in der spherolithischen Morphologie und Kristallinität vor und nach den Kriechversuchen bestätigten diese Erklärung.

In einem dritten Materialsystem wurde das Kriechverhalten von PP verstärkt mit Multi-Wall Carbon Nanotubes untersucht. Unterschiedliche Aspektverhältnisse der Nanotubes wurden bei einem Füllstoffgehalt von 1 vol. % eingesetzt. Es stellte sich heraus, daß die Nanotubes zu außergewöhnlichen Verbesserungen des Kriechwiderstandes bei reduzierter Kriechgeschwindigkeit und Kriechdeformation führen. Besonders die Standzeit der Komposite wurde um 1000% bei erhöhten Temperaturen verbessert. Diese Steigerung wurde der effizienten Lastübertragung zwischen den Carbon Nanotubes und den umgebenden Polymerketten

zugeschrieben.

Abschließend wurde eine Modellierung und Vorhersagemöglichkeit des Langzeit-Kriechverhaltens entwickelt. Zwei Materialmodelle, das Burger-Modell und das Potenzgesetz von Findley, konnten die experimentellen Daten zufriedenstellend simulieren. Eine Parameter-Analyse auf Basis des Burgers-Modell erklärte Struktur-Eigenschaftsbeziehungen. Dennoch konnte das Potenzgesetz von Findley aufgrund intrinsischer Eigenheiten das Langzeit-Kriechverhalten besser vorhersagen als das Burgers-Modell. Das Zeit-Temperatur-Spannungs-Superpositionsprinzip wurde angewandt, um das zeitaufwendige Langzeitkriechverhalten auf der Basis von Kurzzeit-Kriechversuchen vorherzusagen.

List of Abbreviations and Symbols

Abbreviation	
1-, 2-, 3-D	1-, 2-, 3-dimention
CNT	Carbon nanotube
DMTA	Dynamic-mechanical-thermo analyzer
DSC	Differential scanning calorimeter
LM	Light microscope
HDPE	High density polyethylene
LVE	Linear viscoelasticity
NLVE	Nonlinear viscoelasticity
MLS	Montmorillonite layered silicate
MWNT	Multiwalled carbon nanotube
PA or PA66	Polyamide 6,6
PA6	Polyamide 6
PC	Polycarbonate
PCC	Precipitated $CaCO_3$
PE	Polyethylene
PET	Polyethylene terephthalate
PMMA	Poly(methyl methacrylate)
PNC	Polymer nanocomposites
PP	Polypropylene
PS	Polystyrene
RD	Relative deviation
SEM	Scanning electron microscope

sSEBS		Sulfonated poly(styrene-b-ethylene/butylene-b-styrene
SWNT		Single-walled carbon nanotubes
TEM		Transmission electron microscope
TTSSP		Time-temperature-stress superposition principle
TTSP		Time-temperature superposition principle
TSSP		Time-stress superposition principle
UTS		Ultimate tensile strength
XRD		X-ray diffraction

Symbols

A, B		Material constants in Doolittle equation
C_1, C_2, C_3		Constants in TTSSP equation
d	[nm]	Interparticle distance
D	[nm]	Nanoparticle diameter
d'		Ratio of d/D
E_{E1}, E_{E2}	[MPa]	Modulus of the spring in the Eyring model
$E_{tensile}$	[MPa]	Young's modulus from static tensile test
E_K	[MPa]	Modulus of the Kelvin spring in the Burgers model
E_M	[MPa]	Modulus of the Maxwell spring in the Burgers model
f		Fractional free volume
f_{ref}		Fractional free volume at the reference state
ΔH	[kJ/mol]	activation energy of Eyring dashpot
k	[J/K]	Boltzmann constant, 1.38×10^{-23} J/K
n		Power in the Findley power law equation

R	[J/mol·K]	Universal gas constant, 8.31J/mol·K
t	[hour]	Time
T	[K]	Absolute temperature
T_g	[°C]	Glass transition temperature
T_{ref}	[°C]	Reference temperature
a_σ		Stress shift factor
a_T		Temperature shift factor
$a_{T\sigma}$		Temperature-stress shift factor
a_σ^T		Stress shift factor at a constant temperature
a_T^σ		Temperature shift factor under a constant stress level
Tan δ		Mechanical loss factor in DMTA test
ε_B		Strain of the Burgers model
ε_F		Strain of the Findley power law model
ε_{F0}		Time-independent strain in the Findley power law model
ε_{F1}		Time-dependent term in the Findley power law model
ε_K		Strain of the Kelvin unit in the Burgers model
ε_{M1}		Strain of the Maxwell spring in the Burgers model
ε_{M2}		Strain of the Maxwell dashpot in the Burgers model
$\dot{\varepsilon}_{II}$	[hour^{-1}]	Fitting strain rate from the secondary creep stage
$\dot{\varepsilon}_B$	[hour^{-1}]	Strain rate of the Burgers model
$\dot{\varepsilon}_E$	[hour^{-1}]	Strain rate of Eyring creep process
$\dot{\varepsilon}_{E0}$	[hour^{-1}]	Constant pre-exponential factor in equation (8)
$\dot{\varepsilon}_F$	[hour^{-1}]	Strain rate of the Findley power law model

$\dot{\varepsilon}_K$	[hour^{-1}]	Strain rate of the Kelvin dashpot in the Burgers model
$\dot{\varepsilon}_{M2}$	[hour^{-1}]	Strain rate of the Maxwell dashpot in the Burgers model
η	[MPa·hour]	Viscosity of material
η_K	[MPa·hour]	Viscosity of the Kelvin dashpot in the Burger model
η_M	[MPa·hour]	Viscosity of the Maxwell dashpot in the Burger model
σ	[MPa]	Stress
σ_0	[MPa]	Initial creep stress
σ_{ref}	[MPa]	Reference stress
τ	[hour]	Retardation time of the Kelvin unit in the Burgers model
υ	[nm^3]	Activation volume in stress activated Eyring process
ρ		Volume content of filler

1   State of the Art

1.1   Introduction

Materials exhibit a great variety of behavior. The design of modern high stability and reliability structures often must take into account the effect of complex states of stress, strain and environment on the mechanical behavior of different classes of materials [1]. Creep is a slow and continuous time-dependent deformation, which takes place under constant stress or load [1,2]. It can result in functional failure or, even worse, catastrophic rupture, and thus is an essential consideration in long-term reliable design of structural materials. The creep problems of metals/alloys [3-11] and polymers and their traditional composites [1,2,12-23] have been widely and deeply studied. However, rapid development of promising nanocomposites [24-40] has brought about new problems concerning stability and reliability in potential applications. This chapter provides a preliminary overview of creep and nanometric fillers and a review of the developments in this field over the last few decades. Special emphasis is placed on the "nano-effects" of nanofillers and recent efforts regarding time-dependent behaviors of polymer-based composites filled with nanoparticles, nanoclay and nanotubes. This has been becoming an important topic in scientific research and receiving considerable attention recently.

A completed creep curve is schematically shown in Figure 1.1 together with creep rate $\dot{\varepsilon}$. Creep can generally be described in terms of three different stages. Before creep, there is an instantaneous elongation (ε_0), which is due to the elastic or plastic deformation of the polymer once the external load is applied; this process is naturally independent of time. The first stage is called primary creep (ε_1), where the creep strain increases noticeably at the beginning and then slowly; the creep rate begins at a relatively high value and decreases rapidly with time, which may be due to the slippage and orientation of polymer chains under persistent stress. After a certain period, the creep strain increases with a minimum constant creep rate in the secondary creep stage, in which viscoelastic flow occurs in the polymer, and the duration is extremely long if under low stress. Finally, the material falls into the
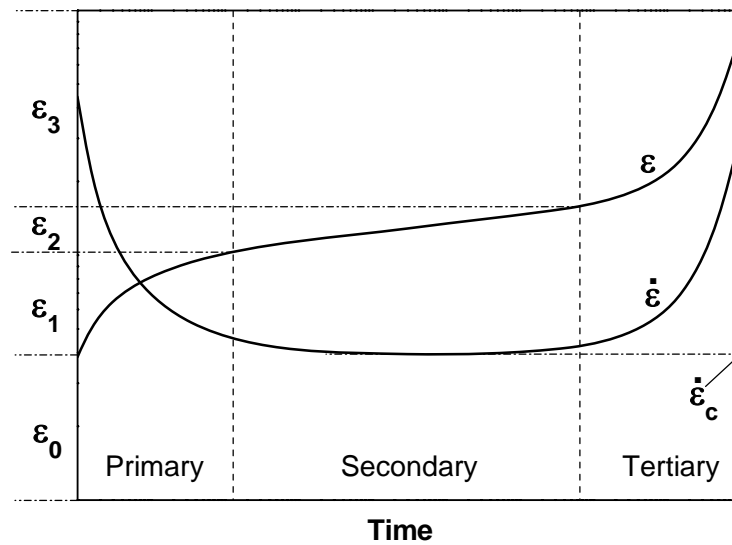
Figure 1.1: Representative creep strain and creep rate curves showing the complete stages.

tertiary creep stage (ε_3), where the creep rate and deformation increase rapidly and finally creep rupture or advanced necking occurs.

1.2 Polymer-based nanocomposites

In recent years, the limits of optimizing composite properties using traditional micron or macro-sized fillers have been reached due to compromised performance, e.g., strength is traded for ductility, or stiffness traded for toughness. In addition, macroscopic defects from regions of filler aggregates often lead to breakdown or failure. A promising opportunity has now arisen to overcome the limitations of traditional polymer composites by the use of nanofiller modified polymer composites, in which the filler is less than 100 nm in at least one dimension. Although some nanocomposites, e.g., carbon black filled silicone rubber [41], have been used for more than a century, research and development of polymer nanocomposites have increased remarkably in recent years for several reasons. First, a previously unimaginable improvement in property combinations has been obtained in some polymer nanocomposites [28, 31], e.g., yield stress, ultimate tensile strength (UTS), and Young's modulus were increased simultaneously in some semicrystalline thermoplastic composites filled with nanoparticles compared to pure polymers [42].
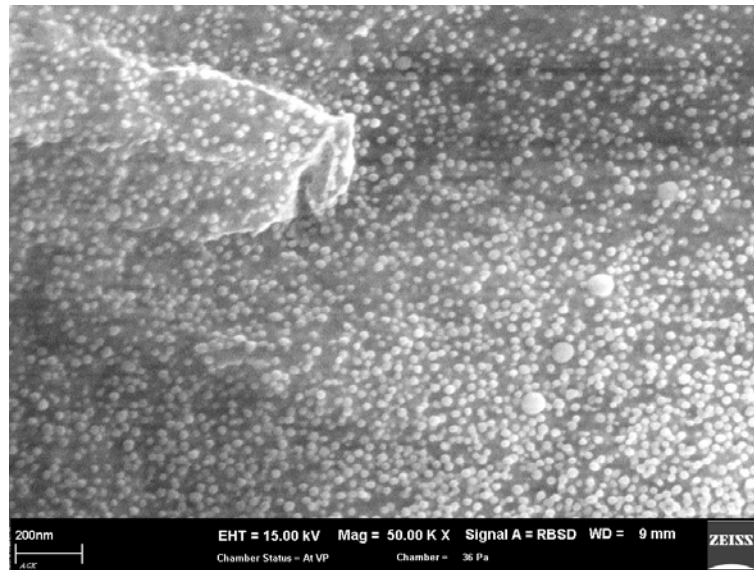
Figure 1.2: Almost ideal dispersion of 12 vol. % SiO$_2$ nanoparticles in epoxy using in situ processing technique. (Courtesy: H. Giertzsch, 2006)

The second reason is the discovery [43] and high yield synthesis [44-50] of carbon nanotubes with exceptional physical and mechanical properties, such as extremely high modulus and strength and even ductility [51-65]. As a novel kind of carbon material, carbon nanotubes are significantly different from carbon fibers and graphite, and play an important role in nanofillers to stimulate the development of nanocomposites. The third reason is that the dispersion technologies for nanofillers have been rapidly developed by means of chemical and in situ processing [28, 31, 66-79]. For example, as illustrated in Figure 1.2, a uniform dispersion of 12 vol. % SiO$_2$ nanoparticles in epoxy was achieved by using in situ polymerization. This development has also created excellent ability to control the interface between the matrix and the filler [67, 74, 80-82]. Thus, an exciting new era is at hand for research into nanocomposites, not only because the unique combinations of properties are achievable but because there is great potential for wide commercial application.

1.2.1 Nano-effects

Nanometric materials are normally defined as those with at least one dimension less than 100 nm. Nanofillers can be grouped into three classes according to their shape, as shown in Figure 1.3 with (a) 3-D nanoparticles, (b) 2-D platelets, and (c)1-D nanotubes. As novel materials, nanometric fillers have numerous advantages over
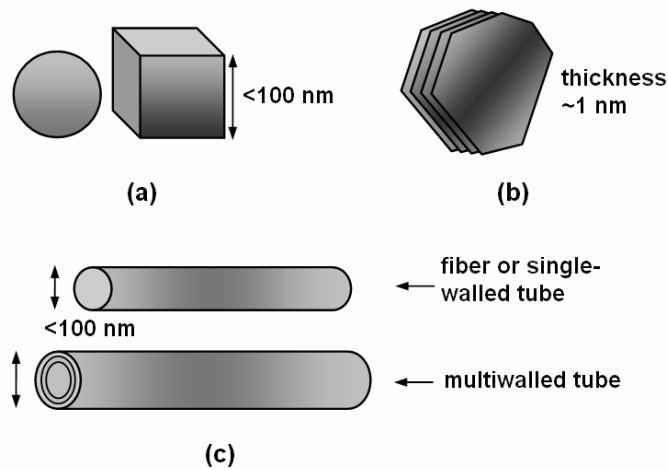
Figure 1.3: Schematic classification of nanofillers by their geometry. **(a)** 3-D nanofiller (particle and cube), **(b)** 2-D nanofiller (platelet), and **(c)** 3-D nanofiller (fiber and single- and multi-walled tube).

their micrometric counterparts due to their tiny body size. There are several general phenomena related to these "nano-effects" [31]. First, the size of nanofillers, e.g., nanoparticles with diameter less than 10 nm, is comparable to that of polymer chains. At this point, nanoparticles can be integrated perfectly into polymer matrix without defects. Thus high stress concentrations can be moderated and the ductility of polymers is not impaired [71]. In addition, interparticle distance can be very close on
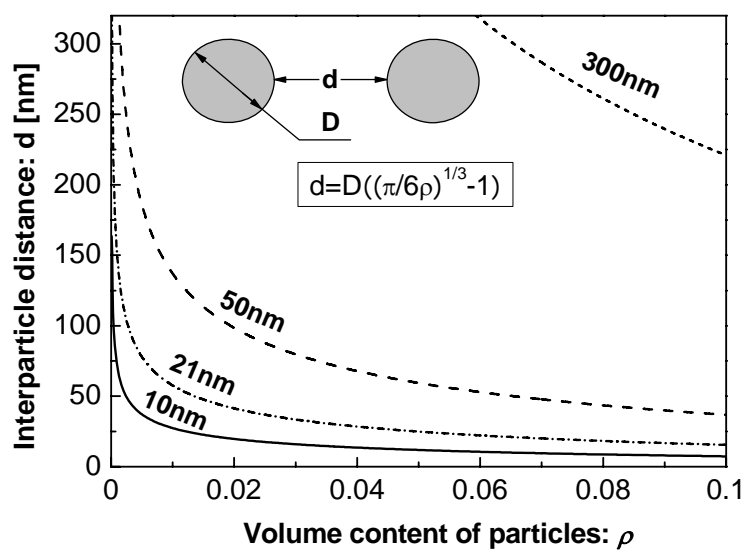
Figure 1.4: Interparticle distance as a function of volume content and particle diameter of fillers on the assumption of uniform dispersion.

nano-level, as shown in Figure 1.4 with various particle diameters and changing volume fraction. It can be seen that when particle diameter is less than 20 nm, an interparticle distance in nanometer scale is easy to achieve even with low volume content of the filler. For submicron particles, to obtain an interparticle distance in the nanometer range would result in high volume content. Thus large defects in regions of agglomeration would greatly compromise the reinforcing effectiveness. With nanoparticles a much denser and stiffer network can be formed, for example by small sized particles, and the mobility of polymer chains can be significantly restrained. Relevant properties such as toughness [83-85], gas permeability [86], and viscoelasticity and creep resistance [87, 88] can also be improved.

Second, the huge specific surface area of nanofillers results in an exceptionally large interfacial area between fillers and matrix. Specific surface area is defined here as the total surface area of nanoparticles at certain volume content in a unit volume composite. Figure 1.5 illustrates the specific interfacial area as a function of particlediameter and volume content. The specific interfacial area increases dramatically below 100 nm. The interfacial area is considered a most important characteristic in nanocomposites as well as in traditional composites [91] because
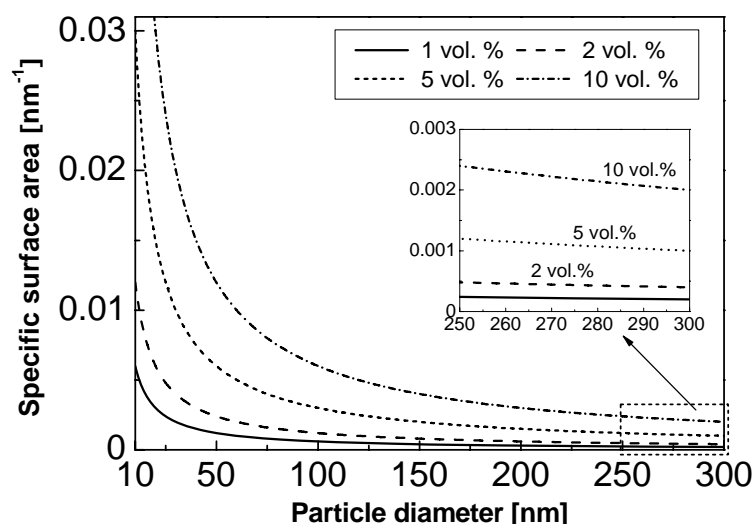
Figure 1.5: Specific surface area of particles as a function of particle diameter and volume content on the assumption of uniform dispersion. The insertion graph showing the value at the range of large particles.

the interface determines the degree of interaction between the filler and the matrix in terms of interfacial strength. A special region around the interface has been identified in a large range of 2 ~ 50 nm, where the physical and chemical properties of the matrix are changed, including crystallinity, cure degree, and mobility of polymer chains [31], and an alternative nomenclature, "interphase", has been given. From Figures 1.4 and 1.5 it can be concluded that the interphase region together with fillers can result in a huge network even with a low nanofillers loading. Consequently, increasing the interfacial area will bring about improvements in properties. There are two possible ways to accomplish this target, decreasing particle size and increasing filler concentration. However, there is a dilemma concerning dispersion, for example in the processing of melt compounding. It is easy to achieve a high fraction of fillers in agglomerates, which greatly compromises reinforcing effectiveness. Small particles cannot be applied at high content due to the very small interparticle distance. How to achieve a uniform dispersion at high filler concentration using the melt mixing technique is an ongoing topic of interest in polymer nanocomposites [67, 90, 91].

Another "nano-effect" arises from the exceptional properties of the fillers themselves. For example, single-walled nanotubes are considered perfect molecule material without any defects, having modulus and strength as high as 1 TPa and 500 GPa [31, 52, 53, 55, 92-94], respectively.

These "nano-effects" of nanofillers are significantly different from those of their micrometer counterparts. Numerous studies relating to the basic questions and engineering applications of nanofillers in polymer matrices have led to flourishing vision in composite fields.

1.2.2 Current studies of time-dependent behavior of nanocomposites

As mentioned in the introduction, design for material stability and reliability requires knowledge of time-dependent behavior such as viscoelasticity, creep, fatigue, etc. Creep and fatigue have been comprehensively observed in traditional polymer composite fields [1, 95]. The novel nanocomposites are promising materials to replace traditional counterparts in some applications. Consequently, study of these

properties has grown in recent years.

I. Nanoparticle composites

Lazzeri et al. [96] observed the viscosity of precipitated $CaCO_3$ particle filled high density polyethylene nanocomposites (PCC/HDPE) with and without surface treatment of the particles by stearic acid. They found that the addition of uncoated PCC resulted in a rise in viscosity. However, coated PCC caused a decrease in viscosity while preventing the particles from agglomerating to some extent, and reduced the size of the agglomerates. More recently, Kim at al. [97] studied the rheological properties of different loadings of ferrite nanoparticle (0.1 – 20 wt. %) filled Nylon-66 composites. The relaxation time was increased with increasing ferrite content above 1 wt. %. The nanocomposites with more than 5 wt. % ferrite particles displayed significant shear thickening behavior at the low frequency. At the higher frequency, shear thinning occurred and the degree of thinning increased with increasing filler loading. It was concluded that nanoparticles began to restrict polymer chain mobility with a fraction above 1 wt. %, and changed the molecular structure of Nylon with a concentration above 5 wt. % and then accelerated the orientation of polymer chains under high shear. Sarvestani and Picu [98] proposed a network model to simulate the viscoelastic behavior of nanoparticle/polymer melts. The rheological property and the shear viscosity of nanocomposites were simulated by taking into account the important roles of the lifetime of polymer-filler junctions and the network of bridging segments. The greatest reinforcement was observed at low strain rates and low frequency oscillations. A solid-like behavior was predicted for systems in which the polymer molecules interacted strongly with the nanoparticles.

The experimental and modeling studies of time-dependent behaviors of nanoparticle /polymer composites indicate that the mobility of polymer chains was restrained by particles. And the immobilization of polymer chains was associated with the degree of filler dispersion, polymer-filler interaction, interparticle distance, etc.

II. Layered nanoclay composites

Lee et al. [25] observed the viscoelastic properties of epoxy nanocomposites using the small-strain stress relaxation method. They found that the characteristic relaxation time was increased in the composites due to the addition of nano-reinforcement. Lele et al. [99] studied the creep behavior of molten PP nanocomposites filled by clay with and without compatibilizer during melt intercalation in an extruder. They found that creep resistance was greatly increased in compatibilized hybrids compared to uncompatibilized composites. Creep results and X-ray diffraction (XRD) analysis indicated that some of the silicate layers from the edges of the crystallites possibly exfoliated into the matrix during annealing of the hybrid. The exfoliated layers bridged different silicate crystallites to form a percolating network that strongly restrained creep deformation. Pegoretti et al. [100] observed the creep performance of recycled polyethylene terephthalate (PET) filled with layered silicate. They obtained a slightly decreased creep compliance and non-rising creep rate in composites compared to neat matrix. More recently, D'Souza et al. [101] studied polyethylene/montmorillonite layered silicate (PE/MLS) films and found that the presence of rigid MLS contributed to improved creep resistance of the composites. Picken et al. [102] also studied the effects of physical aging time and moisture on the creep properties of polyamide 6 (PA6) filled by layered silicate. They demonstrated that the creep compliance of composites could be greatly reduced compared to that of neat PA6. Blackwell and Mauritz [103] reported the shear creep behavior of a sulfonated poly(styrene-b-ethylene/butylene-b-styrene) (sSEBS) /silicate nanocomposite, the experimental data of which could be satisfactorily simulated by using a modified Burgers creep model.

The time-dependent performance of polymer composites reinforced by layered fillers has been widely studied [28]. It is believed that fully exfoliated layers bridge different silicate crystallites to form a percolating network that can strongly restrict deformation of polymer chains. Thus the degree of exfoliation during melt mixing plays an important role in determining the final properties.

III. Nanotube composites

Current studies directly or indirectly related to creep on nanotube/polymer composites entail viscoelasticity measurements, which are performed under dynamic load [104-107], indicating an interaction between nanotubes and matrix, and deformation observation, which has been focused on load transfer effect due to the large aspect ratio and good interfacial strength [108-115].

Liu et al. [104] observed the glass transition temperature of an epoxy composite filled by 1 wt. % carbon nanotubes in a surfactant-assisted processing, recording an obvious increase of T_g in the composite from 63 °C to 88 °C. Castano et al. [116] studied the thermal and mechanical properties of functionalized carbon nanotube reinforced poly(methyl methacrylate) (PMMA) and found that the storage modulus and T_g of the composite were significantly increased 12-folds and by 40 °C, respectively, compared to those of matrix. Other reports [82, 105, 117-123] of the increase in glass transition temperature of CNT/polymer composites indicated that there exists a mechanical or even chemical bond between nanotubes and polymer chains, which strongly restricts the mobility of molecules.

Fisher et al. [106] studied the viscoelasticity of multiwalled carbon nanotube reinforced polycarbonate (MWNT/PC). They found that macroscale experimental results indicated that the effective relaxation spectra of the composites were consistent with non-bulk polymer regions of restricted molecular mobility, which was due to localized nanoscale interactions between the nanotubes and individual polymer chains. Recently, Koratkar et al. [107] observed the viscoelasticity of MWNT/epoxy composite film with filler content as high as about 50 vol. %. They reported strong viscoelastic behavior with up to 1,400 % increase in loss factor (damping ratio) of the baseline epoxy. It was considered that the increased damping was related to frictional energy dissipation during interfacial stick-slip sliding at the large and spatially distributed nanotube-nanotube interfaces. More recently, Koratkar et al. [124, 125] studied the effects of temperature and mechanical pre-strain on damping of SWNT/PC composites. They found that interfacial nanotube-matrix friction slip could be activated either at elevated temperature with low strain levels or at a static pre-strain with low dynamic strain amplitudes. The effectiveness of

nanotube-matrix sliding energy dissipation was significantly improved and resulted in damping enhancement in composite structures.

Thermal and dynamic mechanical research on CNT composites has illustrated good bonding existing between nanotube-polymer interfaces. Deformation behaviors of nanotube/polymer composites presents another way to understand the importance of interfacial bonding and aspect ratio. Ajayan et al. [110] measured the load transfer in MWNT epoxy composites by means of tension and compression tests. They found that the compressed modulus was higher than the tensile modulus and proposed that only the outer layers were stressed in tension whereas all the layers responded in compression. Lourie and Wagner [126] found evidence of stress transfer and formation of fracture clusters in MWNT/epoxy composites. The damage clusters were comparable to those arising in fiber-reinforced composites as a result of the redistribution of stress from a failed fiber to its non-failing adjacent neighbors. Dickey et al. [111] analyzed load transfer and deformation mechanisms in MWNT/polystyrene (PS) composites and found that the elastic modulus and break stress were obviously increased. The Halpin-Tsai model was used to present an appropriate evaluation between the experimental and calculated values. The interfacial strength and aspect ratio of tubes have also been analyzed. Qian and Dickey [127] observed the deformation of MWNT/PS composites by using the in situ TEM method. They found that load transfer across the nanotube-PS interface was operative well into the plastic deformation regime of the composite film. Although most of the MWNTs eventually debonded at the interface and subsequently pulled out from the matrix, some direct evidence of failure mechanisms of MWNTs, such as sword-in-sheath and transverse shear fracture, was observed.

These studies showed that the load transfer effect played an important role in reinforcing the properties of nanotube-polymer composite. Other studies [81, 82, 108, 115, 128-132] have shown that the aspect ratio of nanotubes and interfacial strength between nanotube and matrix were key factor determining the effectiveness of load transfer.

1.3 Deformation mechanisms

1.3.1 Experimental observations in nanocomposites

From the numerous studies on the enhanced thermal and mechanical properties of polymer nanocomposites (PNC), it can be concluded that this improvement is attributed to the immobility of polymer chains due to the addition of nanofillers. The creep deformation of composites is reasonably associated with this immobility. The degree of immobility is affected by interfacial strength (surfactant processing or not), filler geometry (particle, platelet, and tube) and dispersion status (degree of aggregation), filler content, etc. In nanoparticle/polymer composites, a 3-D network formed by particles acts as an obstacle for the motion of polymer chains. Parameters such as interparticle distance (filler content) and interfacial region (particle size) play important role at this point. Figure 1.6 shows a schematic representation of the molecule structure of particle/polymer composite [98]. However, an improved structure is developed and presented in the following chapter.
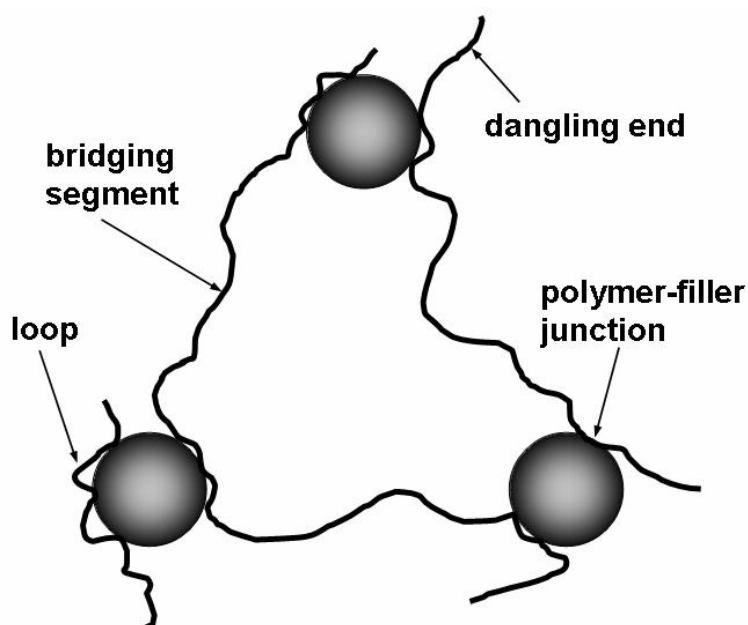
Figure 1.6: Schematic representation of the molecule scale structure of nanoparticle /polymer composites. (Revised from [98]. Based on the assumption that particles with a diameter of 20 nm are uniformly dispersed and the diameter of the molecules is 1 nm.)
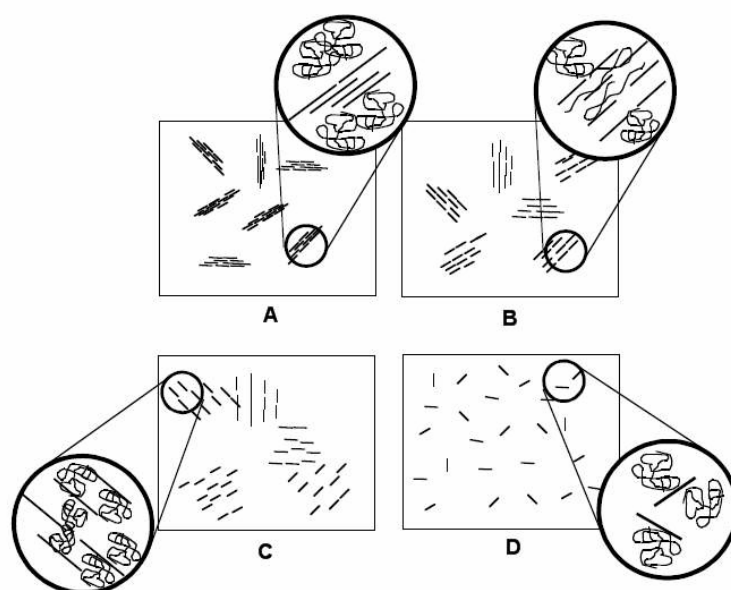
Figure 1.7: Schematic diagrams of the microstructures of clay-filled polymer composites: **(a)** a traditional composite with tactoids, **(b)** an intercalated nanocomposite, **(c)** an ordered exfoliated nanocomposite, and **(d)** a disordered exfoliated nanocomposite [31].

In layered filler/polymer composites, the scene is different from that of particles due to their 2-D structure with high aspect ratio. A schematic diagram of the microstructures of clay-filled polymer composites is given in Figure 1.7. In melt processing, intercalated and partially ordered exfoliated nanocomposites are normally obtained. However, it is very difficult to achieve full exfoliation of layered fillers [133]. The strength between intercalated and partially exfoliated layers plays a significant role in deformation because shear stress can result in interlayer slip, compromising the improvement. In CNT composites, external load can transferred to nanotubes through good interfacial regions. In this way the load bearing ability that is related to creep deformation of composites is significantly enhanced. Although most nanotubes do not break due to their high strength, the failure types of nanotubes like sword-in-sheath [134] (Figure 1.8) and transverse shear fracture [127] provide some clues to understanding the possible damage evolution in creep deformation. It is noteworthy to point out that intertube sliding contributes to improvement of damping [107] but may be a negative factor to enhancing creep resistance.

Figure 1.8: Evidence of nanotube broken by the sword-in-sheath fracture mechanism in MWNT/PS composite film [127].

1.3.2 Creep modeling analyses

Besides experimental observation, highly developed creep modeling analyses in traditional composites can be also applied in nanocomposites to develop comprehensive understanding of creep deformation. In the past half century, numerous creep models [1, 2, 135] have been proposed and applied to describe the creep behaviors of viscoelastic polymers and composites. Simplified elastic spring and viscous dashpot units are considered connected in series or parallel, as shown in Figure 1.9. Amongst the viscoelastic models, Burgers or the four-element model is one of the most widely used [136-138] and is introduced in Chapter 4. Recently, Blackwell and Mauritz [103] applied a modified Burgers creep model to satisfactorily simulate the creep data of nanocomposite.

Besides constitutive models, empirical or mathematical descriptions have also been widely studied [1], due to their simple expression and satisfactory simulation or prediction capacity. Among these, the Findley power law is one of the most acceptable models [1, 139-142]. It is capable not only of simulating the experimental data but also of predicting future behavior very well. A detailed introduction is provided in Chapter 4.

Since creep experiment is very time-consuming, many superposition methods, including time-temperature [2, 135, 143-148], time-stress [149-151], time-strain [146, 152, 153], and time-moisture [154, 155], have been developed on the basis of the
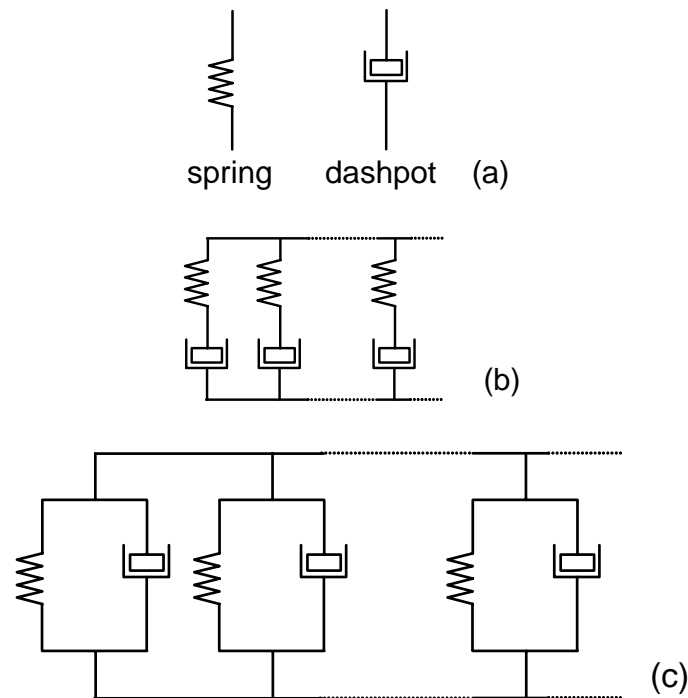
Figure 1.9: Creep models. **(a)** creep units, **(b)** and **(c)** generalized models in different connections.

different natures of materials. The long-term behavior of materials can be obtained by shifting short-term experimental data on the reference state to form a master curve with a large time scale. These methods are applicable and much amount of experimental work can be saved. A description of the time-temperature-stress superposition principle is presented in Chapter 4.

1.4 Summary

Over the past decades, studies on the time-dependent behaviors of traditional polymers and composites have been widely carried out by many means for the purpose of materials design. Recently the limits of optimizing composite properties using traditional micron/macro-sized fillers have been reached, due to compromised resulting performances. Fortunately in recent years rapid development has occurred in nanometric materials, e.g. nanoparticles, nanoclay platelets and nanotubes, with novel physical and mechanical properties. Correspondingly, studies on nanocomposites have been increasingly focused as a promising field in materials science. General mechanical properties have been extensively explored. However,

systematic and comprehensive observation of time-dependent behaviors is an urgent requirement for designers and computing engineers dealing with long-term applications of polymer nanocomposites as structural materials.

It is thus interesting and valuable to apply and develop traditional polymer composite analysis methods, such as creep models and prediction principles, to nanocomposites. Such work will not only expand our knowledge of nanocomposites but also present a detailed and direct reference for materials of this type in practical applications. That is the ultimate aim of the current work.

2 Objectives of the Study

Over the past few decades, interest has grown rapidly in polymers and their composites as structural and functional materials in engineering applications, where dimensional stability and reliability are among the main considerations. As reviewed in Chapter 1, traditional fillers, including fibers and particulates, have been successfully applied in polymers for the purpose of improving the above-mentioned characteristics. In recent years, nanocomposites have been increasingly focused as a novel field in materials science. However, there are still many scientific and technical questions concerning such materials and their optimal property combinations. With this background, the main task of the current work is to study the reinforcing effects and mechanisms of different nanofillers on modifying the creep behavior of polymer. The study is carried out on three material systems by means of experimental observation and modeling and prediction analysis. The scope and aim of each material system and theoretical analysis are elaborated as follows, as also depicted in Figure 2.1 with a flowchart structure.

Nanoparticle/PA system

Nanoparticles are widely used as additives in polymer composites. In this study, PA66 composites filled with different kinds of nanofiller, i.e. 300 nm and 21 nm TiO_2 particles and nanoclay platelets (single platelet 100~500 nm x 1 nm), were prepared for creep tests. Additionally, surface modified 21 nm TiO_2 particles were investigated to understand the effect of surface modification on creep performance. The volume content of all nanofillers was constant at 1 %. The creep experiments were performed at different stress levels (20, 30, 40, 60 MPa) at room and elevated temperatures (23, 50, 80 °C). The target was to characterize the creep behavior of the materials and understand the effect of different nanoparticles on enhancing creep resistance by considering the isochronous stress-strain curves, creep rate, and creep compliance with temperature and stress effects. Static tensile tests were also performed at corresponding temperatures. In addition, changes in crystalline morphology of matrix and composites were analyzed. Orientational hardening and thermally and stress activated Eyring rate process are briefly introduced to

understand in depth the mechanisms of viscoelasticity of these nanocomposites. The creep resistant nanoparticle/PA system can provide a systematic overview and be an important reference for this type of material for the purpose of engineering applications.

Nanoparticle/PP system

To understand how the behavior of nanoparticles engenders a general improvement in the creep resistance of polymers, another kind of thermoplastic with low glass transition temperature was considered. PP was selected for this purpose. Fillers of 300 nm and 21 nm TiO_2 were set as 1 vol. %. Another aim was to obtain more

```
                    ┌─────────────────────────────────┐
                    │      Creep resistant             │
                    │      nanocomposites              │
                    │                                  │
                    │ Creep characterization and       │
                    │ mechanisms of nanocomposites,    │
                    │ modeling analysis and            │
                    │ prediction of long-term creep    │
                    │ behaviors                        │
                    └─────────────────────────────────┘
```

Creep resistant nanocomposites

Creep characterization and mechanisms of nanocomposites, modeling analysis and prediction of long-term creep behaviors

Nanoparticle/PA system

Creep characterization and structure-to-property relationship of PA66 nanocomposites

Nanoparticle/PP system

Reinforcing effects of particle size and structure-to-property relationship of PP nanocomposites

MWNT/PP system

Creep characterization and load transfer mechanism of CNT nanocomposites

Creep modeling analysis

Simulation of the experimental data and modeling parameter analysis via Burgers model and Findley power law; comprehensive understanding of creep resistant nanocomposites

Prediction of long-term behaviors

Determining long-term creep behaviors based on short-term experiments by means of creep models and TTSSP method

Figure 2.1: The aims of the creep experiments and the modeling and prediction analysis of the three material systems observed in this study with a flowchart.

information about the effect of particle size on the creep behavior of matrix. As expected, nanoparticles improved the creep resistance of the matrix without sacrificing tensile properties. Additionally, the creep lifetime of the nanocomposites was extended under high stress levels compared to that of neat polymer. The concept of a 3-D network formed by nanoparticles was developed to explain this improvement in creep resistance. Further experimental results, including changes in spherulite morphology in the composites and changes in crystallinity before and after creep tests, were provided to support the explanation.

MWNT/PP system

Due to their excellent physical and mechanical properties of carbon nanotubes, their application as reinforcers in the composites field has been of great interest in recent years. Here PP compounded with 1 vol. % short and large aspect ratio multiwalled carbon nanotubes was studied. The aim was to explore the creep behavior of this novel kind of composite. It was anticipated that the nanotubes would markedly improve the creep resistance of the matrix with significantly reduced creep deformation and creep rate. Additionally, the creep lifetime of the composites was significantly extended compared to that of neat matrix. The improvement in creep resistance contributed to efficient load transfer between the carbon nanotubes and surrounding polymer chains. The results should lead to improved grades of creep resistant polymer nanocomposites for engineering applications.

Modeling analysis and prediction of long-term behavior

Finally, creep modeling analysis based on the experimental data was executed to comprehensively understand the creep behaviors of the nanocomposites and to attempt to find some structure-to-property relationship via physical modeling parameters. In practical applications, creep normally occurs under small stress levels and is a very time-consuming task in laboratory observation. It was necessary if possible to determine long-term behaviors based on short-term experiments. This purpose could be accomplished through prediction methods. Creep models were compared in their capacity to achieve this purpose, and the model with good

prediction ability was applied. In addition to model prediction, time-temperature and time-stress superposition principles were applied in PA and PP systems, respectively. The prediction methods make it possible to save a large amount of experimental work by using less data to forecast the behavior of materials.

3 Experimental Procedures

3.1 Selection of materials

3.1.1 Polymer matrices

In the current study, two commercial thermoplastics were selected as matrices. One was polyamide 66 (PA66), which displays good mechanical properties and toughness, and is widely applied in the automotive and chemical industries and in commodity consumption. The other was polypropylene (PP), which has the lowest density (~0.90g/cm^3) of all plastics and is widely used as fibers and films with reinforcements for improved properties. Table 3.1 shows the details of matrix designation, manufacturer, and also the as-received physical and chemical parameters.

3.1.2 Nanofillers

In order to investigate the effects of nanofillers on creep performance, three different kinds of filler were selected: 3-D particles, 2-D clay layers and 1-D tubes. The volume content of all fillers was constant in the range of 1 %. TiO_2 particles with diameter of 21 nm and 300 nm were chosen to identify the size effect. Surface modified 21 nm TiO_2 particles were also used to obtain a better dispersion.

The as-received clay particles with a diameter of 35 μm contained 100~500 nm platelets with 1 nm thickness and could be exfoliated during melt extrusion. Considering their exceptionally good mechanical and physical properties, large and small aspect ratios of multiwalled carbon nanotubes (5~15 μm and 1~2 μm long) with an outer diameter of 10~30 nm were applied as reinforcers. Detailed information about the selected fillers is provided in Table 3.2.

Table 3.1: Designation and product details of the selected matrices.

Designation	Brand Name	Tensile Strength (MPa)	Density (g/cm^3)	T_g/T_m (°C)	Manufacturer
PA66	Zytel 101L	77	1.14	52/262	duPont
PP	Moplen HP501H	33	0.90	12/168	Basell Co.

Table 3.2: Designation and product details of the selected nanofillers.

Designation	Brand Name	Diameter (nm)	Length (μm)	Density (g/cm^3)	Specific Surface Area (m^2/g)	Modified Surface	Provider
300-TiO$_2$	Kronos 2310	300	-	4.0	-	No	Kronos Inc.
21-TiO$_2$	Aeroxide P25	21	-	4.0	50	No	Degussa
21-SM-TiO$_2$	Aeroxide T805	21	-	4.0	45	Yes	Degussa
Nanoclay	Nanofil 919	100~500	0.001	1.8	-	No	Süd Chemie
S-MWNT	S-MWCNT1030	10~30	1~2	1.75	-	No	Shenzhen Nanotech Port Co. Ltd.
L-MWNT	L-MWCNT1030	10~30	5~15	1.75	-	No	

3.2 Specimen preparation

3.2.1 Extrusion

I. PA series

PA series nanocomposites were compounded using a corotating twin-screw-extruder (Berstoff ZE 25A×44D-UTS). The barrel temperatures were set at 55/260/270 /280/285/285/285/285/285 °C. A screw speed of 150 rpm was used, and a final extrusion rate of 9 kg/h was applied. The matrix was dried in a vacuum oven at 70 °C for a minimum of 24 hours before extrusion. During melt extrusion, ventilation was kept on to remove trapped air in blends. Other processing parameters were also optimized in order to achieve a fine nanoparticle distribution. To precisely control the content of the nanoparticles, a commercial twin screw loss-in-weight feeder (K-Tron Soder K-CL-24-KT20) was used. After cooling by water bath, the extruder blanks were cut as granules with length in the range of 3~5 mm for further injection molding.

II. PP series

To obtain good dispersion of fillers, a two-step extrusion procedure was adopted for PP series nanocomposites. In the first step, pre-extruding compounds with a high concentration of fillers were obtained. In the second extrusion the pre-extruding compounds were put into the feeder as fillers and the final composite granules were produced. The filler content was calculated in each step. The barrel temperatures were set at 50/185/190/195/200/200/200/200/200/200°C, and all other processing parameters were the same as those in the PA series.

3.2.2   Injection molding

Before injection molding the granules were dried to evaporate moisture. The composites were then manufactured using an injection molding machine (Alburg Allrounder 320S) as dog-bone tensile specimens ($160\times10\times4$ mm^3, according to the German standard of DIN-ISO-527) for tensile and creep tests. The injection parameters were kept constant for each series of matrix systems. The barrel temperature of the injection molding machine was set at 295 °C and 220 °C for the PA and PP series, respectively. The injection pressure was kept constant at 500 bars, the mold temperature was fixed at 70 °C and 40 °C for the PA and PP series, respectively, and a constant injection speed of 80 ccm/s was applied for all specimens.

3.2.3   Specimens for tensile and creep experiments

In this study PA66 and PP composites reinforced with 1 vol. % different nanofillers were investigated. The size and form were according to Type 1A in DIN ISO 527-2 [156]. Concerning the different structures of the nanofillers, three material systems were classified for the following discussion: Nanoparticle/PA, Nanoparticle/PP, and MWNT/PP. A complete list of prepared specimens is shown in Table 3.3.

3.3   Mechanical experiments

3.3.1   Quasi-static tensile test

A Zwick universal testing machine (Zwick 1485) was used for uniaxial tensile testing. Both an extensometer and a 10 kN load cell were equipped for measuring tensile modulus and strength. Dog-bone tensile specimens were used with dimensions of $160\times10\times4$ mm^3. A gauge length of 50 mm was considered. The crosshead speed was kept constant at 2 mm/min for room temperature and 5 mm/min for elevated temperature measurements. An environmental chamber was used for elevated temperature testing. At least four specimens of each material were tested, and the average values with standard deviation were reported.

Table 3.3: Material systems applied in this study.

Material System	Designation	Filler Designation	Amount of filler/mm^3
Nanoparticle/PA	PA66	-	-
	300/PA	300-TiO$_2$	7.1×10^8
	21/PA	21-TiO$_2$	2.1×10^{12}
	21-SM/PA	21-SM-TiO$_2$	2.1×10^{12}
	Clay/PA	Nanoclay	1.1×10^{11}
Nanoparticle/PP	PP	-	-
	300/PP	300-TiO$_2$	7.1×10^8
	21/PP	21-TiO$_2$	2.1×10^{12}
MWNT/PP	PP	-	-
	S-MWNT/PP	S-MWNT	2.1×10^{10}
	L-MWNT/PP	L-MWNT	3.2×10^9

3.3.2 Uniaxial tensile creep

Uniaxial tensile creep tests were preformed by a Creep Rupture Test Machine with double lever system (Coesfeld GmbH, Model 2002), as schematically shown in Figure 3.1. Ten specimens can be measured at one time in an environmental chamber. Before testing, the desired constant load for each measurement unit was calibrated using a force transducer. Then the samples were fixed into the clamps without loading and the original gauge length was recorded. For the elevated
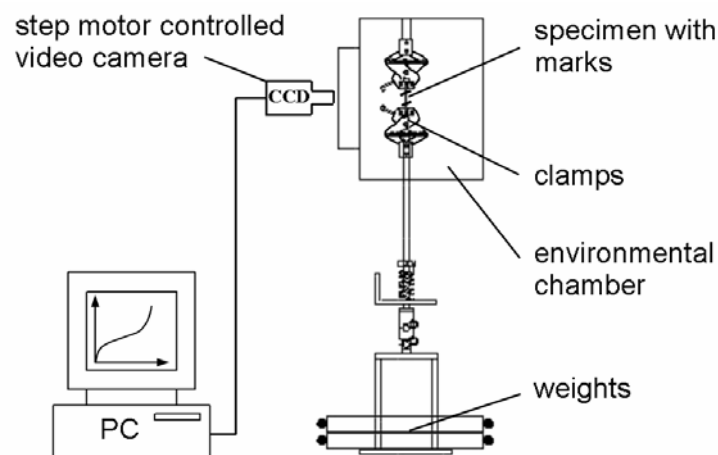
Figure 3.1: Schematic diagram of the tensile creep testing machine according to the Creep Rupture Test Machine Model 2002.

temperature measurement, the chamber was preheated to the desired level for at least 24 hours before loads were applied to the specimens, in order to reach a uniform and steady thermal distribution. The relative humidity was kept below 50%. A gauge length of 30 mm was marked on each specimen, and the elongation was monitored by a video camera, which was equipped with a program-controlled step motor and connected to a computer imaging analysis system during the whole period of creep testing. Creep compliance was calculated by the ratio of the measured creep strain to the initial stress. The measurement procedure was performed based on ASTM 2990-01 [157].

3.4 Microscopic characterization

3.4.1 Scanning electron microscopy

A scanning electron microscope (SEM, Jeol 5400) was applied to simply characterize the dispersion of nanofillers in PA66 matrix. The specimens were submerged in liquid nitrogen for 2 hours, after which they were taken out and broken using pincers. To obtain stable images, the fracture surfaces were firstly sputter coated by a sputtering device (SCD-050) with a Pt/Pd alloy for at least 140 seconds. The resulting images taken from the fracture surfaces represented dispersion of fillers.

3.4.2 Transmission electron microscopy

Ultrathin sections (approximately 50~100 nm) of 21/PP and S-MWNT/PP specimens were microtomed at room temperature. The dispersion characterization of nanoparticles and CNTs in the PP matrix was observed using a transmission electron microscope (TEM, FEI Tecnai G 20) as well.

3.4.3 Polarization microscopy

Films were cut using a Leitz 1400 microtome. To obtain a clear morphology of spherulite, films as thin as possible were carefully prepared. The spherulites of neat matrices and nanocomposites were then observed using a Leitz Diaplan polarization microscope, equipped with a video camera connected to a personal computer.

3.5   Dynamic mechanical thermal analysis

Dynamic mechanical thermal analysis (DMTA) was carried out to determine the effects of nanofillers on the glass transition temperature (T_g). DMTA experiments were performed with rectangular specimens ($50 \times 10 \times 4$ mm^3) under tension loading at 10 Hz using an Eplexor 25 N device of Gabo Qualimeter. The static and cyclic (sinusoidal) loads were set as 20 N and ±10 N, respectively. Temperature ranges of -100~+200 °C and -50~+100 °C were used for the PA66 and PP material systems, respectively. The mechanical loss factor (tan δ) was measured to determine T_g at a heating range of 2 °C/min. At least two specimens were repeated and the average values were presented.

3.6   Differential scanning calorimetry

A differential scanning calorimeter (Mettler Toledo, DSC 821) was used to measure the crystallinity of specimens before and after creep experiments. The temperature ranges of 0~300 °C and -20~220 °C were considered for the PA66 and PP material systems, respectively. The mass of samples was cut from bulk specimens in the range of 10~20 mg. The heating rate was set as 10 °C/min and at least three samples were measured. Crystallinity was then calculated by the ratio of the specific melting heat of the specimens to that of the fully crystallized matrix, as given in the literature. Additionally, the glass transition temperature of the PA66 system was obtained using this method.

4   Theoretical Methods for Analyzing Creep Characteristics

4.1   Creep compliance

In addition to the general description of creep in terms of creep deformation and creep rate in Chapter 1, creep compliance, $J(t,\sigma(t),T)$, is also frequently used to describe creep behavior. It can be obtained via the following relation

$$J(t,\sigma(t),T) = \frac{\varepsilon(t,\sigma(t),T)}{\sigma_0} \qquad (4.1)$$

where t is creep time, $\sigma(t)$ real stress, σ_0 initial applied stress, T temperature, and $\varepsilon(t,\sigma(t),T)$ creep strain dependent on creep time, real stress and temperature. For cases of small deformation, the real stress is normally considered to be the same as the initial stress and thus the strain is proportional to the initial stress, so we have

$$\varepsilon(t,\sigma(t),T) = \varepsilon(t,\sigma_0,T) = \varepsilon(t,T) \cdot c\,\sigma_0 \qquad (4.2)$$

Therefore, Equation (4.1) can be simplified as

$$J(t,\sigma(t),T) = J(t,T) = c\,\varepsilon(t,T) \qquad (4.3)$$

where c is constant. In Equation (4.3), creep compliance is the only function of creep time and temperature applied and therefore is considered a material constant for
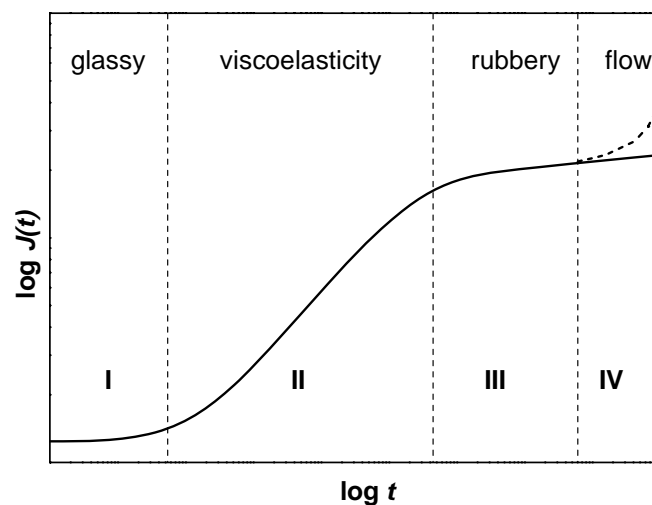

Figure 4.1: Schematic diagram of creep compliance versus time of polymers.

linear solids at constant temperature. An idealized amorphous polymer will behave as a glassy solid, viscoelastic solid, rubber or viscous liquid depending on the time scale or on the temperature of the experiment [2]. A schematic curve of creep compliance vs. time at constant temperature over a very wide time scale is shown in Figure 4.1. The diagram shows that for experiments of very short duration the obtained compliance lies at a low value in glassy status and is time independent. With a sufficiently long time scale the polymers become rubbery and present a plateau compliance that is time independent. For intermediate times, the compliance lies between these statuses and is time dependent, which is the general situation of viscoelastic behavior. Additionally, under high stress levels or at elevated temperatures, e.g. higher than T_g, polymers will act as viscous flow even for an experiment of short duration, which is the basis of the time-temperature-stress superposition principle as discussed in another subsection.

4.2 Creep models

Numerous models have been developed to describe creep behavior of polymers [1, 2, 10]. Two main classes can be defined. One is based on a physical assumption of viscoelastic material with elementary spring and dashpot units. This kind of representation can yield a basic understanding of material structure-property relationships through model parameters. The most widely used configuration is the so-called four-element or Burgers model. Additionally, the Eyring rate process model with a special dashpot [2] is also often used to obtain representatives of activation volume and energy. The second class has an empirical framework built on different kinds of mathematical expressions. Empirical models can provide very good agreement with experimental data and have a good capability to predict creep behavior based on known data. The most widely adopted formulation is the Findley power law, which is accepted by ASTM as a standard method to predict creep behavior of materials [1]. In this study the Burgers model, Eyring rate process model, and Findley power law are applied and compared. A detailed introduction to these models is given below.

4.2.1 Burgers model

Among the numerous viscoelastic creep models, the Burgers or four-element model [2] is most widely used to analyze the viscoelasticity of materials, as illustrated in Figure 4.2 with a Maxwell and Kelvin model connected in series. The constitutive equation for a Burgers model can be derived by considering the strain response under constant stress of each of the elements coupled in series, as shown in Figure 4.2. The total strain ε_B at time t will be the sum of the strain in the three elements, where the spring and dashpot in the Maxwell model are considered as two elements, thus:

$$\varepsilon_B = \varepsilon_{M1} + \varepsilon_{M2} + \varepsilon_K \tag{4.4}$$

where ε_{M1} is the strain of the Maxwell spring

$$\varepsilon_{M1} = \frac{\sigma}{E_M} \tag{4.5}$$

ε_{M2} is the strain of the Maxwell dashpot

$$\dot{\varepsilon}_{M2} = \frac{\sigma}{\eta_M} \tag{4.6}$$
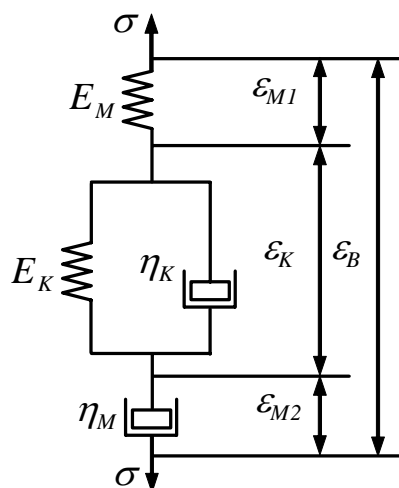
Figure 4.2: Schematic diagram of Burgers model consisting of Maxwell and Kelvin elements.

and ε_K is the strain of the Kelvin unit which can be described as

$$\dot{\varepsilon}_K + \frac{E_K}{\eta_K}\varepsilon_K = \frac{\sigma}{\eta_K} \tag{4.7}$$

where the subscripts B, M, and K indicate Burgers model, Maxwell and Kelvin elements, respectively. E and η are the modulus and coefficient of viscosity of the spring and dashpot, respectively. σ is applied stress.

Combining Equations (4.4)-(4.7) and eliminating ε_{M1}, ε_{M2}, and ε_{K3}, a second order differential equation can be obtained

$$\dot{\varepsilon}_B + \frac{\eta_K}{E_K}\ddot{\varepsilon}_B = \frac{\sigma}{\eta_M} + (\frac{1}{E_M} + \frac{1}{E_K} + \frac{\eta_K}{E_K\eta_M})\dot{\sigma} + \frac{\eta_K}{E_M E_K}\ddot{\sigma} \tag{4.8}$$

The constitutive creep relationship of the Burgers model under constant stress σ_0 can be obtained by solving Equation (4.8) with the initial conditions at $t =0$

$$\left.\begin{array}{l} \varepsilon_B = \varepsilon_{M1} = \dfrac{\sigma_0}{E_M} \\[2mm] \varepsilon_{M2} = \varepsilon_K = 0 \\[2mm] \dot{\varepsilon}_B = \dfrac{\sigma_0}{\eta_M} + \dfrac{\sigma_0}{\eta_K} \end{array}\right\} \tag{4.9}$$

Finally, the creep behavior of Burgers model can be obtained as follows

$$\varepsilon_B = \frac{\sigma_0}{E_M} + \frac{\sigma_0}{E_K}(1 - e^{-\frac{t}{\tau}}) + \frac{\sigma_0}{\eta_M}t \tag{4.10}$$

where $\tau = \eta_K/E_K$ is the retardation time taken to produce 63.2 % or $(1-e^{-1})$ of the total deformation in the Kelvin unit.

The creep characteristics of Burgers model shown in Equation (4.10) can be explained as follows. The first term is constant and determines the instantaneous elastic deformation; the second is delayed elasticity of the Kelvin unit and is dominant in the earliest stage of creep but soon reaches a saturation value close to

σ_0/E_K; the viscous flow then increases almost linearly in the third term after a sufficient duration of loading.

Differentiating Equation (4.10) yields the creep rate of Burgers model as follows

$$\dot{\varepsilon}_B = \frac{\sigma_0}{\eta_M} + \frac{\sigma_0}{\eta_K} e^{-\frac{t}{\tau}} \tag{4.11}$$

Over a sufficiently long time scale, the creep rate asymptotically reaches a constant value

$$\dot{\varepsilon}_B(\infty) = \frac{\sigma_0}{\eta_M} \tag{4.12}$$

The Burgers model, which includes the essential elements, can be applied satisfactorily to model the practical behavior of viscoelastic materials. The material parameters E_M, η_M, E_K, and η_K can be simulated from experimental data. Variation of the simulated parameters will constitutively show the effect of nanofillers.

4.2.2 Eyring model

The deformation of a polymer is considered in some cases as thermally activated rate processes involving the motion of chain molecules or parts of a chain molecule over potential barriers, as shown in Figure 4.3. Correspondingly, the dashpot in the standard linear solid can be replaced by an Eyring dashpot that is governed by the activated process, as illustrated in Figure 4.4. The Eyring model is introduced here due to its useful parameter of activation volume that may provide an indication of the underlying molecular mechanisms. The activated rate process may provide a common basis for the discussion of creep behavior as well.

The creep rate of a stress activated Eyring dashpot is given by [2]:

$$\dot{\varepsilon}_E = \dot{\varepsilon}_{E0} e^{-\frac{\Delta H}{kT}} \sinh(\frac{\upsilon \sigma}{kT}) \tag{4.13}$$

where $\dot{\varepsilon}_{E0}$ is a constant pre-exponential factor, ΔH represents the energy barrier

height, υ is the activation volume for the molecular event, and k, σ and T are Boltzmann constants given by 1.38x10^{-23}Joules/Kelvin, applied stress and absolute temperature, respectively. Under high stress levels ($\upsilon\sigma > 3kT$) the hyperbolic sine term can be approximated to $\dfrac{1}{2}\exp(\dfrac{\upsilon\sigma}{kT})$, thus Equation (4.13) can be simplified as

$$\frac{\partial \ln \dot{\varepsilon}_E}{\partial \sigma} = \frac{\upsilon}{kT} \tag{4.14}$$
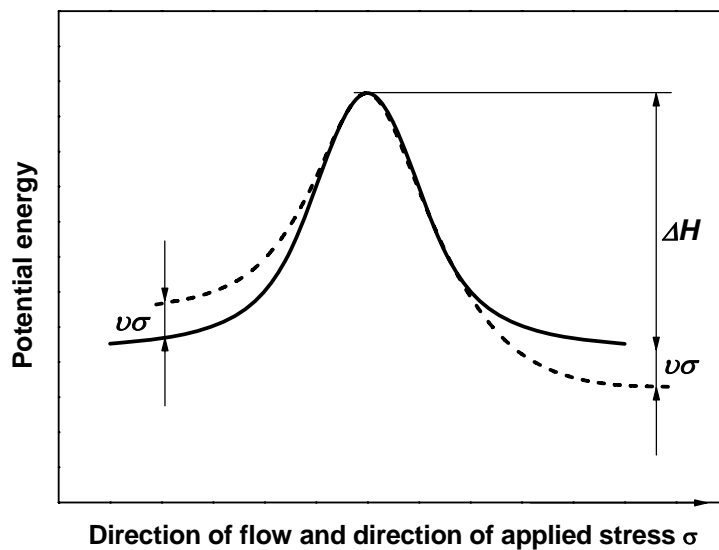

Figure 4.3: Schematic diagram of the Eyring model with activated process for creep.
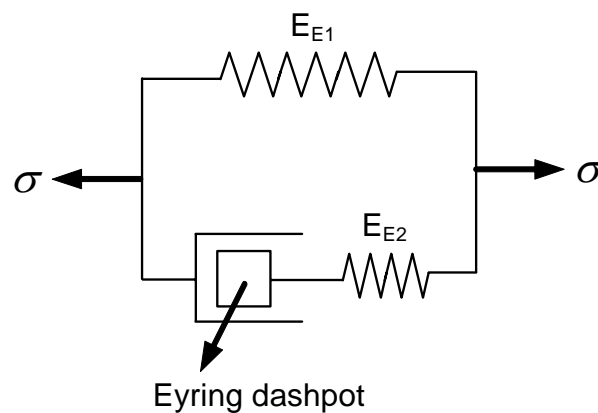
Figure 4.4: Eyring's modification of the standard linear solid with an activated dashpot.

Finally, approximate values for the activation volume of the tested specimens can be obtained from the high stress levels of σ_1 and σ_2

$$\upsilon = kT \frac{(\ln \dot{\varepsilon}_E)_{\sigma_2} - (\ln \dot{\varepsilon}_E)_{\sigma_1}}{\sigma_2 - \sigma_1} \qquad (4.15)$$

where $\dot{\varepsilon}_E$ is taken as the secondary creep rate. The activation volume is considered to represent the volume of the polymer segment which has to move as a whole in order for plastic deformation to occur [2].

4.2.3 Findley power law

Considering that the creep curves for many polymers are similar to those of some metals, some authors have proposed empirical mathematical models to represent the creep behavior of plastics. Among them, Findley et al. [1] proposed the following empirical power equation, which can describe the creep behavior of many polymers with good accuracy over a wide time scale

$$\varepsilon_F = \varepsilon_{F0} + \varepsilon_{F1} t^n \qquad (4.16)$$

or in terms of creep compliance $J_F = \varepsilon_F/\sigma$,

$$J_F = J_{F0} + J_{F1} t^n \qquad (4.17)$$

where the subscript F indicates the parameters associated with the Findley power law, ε_F and J_F are strain and compliance, respectively, and n is a constant independent of stress and generally less than one. ε_{F0} and J_{F0} are the time-independent strain and compliance, and ε_{F1} and J_{F1} the coefficient of the time-dependent term. ε_{F0} and ε_{F1} are functions of stress and environmental variables including temperature and moisture etc. The creep time t may be taken to represent a dimensionless time ratio t/t_0, where t_0 is unit time. In this case ε_{F1} has the dimensions of strain, i.e., dimensionless. When t is taken to have the dimensions of time then ε_{F1} has the dimension of (time)$^{-n}$.

Rearranging Equation (4.17) and taking logarithms yields

$$\log(\varepsilon_F - \varepsilon_{F0}) = \log \varepsilon_{F1} + n \log t \tag{4.18}$$

Thus, the curve of $\log(\varepsilon_F - \varepsilon_{F0})$ versus $\log t$ predicts a straight line with slope n and intercept at unit time of ε_{F1}. If n is independent of stress and state of stress, curves under various stresses should be in parallel.

Differentiating Equation (4.16) and the creep rate $\dot{\varepsilon}_F$ of Findley power law yields

$$\dot{\varepsilon}_F = \frac{n \varepsilon_{F1}}{t^{1-n}} \tag{4.19}$$

Here when creep time $t \rightarrow \infty$, thus $\dot{\varepsilon}_F(\infty) \rightarrow 0$. This case is applicable for polymers that do not exhibit a pronounced secondary creep stage, especially under low stress level. The Findley power law has been widely applied to express stress-strain-time relationships for viscoelastic materials.

4.3 Prediction methods

In practical applications of polymers, creep is a long-term deformation, especially under small applied load. Consequently, numerous attempts have been made over past decades to explore and develop effective and applicable methods, constitutively or mathematically, to rationally predict the long-term performance through short-term experiments [1, 2]. In this study, two kinds of approach, creep models and the time-stress-temperature superposition principle, are applied to accomplish this target. The validity of the methods is compared and discussed in the result sections.

4.3.1 Creep models

The Burgers model and Findley power law are also considered as predictive models. They are applied with unchanged model parameters simulated from the data in a short time scale to predict the experimental data in a large time scale. The validity of prediction of the models can be determined.

4.3.2   Time-temperature-stress superposition principle (TTSSP)

The most acceptable methods for realizing long-term prediction involve use of the time-temperature-stress superposition principle, which implies that viscoelastic behavior at one temperature or stress can be related to that at another temperature or stress by a change in the time scale only. The detailed procedure is that creep tests performed at different temperatures and stress levels for short times can be shifted along the time scale to construct a master curve at a reference temperature and stress level [2, 158]. This shifting scheme indicates that as stress level or temperature increases, molecular relaxation accumulates at a constant rate, and that the underlying mechanism of creep remains unchanged. The free volume theory is often applied to represent this molecular mobility. Free volume is considered as the void space available for motion of a polymer segment. The TTSSP was deduced by Luo et. al. [159] and is introduced here briefly.

According to free volume theory, the viscosity of material, η, can be related to the fractional free volume, f, via the Doolittle equation [135]

$$\ln \eta = \ln A + B(\frac{1}{f} - 1) \qquad (4.20)$$

where A and B are material constants. This function is the fundamental of time-temperature superposition.

Assuming that the change in the fractional free volume is linearly dependent on the stress change as well as the temperature change, the fractional free volume can be given as

$$f = f_{ref} + a_T(T - T_{ref}) + a_\sigma(\sigma - \sigma_{ref}) \qquad (4.21)$$

where a_T and a_σ are the thermal- and stress-induced expansion coefficients of the fractional free volume, respectively. T and σ are temperature and stress, respectively, where the data are to be shifted. f_{ref}, T_{ref}, and σ_{ref} are the fractional free volume, temperature, and stress at the reference state, respectively.

Assume there exists a temperature-stress shift factor, $a_{T\sigma}$, which satisfies

$$\eta(T,\sigma) = \eta(T_{ref},\sigma_{ref})a_{T\sigma} \qquad (4.22)$$

then combining Equations (4.20) and (4.22) yields

$$\log a_{T\sigma} = -C_1 \left| \frac{C_3(T-T_{ref}) + C_2(\sigma-\sigma_{ref})}{C_2 C_3 + C_3(T-T_{ref}) + C_2(\sigma-\sigma_{ref})} \right| \qquad (4.23)$$

where $C_1 = \dfrac{B}{2.303}$, $C_2 = \dfrac{f_{ref}}{a_T}$, $C_3 = \dfrac{f_{ref}}{a_\sigma}$.

In addition, if the stress shift factor at a constant temperature, a_σ^T, and the temperature shift factor under a constant stress level, a_T^σ, are defined, then by changing the shifting sequence of temperature or stress we have

$$\eta(T,\sigma) = \eta(T,\sigma_{ref})a_\sigma^T = \eta(T_{ref},\sigma_{ref})a_T^{\sigma_{ref}} a_\sigma^T = \eta(T_{ref},\sigma)a_T^\sigma = \eta(T_{ref},\sigma_{ref})a_\sigma^{T_{ref}} a_T^\sigma$$

$$(4.24)$$

Consequently, it yields

$$a_{T\sigma} = a_T^{\sigma_{ref}} a_\sigma^T = a_\sigma^{T_{ref}} a_T^\sigma \qquad (4.25)$$

It is shown in Equation (4.25) that the time-dependent viscoelasticity over a short time period at different temperatures and stress levels can be shifted along the time scale to construct a master curve with a large time scale at a reference temperature and stress level.

If there is no stress change, Equation (4.23) reduces to the WLF equation [2, 158]

$$\log a_T = \frac{-C_1(T-T_{ref})}{C_2 + (T-T_{ref})} \qquad (4.26)$$

Using the temperature shift factor, a_T, the nonlinear creep behavior can be described by the reduced time, t/a_T

$$J(T,t) = J(T_{ref}, t/a_T) \qquad (4.27)$$

Additionally, if the temperature is kept constant, Equation (4.23) reduces as

$$\log a_\sigma = \frac{-C_1(\sigma - \sigma_{ref})}{C_3 + (\sigma - \sigma_{ref})} \tag{4.28}$$

Using the stress shift factor, a_σ, the nonlinear creep behavior can be described by the reduced time, t/a_σ

$$J(\sigma, t) = J(\sigma_{ref}, t/a_\sigma) \tag{4.29}$$

In the current investigation, time-temperature superposition is applied to PA66 nanocomposites, while time-stress equivalence is used for PP nano-composites.

5 Creep Characterization of Nanoparticle/PA System

5.1 Tensile properties of nanoparticle/PA systems

Before considering the creep results, it was important to know the tensile properties of the nanocomposites. The ultimate tensile strength (UTS) or the yield stress of the material was a basic reference value for the creep experiments.

Tensile experiments were performed at a crosshead speed of 2 mm/min at 23 °C, and 5 mm/min at 50 °C and 80 °C. The Young's modulus, UTS and elongation at failure/necking with relative deviation are shown in Figures 5.1, 5.2, and 5.3, respectively. From Figure 5.1, it can be seen that the modulus of each material decreased with increasing temperature. In general, the Young's moduli of the composites were slightly higher than that of the matrix, showing the reinforcing effect of nanofillers. Among the materials, 21/PA exhibited the highest modulus at 23 °C and 80 °C by 21 % and 23 %, respectively, compared to PA66. At 50 °C, 21-SM/PA exhibited the highest modulus by 37 % compared to the matrix.
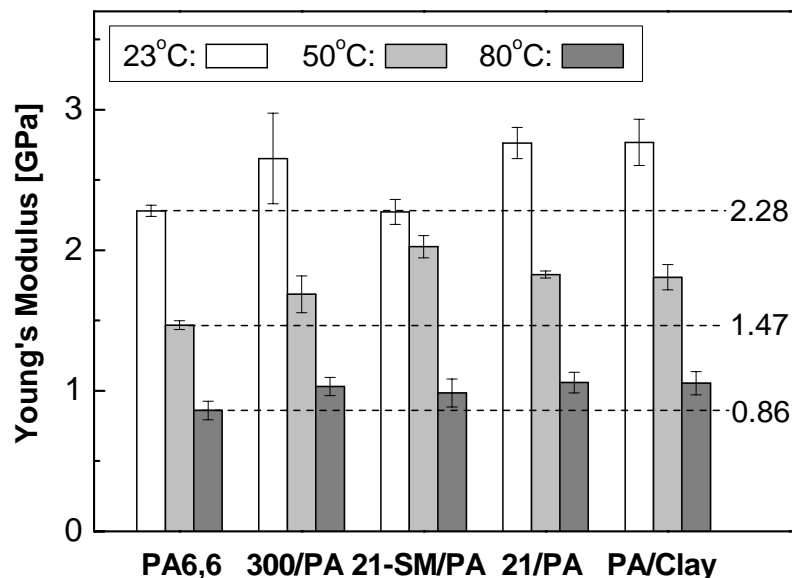
Figure 5.1: Young's modulus of PA66 and nanocomposites at different temperatures. The dashed line shows the base value of neat matrix at the corresponding temperature.

The UTS of the composites became slightly lower at room temperature and increased by less than 10 % at elevated temperatures, compared to that of the matrix, as shown in Figure 5.2. However, the ductility of the nanocomposites obviously deteriorated at both ambient and elevated temperatures, as illustrated in Figure 5.3. The total elongation of the nanocomposites decreased by more than 30% at high temperatures, while they showed some degree of brittleness at ambient temperature.
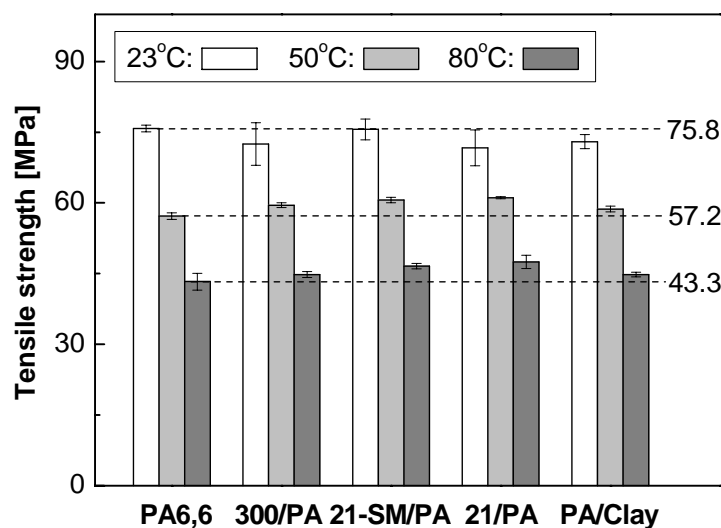
**Figure 5.2:** Ultimate tensile strength of PA66 and nanocomposites at different temperatures. The dashed line shows the base value of neat matrix at the corresponding temperature.
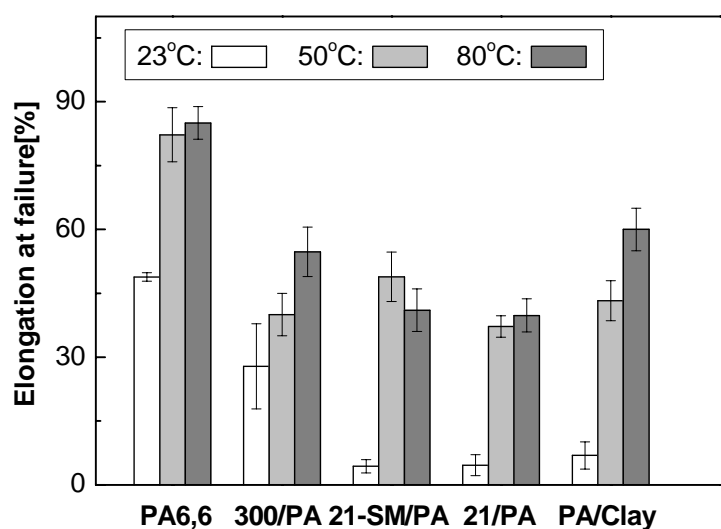

Figure 5.3: Tensile elongation at failure of PA66 and nanocomposites at different temperatures.

Overall, it was clearly shown that the quasi-static mechanical properties of the composites were not seriously diminished by the addition of nanofillers.

5.2 Creep results and general discussions

In our preliminary experiments [87], the creep failure behaviors of PA66 and TiO_2 nanoparticle filled composite were first observed under a high load of 80 % of the static UTS (about 60 MPa), which presented some interesting results. In order to comprehensively understand the influence of different nanofillers on the creep behaviors of matrix under various stresses and different temperatures, a systematic study of the creep performance of nanocomposites was first carried out at three load levels (20, 30 and 40 MPa) at room and elevated temperatures (23, 50 and 80 °C). Therefore, nine testing conditions were considered in total. The primary and part of the secondary creep stages were investigated over a moderate time scale for 200 hours. The creep deformation, isochronous stress-strain relationship, creep rate and creep compliance of different kinds of nanofiller modified PA66 are discussed [88] in the following subsections.

5.2.1 Creep deformability and isochronous stress-strain relationship

The experimental curves of creep strain versus time of PA66 and 21/PA under the high stress of 80 % of each UTS are presented in Figure 5.4. It can be clearly seen that the materials underwent the complete creep stages described earlier. At the beginning of loading, both materials exhibited relatively large instantaneous deformation due to the very high stress level. It took about 100 hours for the materials to move from the primary to the secondary stage. In the secondary creep period, the strain increased markedly with time from 30 % to 60 % for PA66 and from 15 % to 30 % for 21/PA, respectively (Figure 5.4). After about 600 hours the specimens entered the accelerating tertiary process and finally failed, with serious viscous flow and advanced necking. It is also noteworthy to point out that the time-dependent deformation of the pure matrix was significantly reduced by the addition of nanoparticles. However, the creep lifetime to failure was not obviously influenced by loading nanofillers, as shown in Figure 5.4.

The representative creep curves of the tested specimens under 40 MPa are illustrated in Figure 5.5 at (a) 23 °C, (b) 50 °C, and (c) 80 °C. Because creep failure was not considered under those conditions, only the primary and unfinished secondary creep stages were observed.
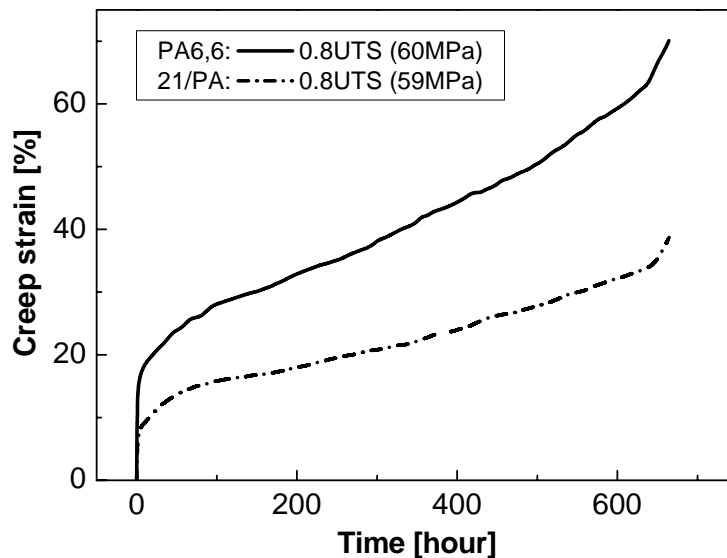
Figure 5.4: Creep strain versus time of PA66 and 21/PA tested under higher stress level of 80 % of each UTS (~60MPa) at 23 °C.
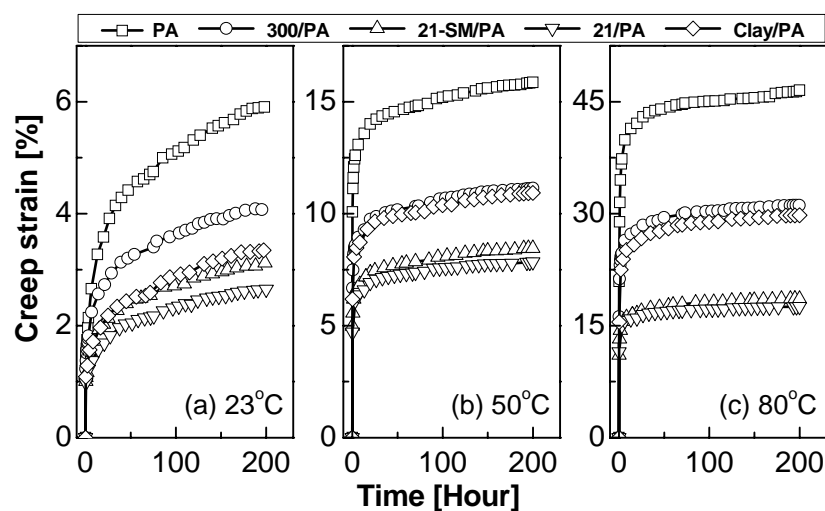
Figure 5.5: Sample curves of creep strain versus creep time of PA66 and nano-composites tested under lower stress level of 40 MPa at **(a)** 23 °C, **(b)** 50 °C and **(c)** 80 °C.

From Figure 5.5, it can be observed that the overall deformation of both the nanocomposites was noticeably less than that of neat matrix, demonstrating the creep resistant influence of the nanofillers. Additionally, the deformations of 21-SM/PA and Clay/PA were very similar at 23 °C, as shown in Figure 5.5(a), while the creep strains of 300/PA and Clay/PA, and 21-SM/PA and 21/PA were of a similar level at 50 °C and 80 °C, as shown in Figures 5.5(b) and (c). Generally, among the nanocomposites 21/PA showed the best non-deformability under each condition.

To detail the deformation behaviors of all tested specimens, the isochronous stress-strain curves at 1, 10 and 100 hours were obtained from the creep data and are presented in Figures 5.6, 5.7, and 5.8 at 23 °C, 50 °C, and 80 °C, respectively. For the 1-hour isochronous curves shown in Figure 5.6(a), the creep strains of small nanoparticle and nanoclay filled PA66 were very close but less than that of neat PA.
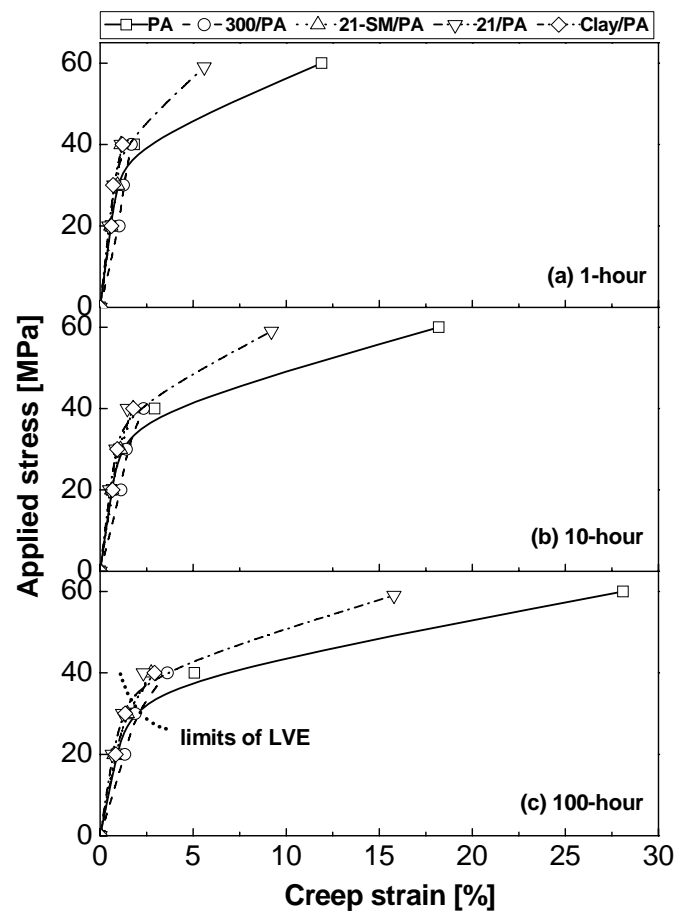
Figure 5.6: The isochronous stress-strain relationships of PA66 and nano-composites at 23 °C and **(a)** 1 hour, **(b)** 10 hours, and **(c)** 100 hours.

However, after 10 hours and even longer, 21-SM/PA and Clay/PA demonstrated similar deformability while 21/PA possessed the best dimensional stability, as shown in Figures 5.6(b) and (c). It is noteworthy to point out that 300/PA exhibited a different isochronous stress-strain relationship, with larger deformation under stress not higher than 30 MPa than the other nanocomposites and neat matrix.

The 1-hour isochronous strain of the composites showed fairly good linearity below the stress of 40 MPa. However, the composites displayed nonlinearity above 40 MPa and especially under 60 MPa. Neat matrix PA66 showed nonlinearity from stress of less than 40 MPa and much more seriously below 60 MPa, as shown in Figure 5.6(a).
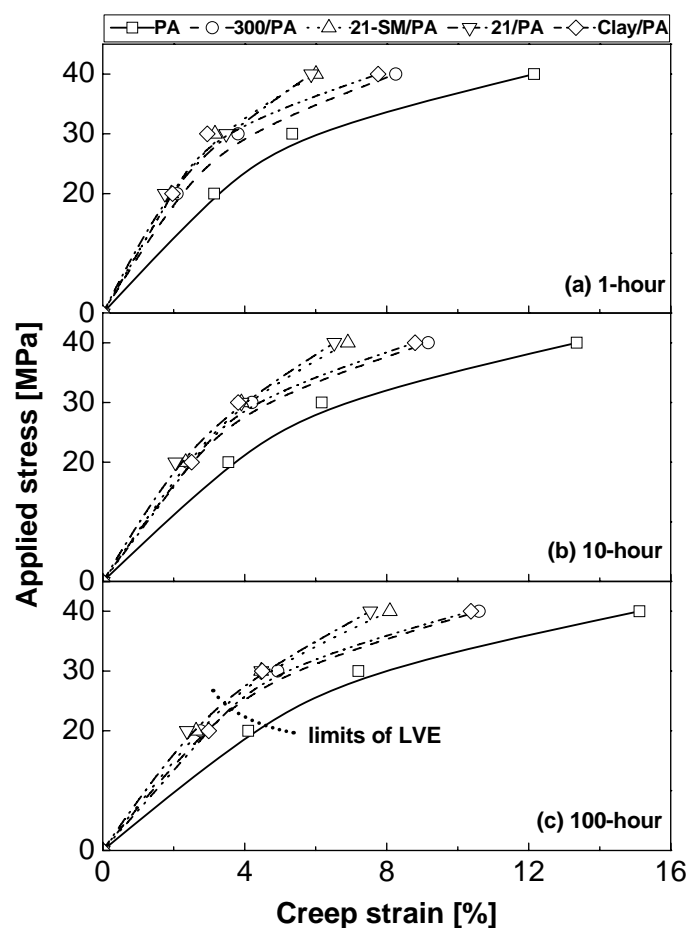
Figure 5.7: The isochronous stress-strain relationships of PA66 and nanocomposites at 50 °C and **(a)** 1 hour, **(b)** 10 hours, and **(c)** 100 hours.

This finding indicated that the nanofillers extended the linear limits and retained the linearity of the matrix for short-term response. With increasing time, the linear relationship between the isochronous stress and strain deteriorated, particularly under higher stress levels, i.e., 40~60 MPa. However, over a large time scale the nanocomposites enhanced their linear limits even under a stress of around 33 MPa, which was slightly higher than the linear limit of PA66, as shown by the dotted line in Figure 5.6(c). Additionally, among the composites small nanoparticles effected the best improvement in linearity, then nanoclay, and large particles the worst.

At elevated temperatures, i.e., 50 °C and 80 °C, the creep deformability of each material became much stronger than that at 23 °C under the same stress level, as shown in Figures 5.7 and 5.8. Another difference from the case at 23 °C was that the deformability of each material at the high temperatures was relatively
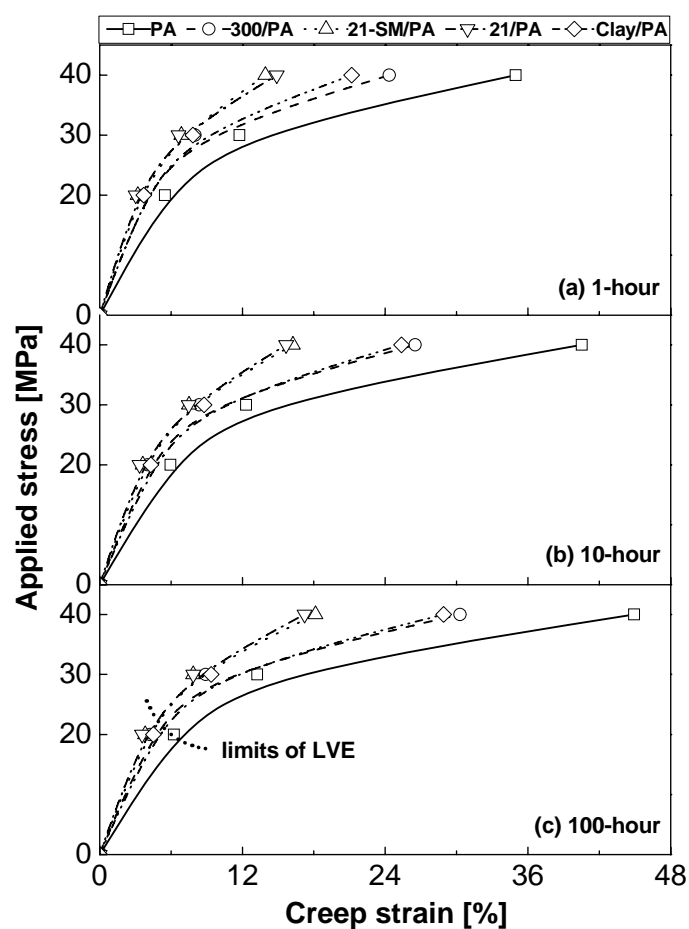

Figure 5.8: The isochronous stress-strain relationships of PA66 and nano-composites at 80 °C and **(a)** 1 hour, **(b)** 10 hours, and **(c)** 100 hours.

constant with increasing time after a large instantaneous deformation. This phenomenon indicated that there was no pronounced creep deformation in the secondary creep stage, which was also confirmed explicitly for example in Figures 5.5(b) and (c). From Figure 5.7, three regimes of deformability can be clearly discerned for the tested specimens: the strongest deformability (PA), the intermediate (300/PA and Clay/PA), and the best non-deformability (21-SM/PA and 21/PA). The superior reinforcing effectiveness of small particles was again verified. Naturally the nonlinearity and instantaneous deformation of the materials tested at 80 °C was increased considerably compared with that at 50 °C for corresponding specimens, whereas the linearity did not changed much with increasing time at each constant temperature for each specimen, due to the non-sensitivity to time of secondary creep deformation, as shown in Figures 5.7 and 5.8. There were also three regimes of linearity of isochronous stress-strain relationship corresponding to deformability. The limits of the linearity at 50 °C (in between 20 to 30 MPa) were higher than those at 80 °C (around 20 MPa) but lower than those at 23 °C (above 30 MPa) for the large scale of time, as indicated by dotted lines in Figures 5.6(c), 5.7(c) and 5.8(c).

The materials exhibited different creep deformability and linearity of the isochronous stress-strain relationship at various temperatures and stress levels, indicating that the filled materials with changed amorphous structures and crystalline morphology had diverse responses to temperature, stress level and applied creep time. A representative structure of nanofiller-semicrystalline polymer composites is schematically illustrated in Figure 5.9. The essential elements, including crystallized chains, amorphous and entanglement regions, segment and crystalline bridging between fillers, polymer-filler junction, and intercrystalline tie molecules, are considered. Crystallized chains could react rapidly to external mechanical action and for example immediately undertake persistent load [160]. With increasing time, the amorphous regions of the materials may thereafter bear load, which normally is a linear or nonlinear viscoelastic processes with orientational strain hardening [161]. In the case of this study the glass transition temperature (T_g) of the nanocomposites was slightly increased (less than 4 °C)
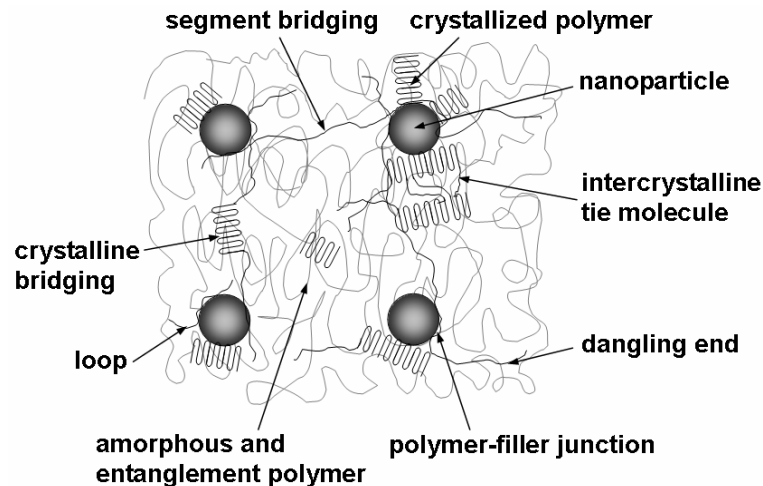
Figure 5.9: Schematic representation of a uniformly dispersed nanoparticle/polymer structure. (Based on the assumption that the particles with 1 vol. % have a diameter of 20 nm, the polymer chains have a diameter of 1 nm, the interparticle distance is 60 nm, and the crystal lamellae thickness is about 10 nm).

compared to that of the matrix. The crystallinity of the composites was only slightly decreased. However, the crystalline structure and morphology were altered significantly [162] with micron-sized rather than sub-micron or nanometric spherulites in neat matrix, as shown in Figure 5.10.

At room temperature, the materials were in a glassy state and the mobility of polymer segments was highly restricted. The load bearing ability was very similar for the composites due to their similar crystallinity. Additionally the external loads were in the elastic limits of the composites. These might be reasons that all the composites exhibited a linear relationship between isochronous stress and strain in short response, as shown in Figure 5.6(a). With increasing time the rate process in amorphous regions was activated and dominant under a high stress level (40 MPa), resulting in large deformation. From Figure 5.6(c) a threshold stress around 30 MPa might also be identified, below which the materials exhibited linearity. The threshold stress of the composites was slightly higher than that of neat PA66, as marked by a dotted line in the figure.

For comparison, the amount of fillers per cubic millimeter of matrix is listed in Table 3.3, based on the assumption of uniform filler dispersion. Although agglomerate
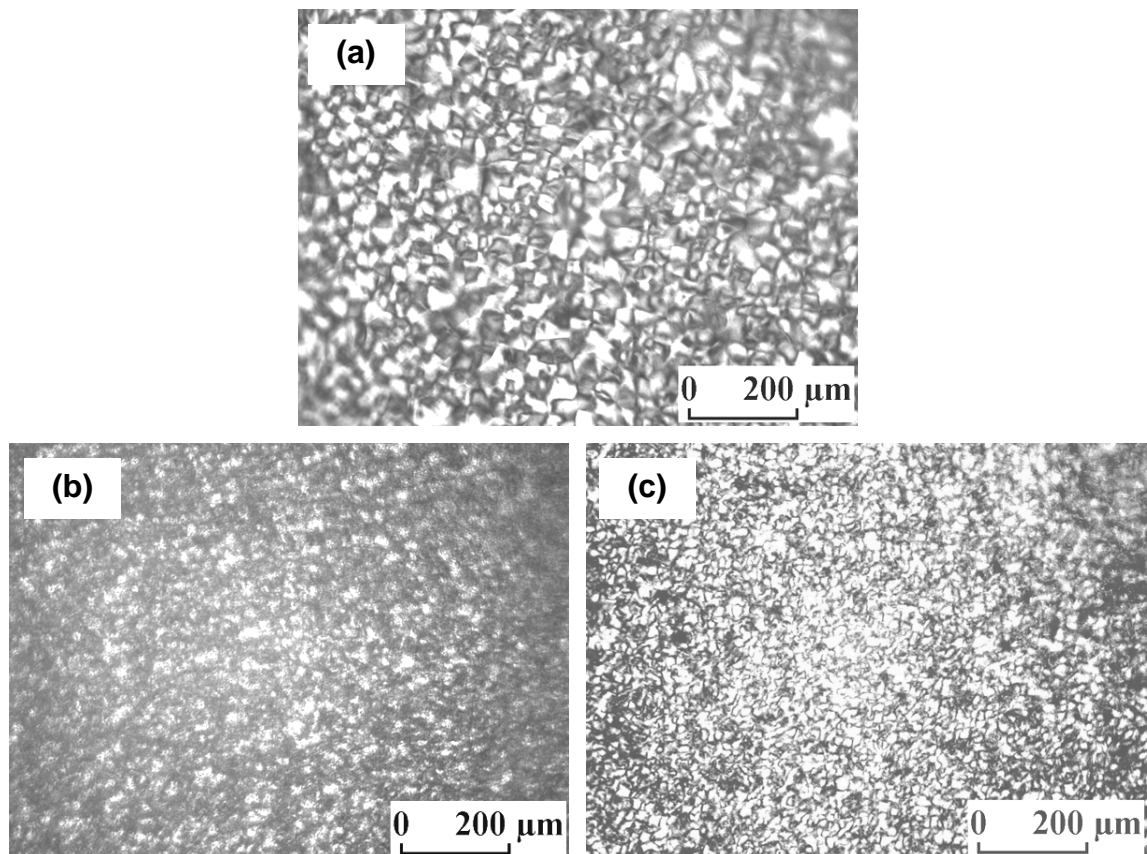
Figure 5.10: Polarizing optical micrographs showing different spherulite morphology of **(a)** neat PA, **(b)** 300/PA, and **(c)** 21/PA.

particles were unavoidable, the huge number of dispersed single particles could form a network [163], which cooperated with the matrix via interphase, bridgings and junctions to bear load and improve the immobility of polymer chains, as illustrated in Figure 5.9. In addition, interparticle distance is normally considered an important parameter in particulate/polymer composites [165, 166]. The ratio of interparticle distance to particle diameter as a function of filler volume content is presented in Figure 5.11 for consideration. The ratio decreases rapidly with increasing filler concentration below 2 vol. % and reaches a slowly decreasing stage when particle content is higher than 10 vol. %. Although the ratio is similarly 2.5 for 1 vol. % of particles, the actual distances were highly different due to their diameters.

In 21/PA composite, the huge number of fillers ($\sim 10^{12}$/mm^3) could form a very dense and stiff network [83] with close interparticle distance of ~53 nm. Considering the interphase between particles and matrix, the distance between the effective particles
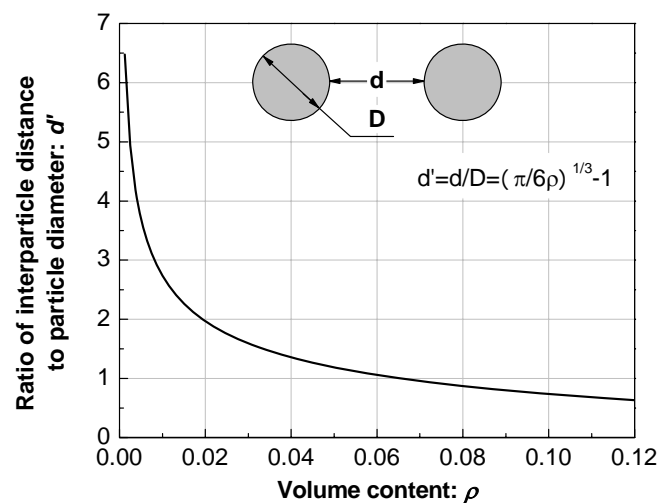
Figure 5.11: The ratio of interparticle distance to particle diameter as a function of the volume content of filler.

with surrounding interphase was less than 53 nm. The available motion for polymer chains was highly constrained within this space. In this way 21/PA became stiff and resistant to deformation. In the case of surface modified nanoparticles, although a better dispersion could possibly be achieved, the surface strength between particle and matrix, a key factor to affect the reinforcing performance, might deteriorate due to modification, resulting in an inferior performance to that of 21/PA. Considering the as-received clay particles with a diameter of 35 μm and individual platelets with size of 100~500nm$\square$1nm, it was very difficult to obtain full exfoliation into single platelets in melt extrusion. The shear stress through the interphase could make the non-exfoliated or agglomerate layers slip [28, 164], especially under high stress levels and elevated temperatures. Consequently, Clay/PA showed a slightly worse non-deformability and linearity than 21/PA. In the case of large particle filled PA, the amount of filler per cubic millimeter of matrix was about 10^9, far less than that of small particles by several orders of magnitude. The diameter (300 nm) of large particles was in the submicron level and any defects or agglomerates resulting from them were in the same or micron level, which would considerably impair the properties of the bulk material. Additionally, the network with relatively large interparticle distance (~750 nm) was not stiff and had little ability to restrict the mobility of polymer chains [163] distant from the particles in a small range, which led

to inferior non-deformability with creep strain <2 % under stress below 30 MPa compared to that of neat matrix. However, the resistance to deformation of large particles increased under 40 MPa with strain >3.5 %, as shown in Figure 5.6(c).

At the point near the glass transition temperature, i.e., 50 °C, the polymer chains became active and the mobility of chains was also markedly increased due to thermal activation. Deformability, such as the instantaneous deformation of each material at 50 °C, was much more severe than that at 23 °C. The deformation after the transient response, however, was insensitive to the rate process [167], which was a result of the rapid orientational hardening of amorphous regions once the specimen was persistently loaded and the stress was not high enough to produce further deformation of the polymer. This was confirmed by the fact that the creep strain of each specimen increased gradually and thus the linearity was changed slightly with increasing time from 1 hour to 100 hours, as shown in Figure 5.7. In addition, the composites showed fairly good creep resistance compared to neat PA66 at 50 °C, with reduced deformation and enhanced linear viscoelasticity (LVE). The limits of LVE of the tested specimens were between 20 and 30 MPa, appreciably lower than those at 23 °C. The isochronous stress-strain curves in Figure 5.7 show three apparent regimes, as mentioned above. The resulting performance of 21/PA, very similar to that of 21-SM/PA, indicated that the network of particles and interphase with good interfacial strength played a key role in restricting the mobility of polymer chains. Concerning interparticle distance, large particles showed some resistance to relatively large deformation, as mentioned earlier. In the case of Clay/PA, although the interlayer distance was smaller than that of 300/PA, shear stress resulting from large deformation could cause slippage in non-exfoliated layers and agglomerate clay particles [28, 164], which impaired creep resistance, so that Clay/PA displayed a similar performance to 300/PA, as shown in Figure 5.7.

The materials entered into a rubbery state at 80 °C above T_g. The polymer chains were strongly activated thermally and deformed easily, and thus the load-bearing capability of the bulk specimens weakened markedly. Consequently, the deformability and linearity of viscoelasticity of the measured specimens at 80 °C showed a similar tendency, but to a much more severe extent, to those at 50 °C, as

shown in Figure 5.8. After severe instantaneous deformation, the creep strain and the nonlinear viscoelasticity (NLVE) of each specimen increased weakly from the short time span to both intermediate and relatively long time scales, as shown in Figures 5.8(a), (b), and (c) at 1, 10, and 100 hours, respectively. Similar deformability with three regimes was again displayed. The limits of the LVE were somehow higher than 20 MPa for the composites, and somewhat lower than 20 MPa for the matrix, as approximately indicated in Figure 5.8(c) with the dotted line.

In discussion of the isochronous curves, it can be concluded that the deformability and NLVE of each specimen increased with increasing temperature, stress level and time scale, and non-deformability and linearity were enhanced in the hierarchy of (PA66)→(300/PA, Clay/PA)→(21-SM/PA, 21/PA), where the materials in the same bracket displayed similar deformation and linearity. As an additional quantitative comparison, the material with the maximum decrement in deformation compared to PA66 after 200 creep hours under each condition is listed in Table 5.1. For almost all conditions that was 21/PA, which exhibited the best performance with the most decreased strain by 62 % under 80°C/40MPa, revealing that smaller nanoparticles were the optimum candidate to improve the dimensional stability of bulk material in this study.

Table 5.1: The nanocomposites with maximum decrement by percentage in creep strain at 200 hour and creep rate compared to PA66.

		Specimen	Creep strain decrement	Specimen	Creep rate decrement
20 MPa	23 °C	21/PA	31 %	21-SM/PA	62 %
	50 °C	21/PA	41 %	21-SM/PA	46 %
	80 °C	21/PA	43 %	21/PA	65 %
30 MPa	23 °C	21/PA	20 %	21-SM/PA	31 %
	50 °C	21/PA	38 %	21/PA	38 %
	80 °C	21-SM/PA	41 %	21-SM/PA	65 %
40 MPa	23 °C	21/PA	55 %	21/PA	58 %
	50 °C	21/PA	50 %	21/PA	55 %
	80 °C	21/PA	62 %	21/PA	67 %

5.2.2 Creep rate

In addition to deformation, the dimensional stability of materials is characterized by another important parameter, namely creep rate, which defines the velocity of creep deformation. The representative curves of creep rate as a function of time are shown in Figure 5.12 for PA66 and 21/PA under different stress levels at 23 °C. In the observed time span, creep rate showed a similar trend to creep deformation. In the primary stage, the creep rate began at a relatively high value while decreasing rapidly with time, which might be due to orientational hardening of the materials [168] after instantaneous deformation under sudden and thereafter persistent stress. After a period of about 50 hours, the creep rate entered a relatively steady state, called the secondary creep stage, in which a dynamic equilibrium of polymer structure evolution and external load was reached. The creep rate increased with increasing stress level for each material. Under 80 % UTS the rate increased quickly after 500 hours and finally the materials failed. In addition, the creep rate was not sensitive to time under 20 Mpa, while it decreased with time under 30 and 40 MPa within the observed time scale, as shown in Figure 5.12. Similar scenarios were also observed at 50 °C and 80 °C.
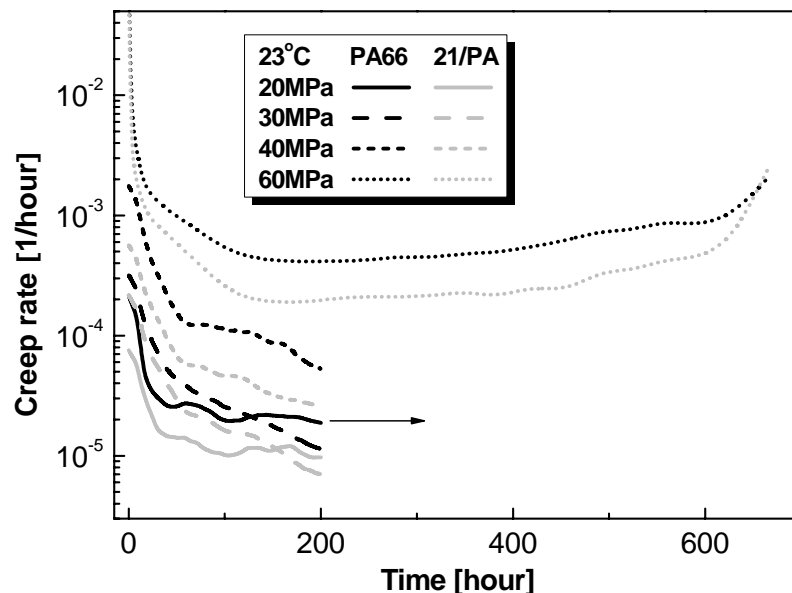
Figure 5.12: Sample curves of creep rates of PA66 and 21/PA as a function of time under different stress levels at 23 °C.

Creep rate behavior showed a more complicated dependence on temperature and stress level compared to deformation. A detailed analysis is given below.

5.2.2.1 Stress effects

To simplify discussion, the secondary creep rates of each specimen at different temperatures are directly fitted and presented as a function of stress level in Figure 5.13, from which it can be seen that the materials showed different response to stress levels.

At room temperature, the creep rate of each specimen was insensitive to stress level below 30 Mpa, while it increased greatly under 40 and 60 MPa, as shown in Figure 5.13(a). This finding indicates that the deformation increased linearly and proportionally to stress less than 30 MPa and the materials acted as linear solids, as shown in Figure 5.6. Under higher stress levels a time-dependent rate process was activated in the amorphous region [169, 170], playing an important role in influencing
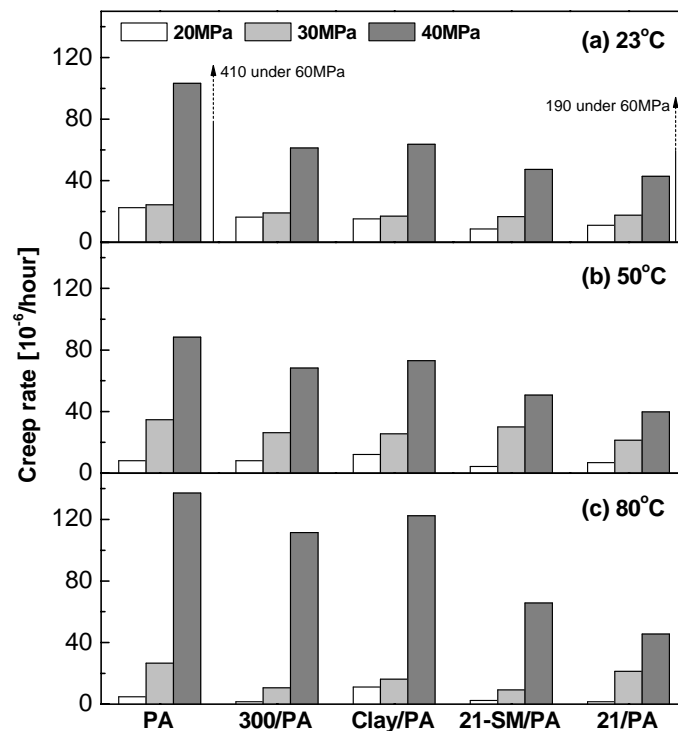
Figure 5.13: The influence of stress level on the creep rate of the tested specimens at different temperatures: **(a)** 23 °C, **(b)** 50 °C, and **(c)** 80 °C.

creep deformation. Thus the materials displayed nonlinearity with time. At elevated temperatures, the stiffness of the specimens weakened and the creep rate increased nearly exponentially, especially at 80 °C, as illustrated in Figures 5.13(b) and (c). These phenomena imply that the materials easily showed nonlinear properties at high temperature even under low stress, which was coincident with the results of deformation, as shown in Figures 5.7 and 5.8.

As for the influence of nanofillers on the creep rate, they displayed similar reactions to external load, i.e., the creep rates of all nanocomposites were generally decreased to some extent compared to that of neat PA66 under each temperature or stress level. The decrease in creep rate of composites was much more obvious under a higher stress level than that of PA66, as shown in Figure 5.13. This finding indicates that the rate process activated under high stress level in the amorphous region was significantly constrained by the presence of nanofillers. Among the nanofillers, small particles displayed much greater effectiveness in decreasing creep rate than did large particles and clay layers; large nanoparticles and nanoclay layers again displayed a similar creep rate; surface modification had no obvious influence on decreasing creep rate.

As analyzed above, interparticle distance might play a key role in influencing the creep rate. For small nanoparticle filled PA66, the relatively close interparticle distance (~53 nm) and the resulting dense network contributed greatly to slowing deformation. However, the large interparticle distance and resulting sparse network in large particle filled PA66 were incapable of significantly decreasing the creep rate. In Clay/PA, the non-exfoliated particles and aggregates would slip due to shear stress, especially under higher stress levels, giving rise to a high creep rate, as shown in Figure 5.13. The maximum decrement in creep rate under each condition is listed in Table 5.1. Among the materials 21/PA exhibited the minimum value, 67 % less than that of PA66 under 80°C/40 MPa, revealing again that smaller nanoparticles were the optimum candidate to improve the dimensional stability of the bulk material.

5.2.2.2 Temperature effects

The secondary creep rates of each specimen are redrawn as a function of temperature in Figure 5.14 under (a) 20 MPa, (b) 30 MPa, and (c) 40 MPa. It can be found from the figures that the materials showed very different and complex dependence on temperature under various stress levels. As discussed above, the specimens exhibited both linear and nonlinear viscoelasticity under the stress levels of 20 MPa and 40 MPa, respectively, within the range of applied temperature; under about 30 MPa the materials showed linear viscoelasticity at 23 °C but nonlinear viscoelasticity at elevated temperatures, indicating that around 30 MPa there was a transition state for temperature. In the following paragraphs discussion is presented according to the stress levels and the linearity of viscoelasticity of the observed samples.

(I) In the state of linear viscoelasticity: 20 MPa

The creep rate of each specimen decreased obviously with increasing temperature in the state of linear viscoelasticity, as shown in Figure 5.14(a). Under a low stress level of 20 MPa at room temperature (0.26 UTS at RT), most of the amorphous segments could not be stress activated to exhibit the creep process in a short time. With increasing time, many more segments were activated, involving a relatively high velocity of orientation of polymer chains and entanglements, and thus a higher creep rate occurred.

Although more polymer segments were thermally activated at elevated temperatures than at RT, the large instantaneous deformation showed that many segments were oriented to some extent along the stress direction in a short time, and thereafter orientational hardening made it difficult to bring about further reorientation and rearrangement of polymer chains and entanglements due to the relatively low stress level (roughly 0.35UTS at 50 °C and 0.46UTS at 80 °C, respectively), as shown in Figure 5.14.

In the nanoparticle composites, as shown in Figure 5.14, creep rate decreased with decreasing particle size at the same temperature, showing that small particles hindered polymer chain motion more efficiently than large ones. 21-SM/PAexhibited
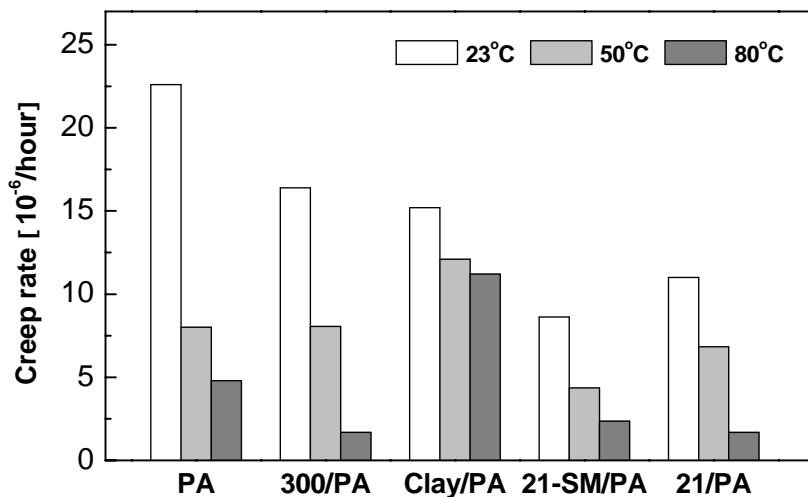
Figure 5.14: Temperature effects of creep rate for the tested specimens in the state of linear viscoelasticity under stress level of 20 MPa.

a lower creep rate at 23 °C and 50 °C, but a higher rate at 80 °C than 21/PA, indicating that surface modification was effective only under a small load level (~0.26UTS) and below glass temperature, whereas its contribution was discounted due to poor interfacial strength at 80 °C. The creep rate of Clay/PA was close to that of 300/PA at ambient temperature while much higher than that of 300/PA at 50 °C and 80 °C, implying that slippage of non-exfoliated clay particles or agglomerates occurred due to the increasing shear stress caused by marked viscous flow of the polymer above glass transition temperature.

(II) In the state of nonlinear viscoelasticity: 40 MPa

Under stress of 40 MPa the creep rate of each specimen generally increased with increasing temperature, as shown in Figure 5.15. This inverse trend in the state of nonlinear viscoelasticity indicated that the movement of polymer chains was totally different from that in the state of linear viscoelasticity. The creep rate changed only slightly, increasing or decreasing, from 23 °C to 50 °C. This might be due to the marked orientational hardening which resulted from thermal activation and high stress level and made it difficult to produce an acceleration of rate for the instantaneously oriented polymer chains. At 80 °C the polymer chains were highly thermally activated and further velocity could be stress activated to overcome the marked orientational hardening [161, 168]. However, this was not the case for 21/PA,
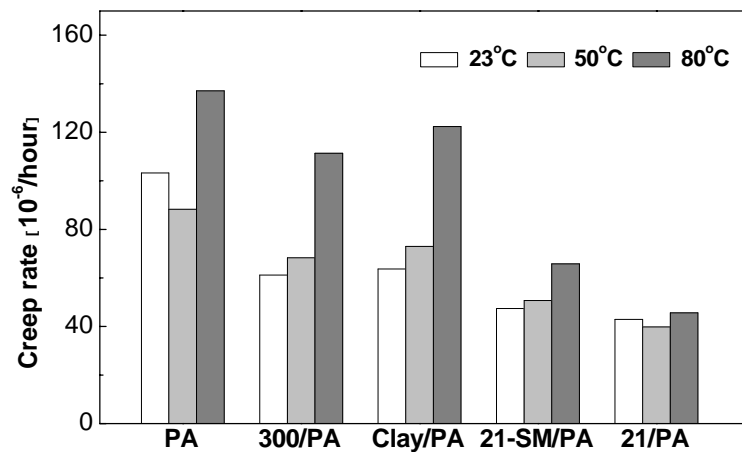
Figure 5.15: Temperature effects of creep rate for the tested specimens in the state of nonlinear viscoelasticity under stress level of 40 MPa.

in which the small particles still constrained the increase in deformation rate.

For the nanoparticle composites, as shown in Figure 5.15, creep rate decreased with decreasing particle size at the same temperature, however, much more than the corresponding value under 20 MPa, showing that many more stress activated polymer chains participated in the creep process. The creep rate of 300/PA was much greater than that of 21-SM/PA and 21/PA, confirming the above conclusion that smaller particles with close interparticle distance and a dense network were more efficient than large ones in hindering polymer chain mobility. The contribution to creep rate of surface modified particles with possible low interfacial strength was not greater than that of untreated ones. The creep rate of Clay/PA was close to that of PA/300 at all temperatures, indicating again that the slippage of non-exfoliated nanoclay layers and agglomerates, due to the shear stress caused by marked viscous flow of the polymer under high stress level, had an adverse effect.

(III) In the transition stress region: 30 MPa
As discussed above, the explicit dependence of creep rate on temperature was evident in the range of linear and nonlinear viscoelasticity, respectively. However, in the transition state from linear to nonlinear viscoelasticity, an interesting phenomenon occurred, in that the highest creep rate of each specimen occurred at 50 °C rather than at other temperatures, and the creep rate at RT was close to that
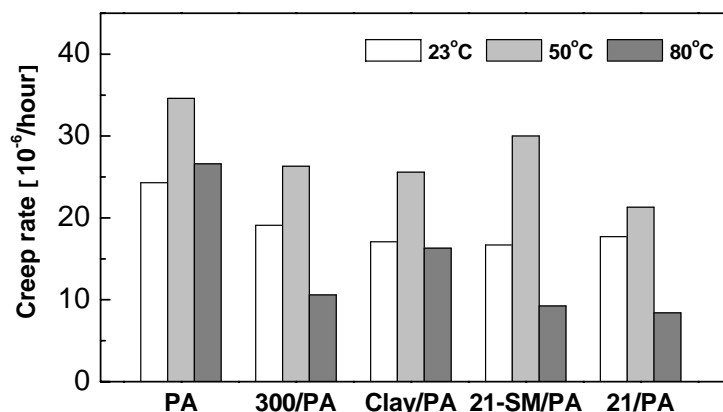
Figure 5.16: Temperature effects of creep rate for the tested specimens in the transition state under stress level of 30 MPa.

at 80 °C, as shown in Figure 5.16. A possible explanation is that the strong orientational hardening [161, 168] due to severe instantaneous deformation at 80 °C made it difficult for further activation of the rate process in amorphous regions because of the moderate stress level, which resulted in a creep rate as low as that at RT. However, at 50 °C the orientational hardening was weaker than at 80 °C, and the accelerating movement of amorphous chains could be further activated by stress with increasing time, resulting in a high creep rate under this condition.

As shown in Figure 5.16, in the nanoparticle composites, similar temperature dependence of creep rate was observed to that under 20 MPa and 40 MPa. Among the composites, 21-SM/PA and 21/PA displayed the lowest creep rate at 23 °C while 21/PA displayed the lowest rate at elevated temperatures, indicating that surface modification made no positive contribution at RT and a negative contribution to creep rate reduction at higher temperatures. The creep rate of Clay/PA was similar to that of 300/PA at ambient and elevated temperatures, implying that the slippage of non-exfoliated nanoclay layers occurred due to the shear stress resulting from the viscous flow of the polymer chains.

5.2.3 Creep compliance

The curves of creep compliance versus creep time of the tested specimens were obtained under different loads and temperatures, as shown in Figure 5.17 with the

same axial scale. It is evident from the curves that at RT and 50 °C the creep compliance of each specimen almost overlapped below the stress level of 30 MPa (except for 21/PA under 50°C/30MPa), implying that the materials displayed linear viscoelasticity. With increase in load, viscous flow became severe and was complicated by the presence of nonlinear viscoelasticity. However, at 80 °C polymer chains became much more thermally active and displayed evident nonlinear viscoelastic flow even under stress levels as low as 20 MPa. The linearity of viscoelasticity can also be confirmed by the relationship of isochronous stress-strain curves in Figures 5.6, 5.7, and 5.8.

Another interesting phenomenon in Figure 5.17 is that at 23 °C the tested specimens displayed lower compliance but a higher growth rate with time; however, at
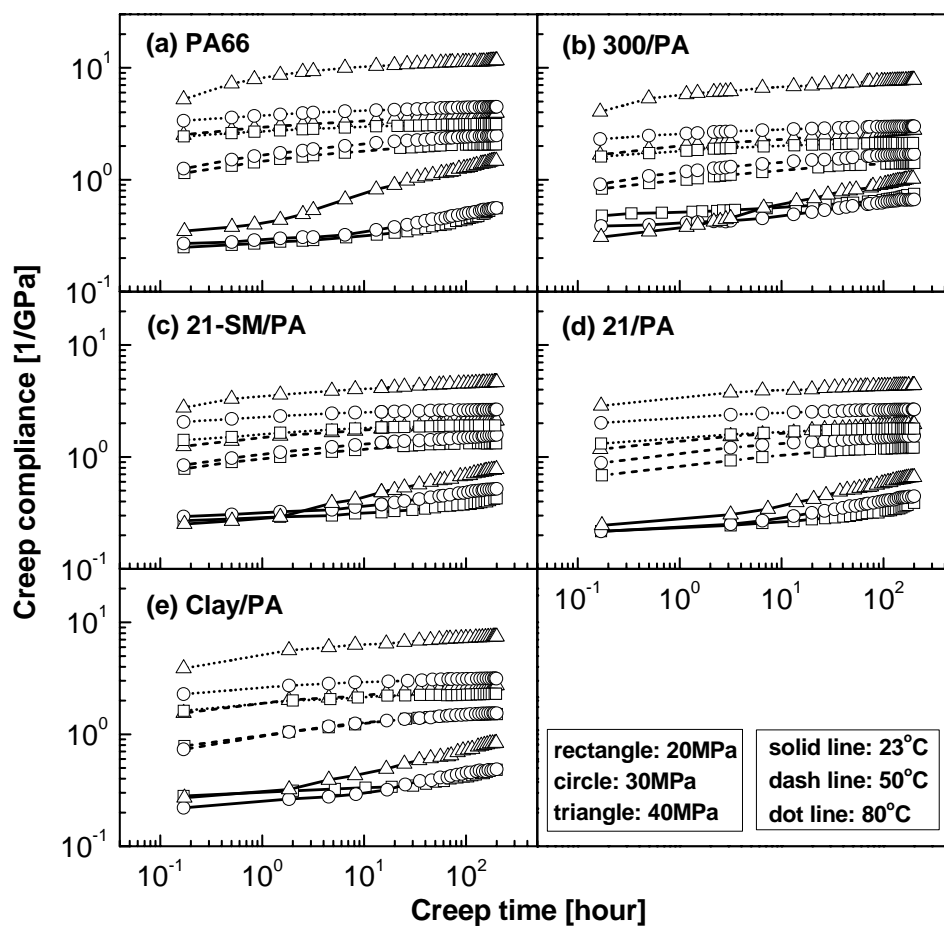
Figure 5.17: Stress and temperature dependence of creep compliance of the tested specimens: **(a)** PA66, **(b)** 300/PA, **(c)** 21-SM/PA, **(d)** 21/PA, and **(e)** Clay/PA.

temperatures above 50 °C the compliances entered plateau state with a much slower growth rate with time, illustrated in Figure 4.2.

Nanocomposites showed creep resistance by reduced compliance compared to the PA66 matrix, as illustrated in Figure 5.17. In the case of nanoparticle composites, compliance decreased with decreasing particle size at each temperature. At high temperatures, the increase in compliance of small particle filled nanocomposites was much lower than that of large particle filled nanocomposites and neat matrix. These results imply that the networks formed by small particles with narrow interparticle distance were more effective in retarding and restricting the mobility and motion of polymer chains than those formed by larger nanoparticles with greater interparticle distance. The compliance of 21-SM/PA was either close to or higher than that of 21/PA, suggesting that surface modification of particles made no contribution to reducing creep compliance. This conclusion was consistent with those for creep deformation and creep rate. Since greater numbers of clay platelets than those of the 300 nm particles were possibly dispersed in unit volume, as calculated in Table 3.3, the compliance of Clay/PA was much lower than that of 300/PA due to good load transfer between clay platelets and matrix at RT [28]. With increasing temperature marked viscous flow led to high shear stress, resulting in the slippage of clay particles and agglomerates and thus impairing their reinforcing effectiveness, until finally the compliance was almost the same as that of 300/PA.

6 Creep Characterization of Nanoparticle/PP System

6.1 Tensile properties of nanoparticle/PP system

The tensile experiments on nanoparticle/PP material system were performed at a crosshead speed of 5 mm/min at 23 °C and 50 °C. The Young's modulus, ultimate tensile strength (UTS) and tensile elongation at necking with relative deviation are shown in Figures 6.1, 6.2, and 6.3, respectively. From Figure 6.1, it can be seen that the modulus of each material decreased greatly with increasing temperature. The Young's moduli of the composites were higher than that of pure PP and increased slightly with decreasing particle size, showing the reinforcing effect of nanoparticles. Small nanoparticles made a contribution of 15 % and 8 % to the matrix modulus at 23 °C and 50 °C, respectively.

The UTS of each material decreased obviously with increasing temperature. Neither small nor large nanoparticles had any obvious effect on the UTS at constant temperature, as shown in Figure 6.2. Although the elongation at necking of the materials increased with increasing temperature, that property of the nanocomposites was slightly worse both at RT and 50 °C than that of neat PP, as illustrated in Figure 6.3.
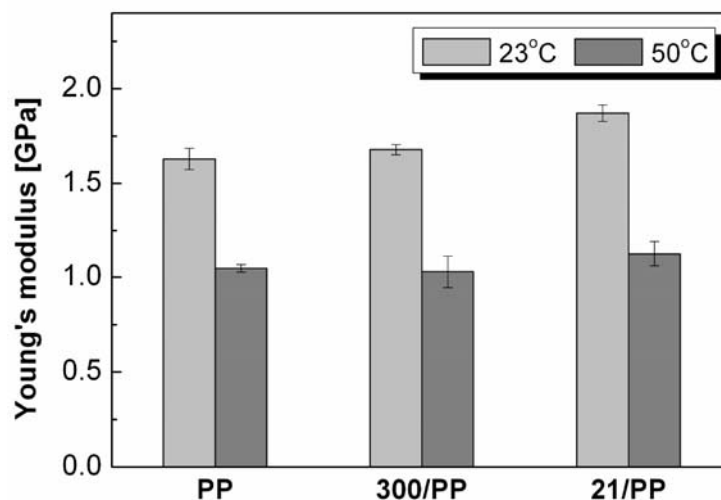
Figure 6.1: Young's modulus of nanoparticle/PP material system at different temperatures.
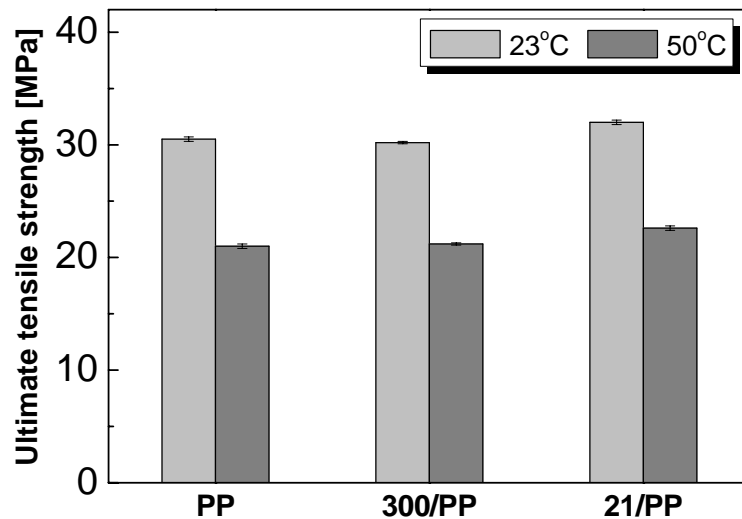
Figure 6.2: Ultimate tensile strength of nanoparticle/PP material system at different temperatures.
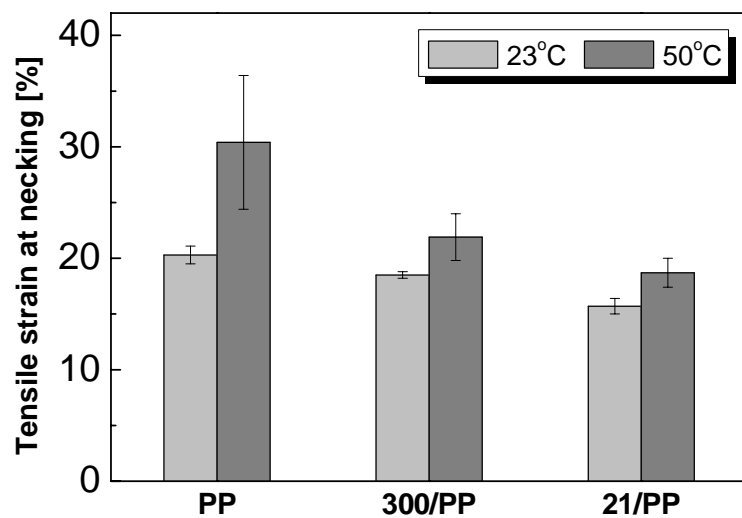
Figure 6.3: Tensile elongation at necking of nanoparticle/PP material system at different temperatures.

It can be concluded that the quasi-static tensile properties of the composites were not seriously impaired as a whole by the addition of nanoparticles.

6.2 Creep results and general discussion

Because of its low glass transition temperature (11 °C), PP is normally in a rubbery state and very soft in a room temperature environment, a characteristic which is very different from PA66. The addition of rigid nanoparticles into the PP matrix resulted in enhanced creep resistance. The dimensional stability and even the creep lifetime under certain conditions are obviously improved. Detailed results and analyses are given below.

6.2.1 Creep deformation and isochronous stress-strain relationship

The representative experimental data of creep strain versus time at 23 °C and 50 °C are shown in Figures 6.4(a) and (b), respectively, under high and moderate stress levels. The arrow in the figures indicates that the specimens were not in failure under moderate stress level within the time scope of observation. An attractive phenomenon was that the creep lifetime of 21/PP was extended by about 330 % (4.3-fold) and 230 % (3.3-fold) compared to that of pure matrix under 23°C/20MPa and 50°C/14MPa, respectively, as shown by dashed lines in Figure 6.4 . It can also be seen that the composites reinforced with small nanoparticles showed greatly reduced creep deformation under each condition; while large particle filled PP displayed only a slight enhancement except for the condition of 50°C/14MPa, under which 300/PP showed an obviously prolonged creep lifetime, enhanced by 90 %.
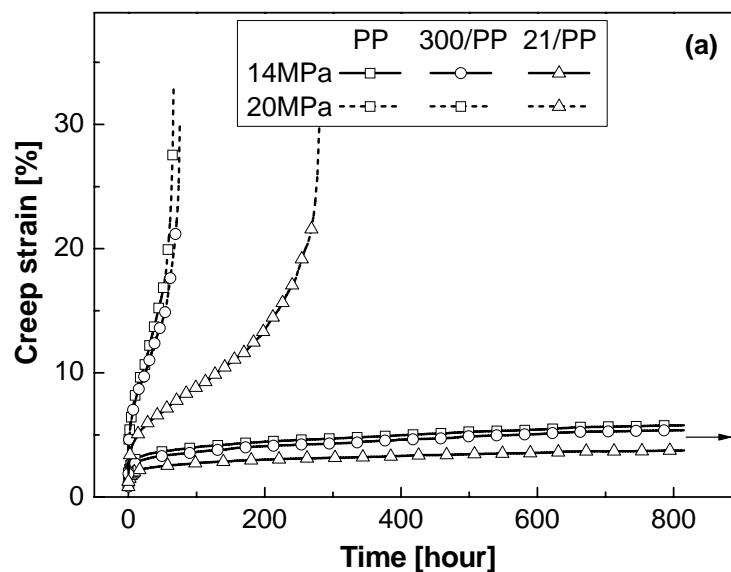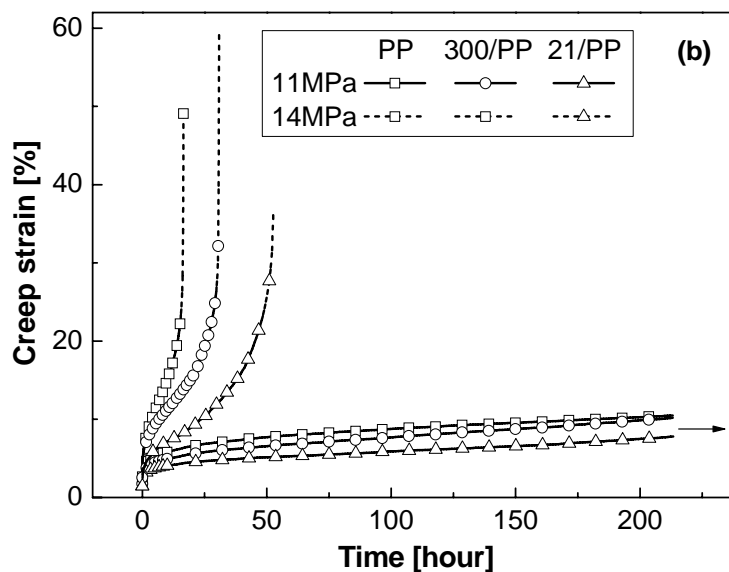
Figure 6.4: The sample curves of creep strain versus time of nanoparticle/PP system at 23 °C **(a)** and 50 °C **(b)** under high and moderate stress levels.

To fully understand the time-dependent deformation and viscoelasticity of the materials under various stress levels and temperatures, the 1-, 10- and 100-hour isochronous stress-strain data are presented in Figures 6.5 and 6.6 at 23 °C and
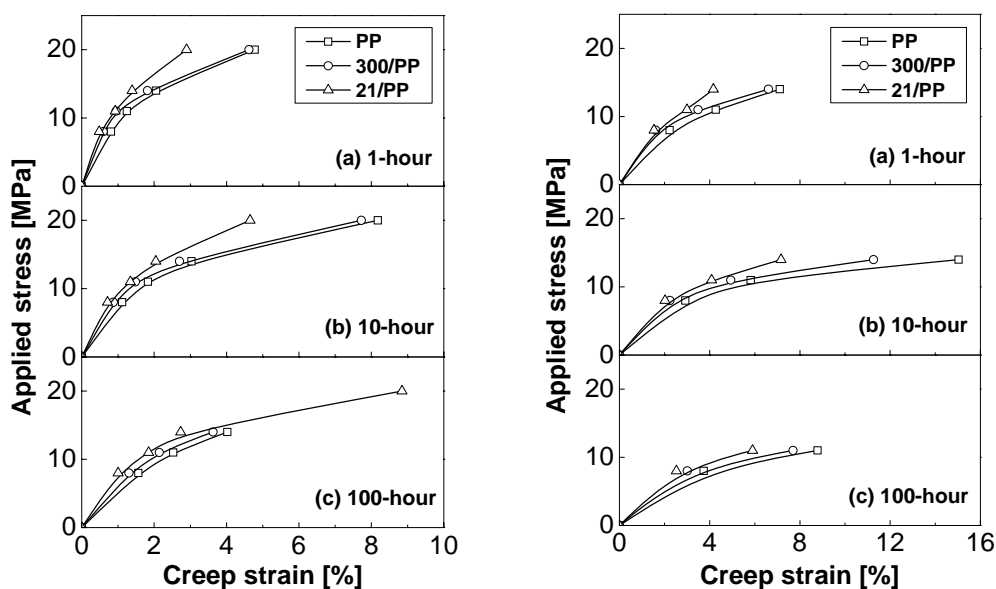
Figure 6.5(left): The isochronous stress-strain curves of nanoparticle/PP material system at 23 °C by 1 hour **(a)**, 10 hours **(b)**, and 100 hours **(c)**.

Figure 6.6(right): The isochronous stress-strain curves of t nanoparticle/PP material system at 50 °C by 1 hour **(a)**, 10 hours **(b)**, and 100 hours **(c)**.

50 °C, respectively. Both at room and elevated temperatures, 21/PP deformed similarly by nearly half the amount of neat PP under each stress level, indicating that the load-induced time-dependent deformation in matrix was notably improved by the application of small nanoparticles. 300/PP showed only a slightly reduced creep strain under each condition in either short- or long-term response, as shown in Figures 6.5 and 6.6. However, obvious enhancement of non-deformability of 300/PP was achieved only at large strain (>10 %), as shown in Figure 6.6(b). In addition, the isochronous curves displayed increased nonlinearity with increasing temperature, indicating that the materials displayed nonlinear viscoelasticity in the observed stress and temperature range, even for the case of small deformation (< 2 %), as shown in Figure 6.5(c). However, the nonlinearity in the composites was no more severe than that in the matrix, demonstrating that the viscous flow and mobility of the polymer chains was restricted to some extent at each stress level due to the presence of nanoparticles.

6.2.2 Creep rate

To study the effect of nanoparticles on creep rate, the sample curves of creep rate versus time are presented in Figure 6.7 at 23 °C (a) and 50 °C (b), corresponding to the creep strain in Figures 6.4 (a) and (b), respectively. Under high stress level, complete creep stages were obtained. In the primary stage creep rate decreased rapidly with time, and after reaching a minimum value in the secondary stage, creep rate increased noticeably with time and an accelerating creep process occurred finally with advanced necking of the material. To compare the creep rate at certain times, creep failure was not considered since there was no tertiary region even for long-term observation for cases of small stress, as shown in Figure 6.7(a).

In the beginning creep stage within 0.1 hour, the creep rate was very similar for all specimens under the same condition. The composites, especially 21/PP, thereafter displayed a greater decrease in creep rate with time under a high stress level.

Additionally, the onset of tertiary creep was obviously deferred to a later time by the loading of small nanoparticles. This retardation led to longer duration of both primary and secondary creep regions, resulting in a lower minimum creep rate and longer
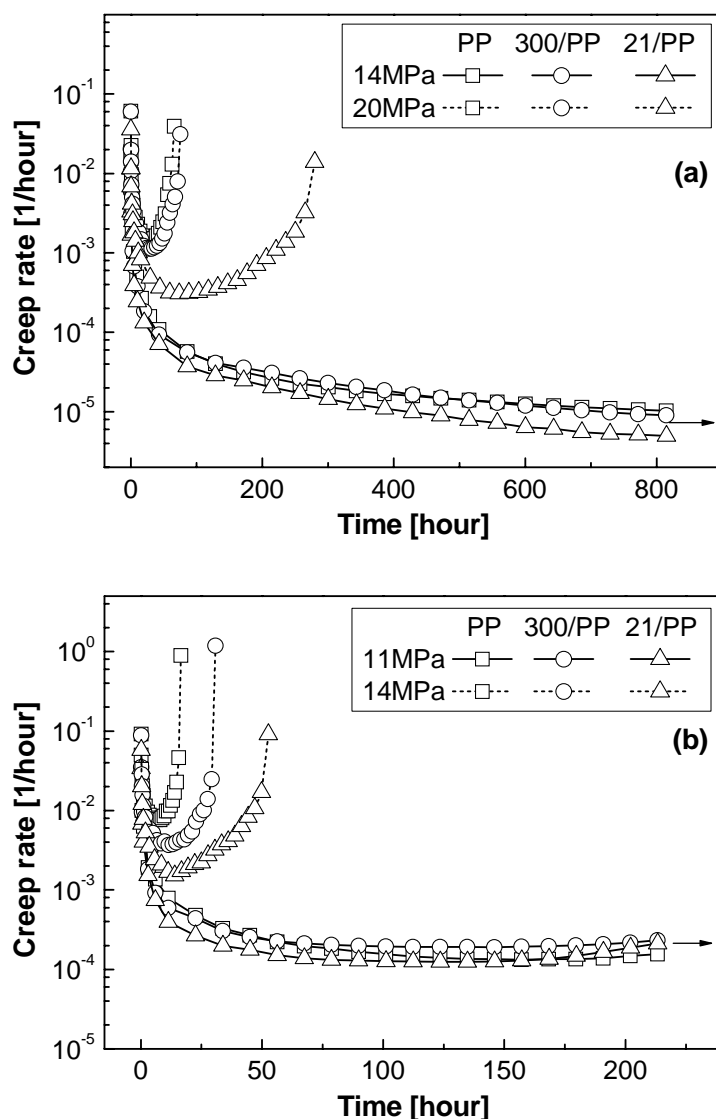
Figure 6.7: The representative curves of creep rate versus time of nanoparticle/PP material system at 23 °C **(a)** and 50 °C **(b)** under different stress levels.

time to failure, as shown in Figure 6.7 by dashed lines connecting symbols. However, under low stress level, the contribution of nanoparticles to reducing the creep rate was less obvious than that under high load level, as shown in Figure 6.7 by solid lines connecting symbols.

The results in Figure 6.7 indicate that stress level and temperature had different effects on creep rate. Figures 6.8 (a) and (b) compare the creep rates under different stress levels at 23 °C and 50 °C, respectively. The minimum creep rate of the materials with a tertiary creep stage and the 200-hour creep rate of the materials

without a tertiary creep stage in the observed time scale are plotted for comparison. The creep rate at the same temperature increased nonlinearly with increasing load, especially at high stress level. The creep rate of each material under the same load obviously increased with increasing temperature. However, the presence of small nanoparticles obviously reduced the creep rate and the reinforcing efficiency was increased with increasing stress level, as shown in Figure 6.8. The larger nanoparticles, however, had only a trivial influence on the resulting creep rate. It is noteworthy to point out that the creep rate of 21/PP decreased similarly by 80 % under both 23°C/20MPa and 50°C/14MPa, compared to that of pure matrix.
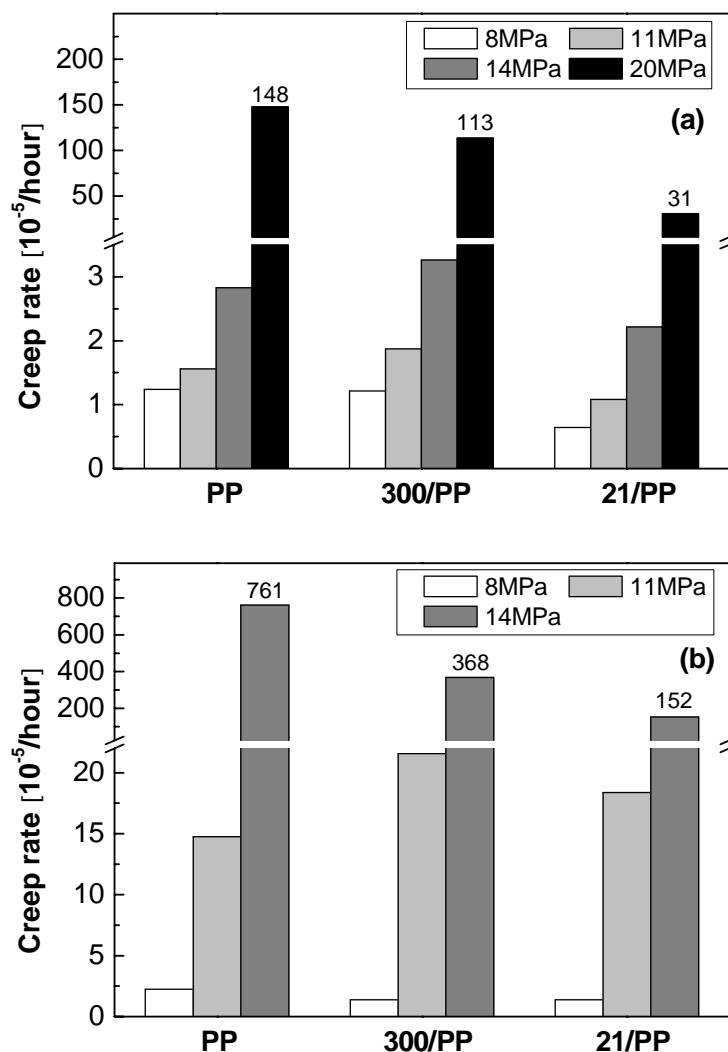
Figure 6.8: Creep rate of nanoparticle/PP system as a function of stress level at 23 °C **(a)** and 50 °C **(b)**.
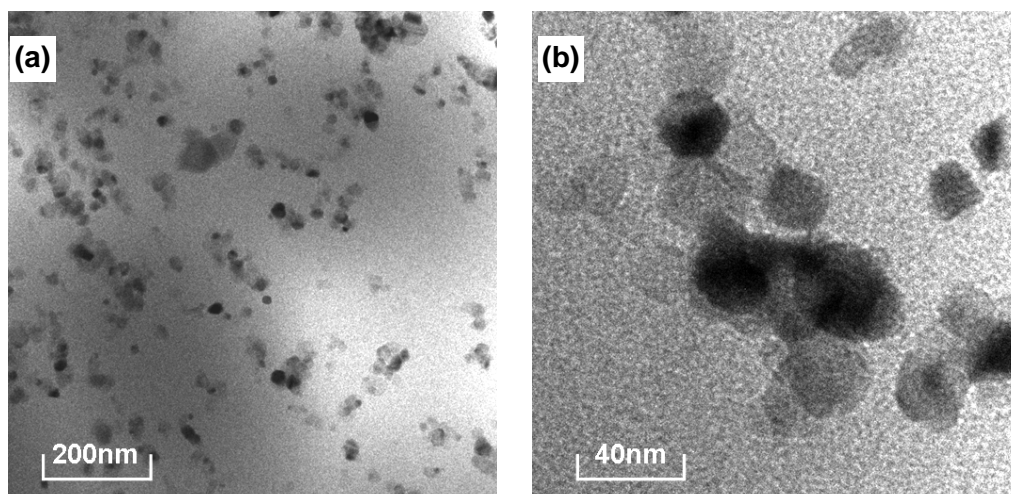
Figure 6.9: TEM micrograph of 21/PP composite. These TEM photographs show fairly good dispersion of nanoparticles in **(a)** and large magnification of some neighboring particles in **(b)**.

To increase understanding of the creep deformation mechanisms of nanoparticles/PP composites, further experiments were performed. The transmission electron microscope (TEM) photographs of 21/PP in Figure 6.9 show a fairly good dispersion of small particles in matrix. The glass transition temperature, T_g, of the nanoparticle/PP system before the creep experiments was also measured, using a dynamic mechanical thermo-analyzer (DMTA). The T_g obtained for particle filled PP
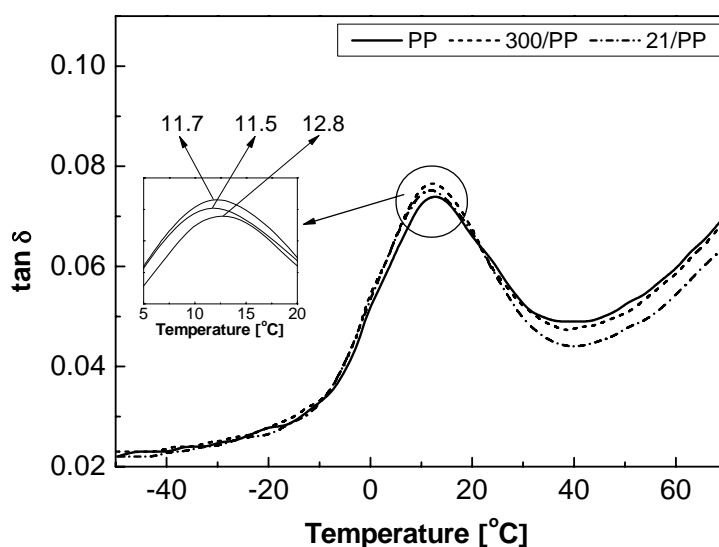
Figure 6.10: DMTA results showing the slight change in T_g of neat PP and particle composites before creep experiment.

(~11.5 °C) was very close to that of neat PP (12.8 °C), as shown in Figure 6.10. This finding indicated that the addition of nanoparticle fillers had no significant effect on the cure chemistry of the matrix. In addition, the spherulitic structure of the nanoparticle/PP system was observed using a polarization optical microscope. The photographs display clearly the existence of micron-sized spherulites in the neat matrix (Figure 6.11(a)), which were significantly destroyed or reduced to sub-micron or nanometric size in composites and could not be discerned in the current magnification, as shown in Figure 6.11(b) and (c). The crystallinity of the specimens before and after creep experiments was measured using a differential scanning calorimeter (DSC), and the results are displayed in Figure 6.12. After creep failure samples for the DSC tests were taken from the advanced necking region. The presence of nanoparticles decreased the crystallinity of the matrix to some extent before creep testing. This change was coincident with the results of altered spherulitic morphology. However, after creep failure under 20MPa/23°C, the crystallinity of 300/PP was increased by 5.3 %,
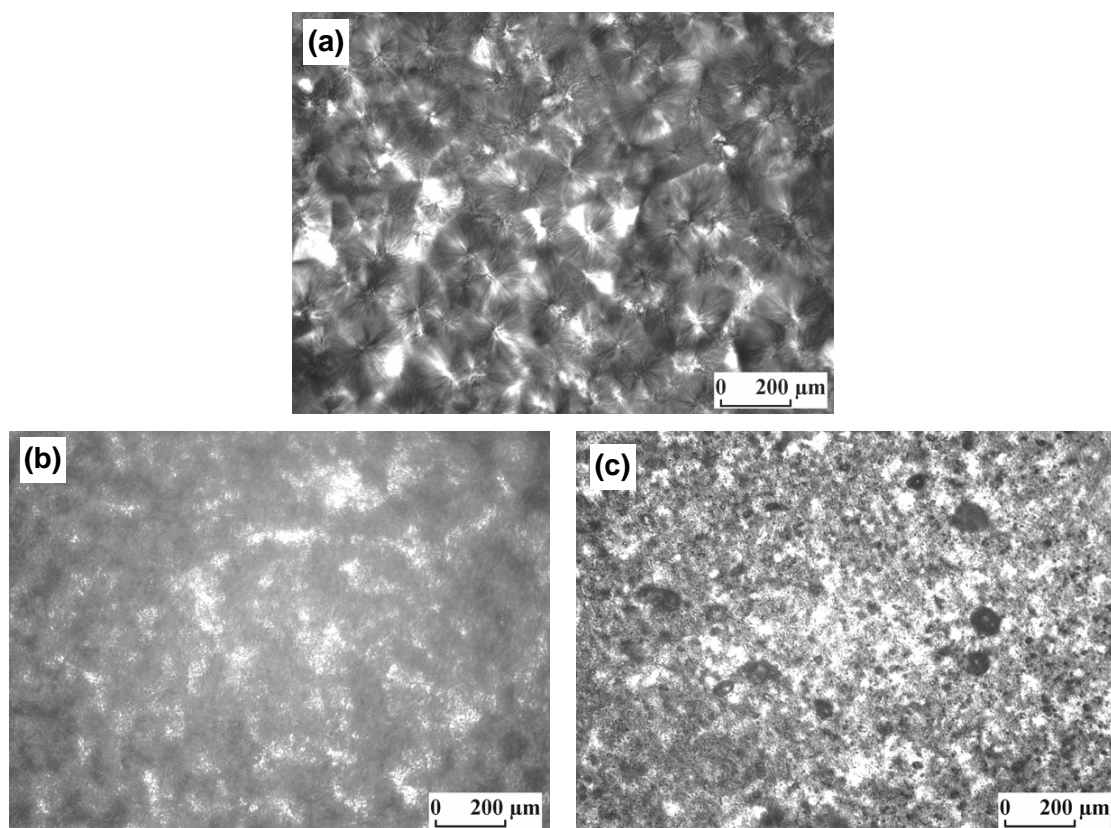
Figure 6.11: Polarization micrographs showing a significant change of spherulite morphology between neat PP **(a)**, 300/PP **(b)**, and 21/PP **(c)**.
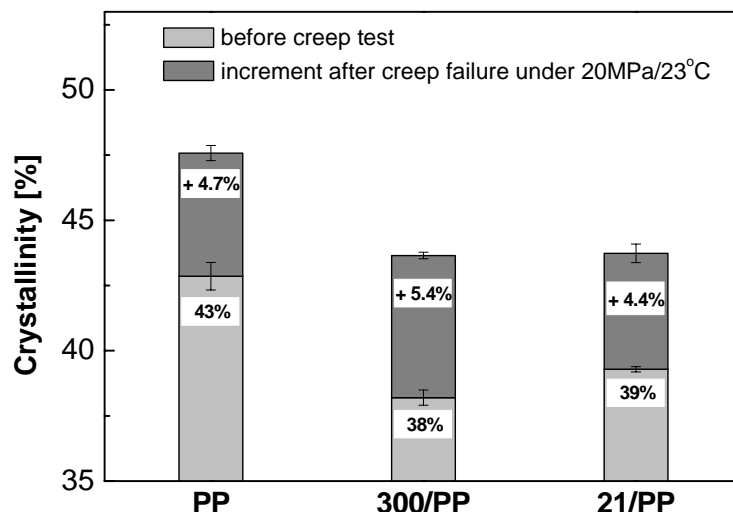
Figure 6.12: DSC results showing the change in crystallinity of neat PP and particle composites before the creep experiment and after creep failure under 20MPa/23°C.

the same as PP, but the increase in value in 21/PP was 3.8 %, a little lower than that of PP and 300/PP.

The structural changes of the specimens after creep tests indicated that small nanoparticles contributed to reducing orientation-induced crystallization while larger ones had no influence at all. These results suggest that small nanoparticles with short interparticle distance (53nm) restricted the mobility of polymer chains [98, 165, 166], whereas large particles with a relatively large interparticle distance (0.75μm) made no contribution to restraining the mobility of polymer chains at this point [83, 86].

6.2.3 Creep compliance

The curves of creep compliance versus creep time of nanoparticle/PP system were obtained under different loads and temperatures, as shown in Figure 6.13 with the same axial scale in logarithmic coordinates. It can be clearly seen from the curves that at RT and 50 °C the creep compliance of each specimen was distinguishable from each other without overlap, implying that nonlinear viscoelasticity of the materials existed within the observed stress range. This is consistent with the results of isochronous stress-strain relationship as discussed earlier. With increase of load

at a constant temperature or with increase of temperature under a constant load, the creep compliance of each specimen also increased and viscous flow became severe, with heightened increase in compliance under very high load levels, as shown in Figure 6.13.

The nanocomposites enhanced creep resistance by reducing compliance compared to PP matrix under the same condition, as illustrated in Figure 6.13. In the case of 300/PP, compliance decreased under relatively low stress levels while there was no obvious change under high loads, i.e. 20MPa/23°C and 14MPa/50°C. However, the compliance of 21/PP was reduced under each load or temperature in comparison with that of 300/PP and neat PP. These results also indicate that the network formed by small particles with short interparticle distance was more effective in retarding and restricting the mobility and motion of polymer chains than that formed by large nanoparticles with greater interparticle distance.

In addition, the non-overlapping creep compliance curves made it possible to apply the time-stress superposition principle by shifting the curves to obtain a master curve at each temperature. This is discussed in a subsequent chapter.
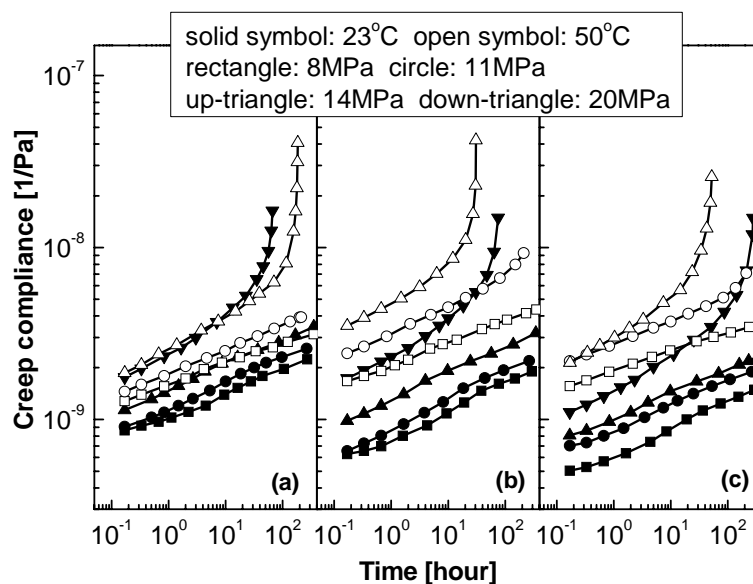
Figure 6.13: Stress and temperature dependence of creep compliance of the tested specimens: **(a)** PP, **(b)** 300/PP, and **(c)** 21/PP.

7   Creep Characterization of MWNT/PP System

7.1   Tensile properties of MWNT/PP system

Tensile experiments were performed at a crosshead speed of 5 mm/min at 23 °C and 50 °C. The Young's modulus, UTS and tensile elongation at necking with relative deviation are shown in Figures 7.1, 7.2, and 7.3, respectively. From Figure 7.1, it can be seen that the modulus of each material decreased significantly with increasing temperature. The Young's moduli of the composites were higher than that of matrix and increased with increasing aspect ratio of tubes, showing the reinforcing effect of nanofillers. L-MWNT/PA displayed the highest modulus at 23 °C and 50 °C, greater by 27 % and 25 %, respectively, than that of PA66.

The UTS of each material decreased greatly with increasing temperature. Large aspect ratio tubes contributed to the UTS by 12 % and 20 % at RT and 50 °C, respectively, while small aspect ratio tubes contributed to the UTS by 10 % and 16 % at RT and 50 °C, respectively. The increases in modulus and UTS of the composites indicated that the external tensile load was successfully transferred to the nanotubes through the CNT/PP interphase [110-114, 126].
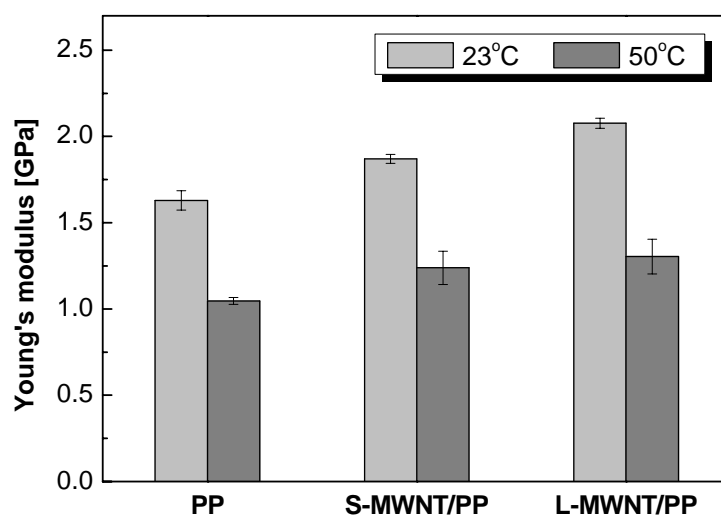
Figure 7.1: Young's modulus of PP and MWNT composites at different temperatures.
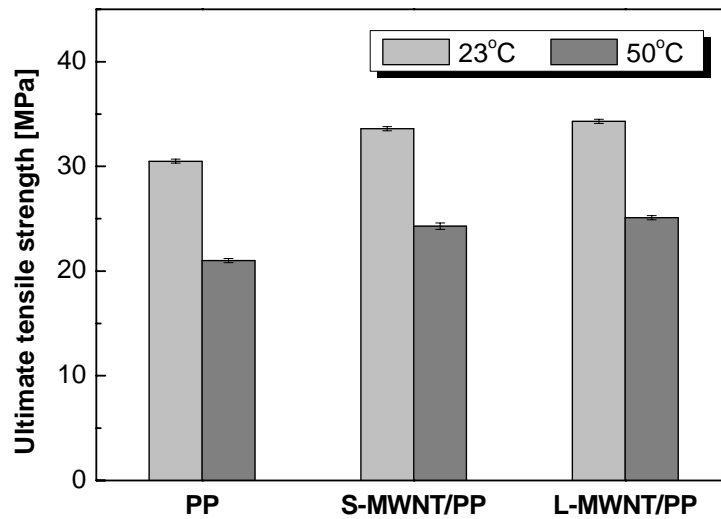
Figure 7.2: Ultimate tensile strength of PP and MWNT composites at different temperatures.
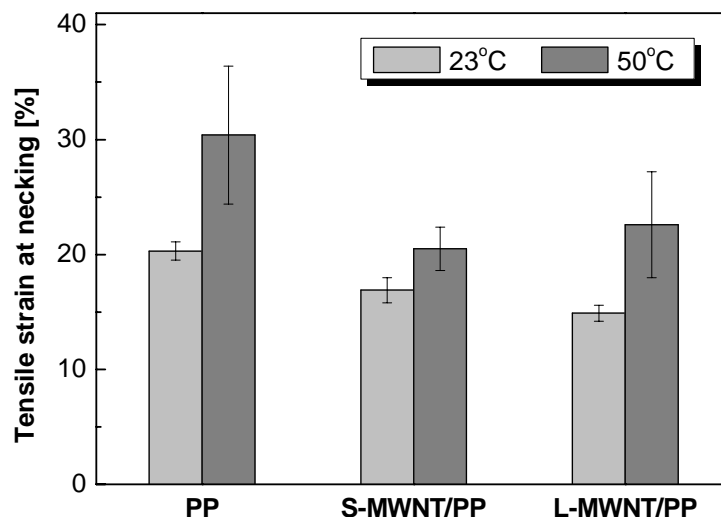
Figure 7.3: Tensile elongation at necking of PP and MWNT composites at different temperatures.

Although the elongation at necking of each material increased with increasing temperature, that value of the nanocomposites was a little lower both at RT and 50 °C than that of neat PP, as illustrated in Figure 7.3.

It could be concluded that the quasi-static tensile properties of the composites were not seriously impaired as a whole by the addition of carbon nanotubes.

7.2 Creep results and general discussion

The multiwalled carbon nanotubes, with high aspect ratio and extremely high modulus, displayed a stronger reinforcing performance than nanoparticles in promoting creep resistance of polymer matrix. The dimensional stability and even the creep lifetime under certain conditions were greatly enhanced. Detailed results and analyses are given below.

7.2.1 Creep deformability and isochronous stress-strain relationship

The partial experimental data for creep strain versus time at 23 °C and 50 °C are graphed in Figures 7.4(a) and (b), respectively, under high and moderate stress levels. The arrows indicate that the specimens were not in failure under moderate stress level within the time scope of observation. It can be seen that the composites showed greatly enhanced creep resistance with similar creep deformation. An extraordinary phenomenon was observed, that the creep lifetime of the composites was extended by about 800 % (9-fold) and 1000 % (11-fold) compared to that of pure matrix under 23°C/20MPa and 50°C/14MPa, respectively, as shown in Figure 7.4 by the dashed line. Additionally, the large aspect ratio CNTs displayed a slightly better reinforcing effect than small ones at 23 °C, while tending towards the same performance at elevated temperature.

To quantify the time-dependent deformation and the viscoelasticity of the materials under various stress levels and temperatures, the 1-, 10- and 100-hour isochronous stress-strain data are presented in Figures 7.5 and 7.6 at 23 °C and 50 °C, respectively. Both at room and elevated temperatures, the composites deformed similarly at nearly half the degree of neat PP under each stress level, indicating that the load-induced time-dependent deformation of the matrix was notably improved by the application of multiwalled carbon nanotubes. In addition, the isochronous curves displayed increased nonlinearity with increasing temperature, indicating that the materials behaved nonlinear viscoelasticity within the observed stress and temperature range, even for the case of small deformation (< 2 %), as shown in Figure 7.5(c). However, the nonlinearity in the composites was not as severe as that in the matrix, demonstrating that the viscous flow and mobility of the polymer chains
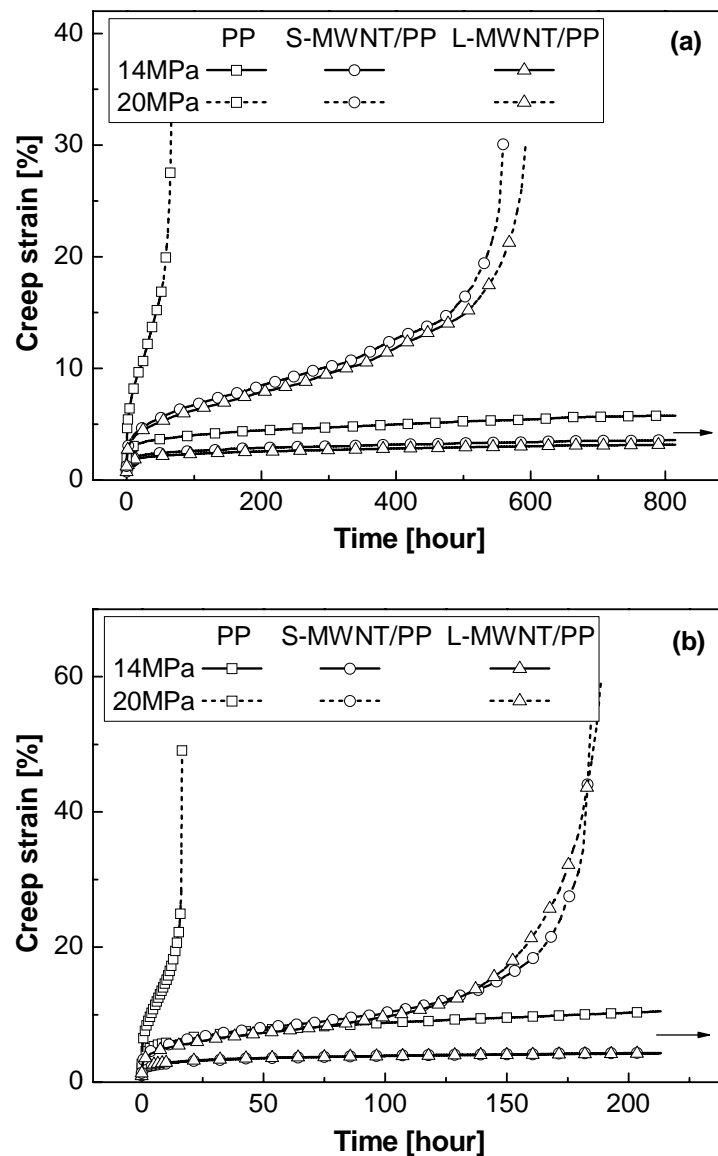
Figure 7.4: The sample curves of creep strain versus time at 23 °C **(a)** and 50 °C **(b)** under high and moderate stress levels.

were greatly restricted through the effective load transfer due to the presence of MWNTs under each stress level.

7.2.2 Creep rate

To illustrate the effect of the nanotube fillers on creep rate, the sample curves of creep rate versus time are presented in Figure 7.7 at 23 °C (a) and 50 °C (b), corresponding to the creep strain in Figures 7.4 (a) and (b), respectively. The complete creep rate curves consisted of the primary creep region, where the creep
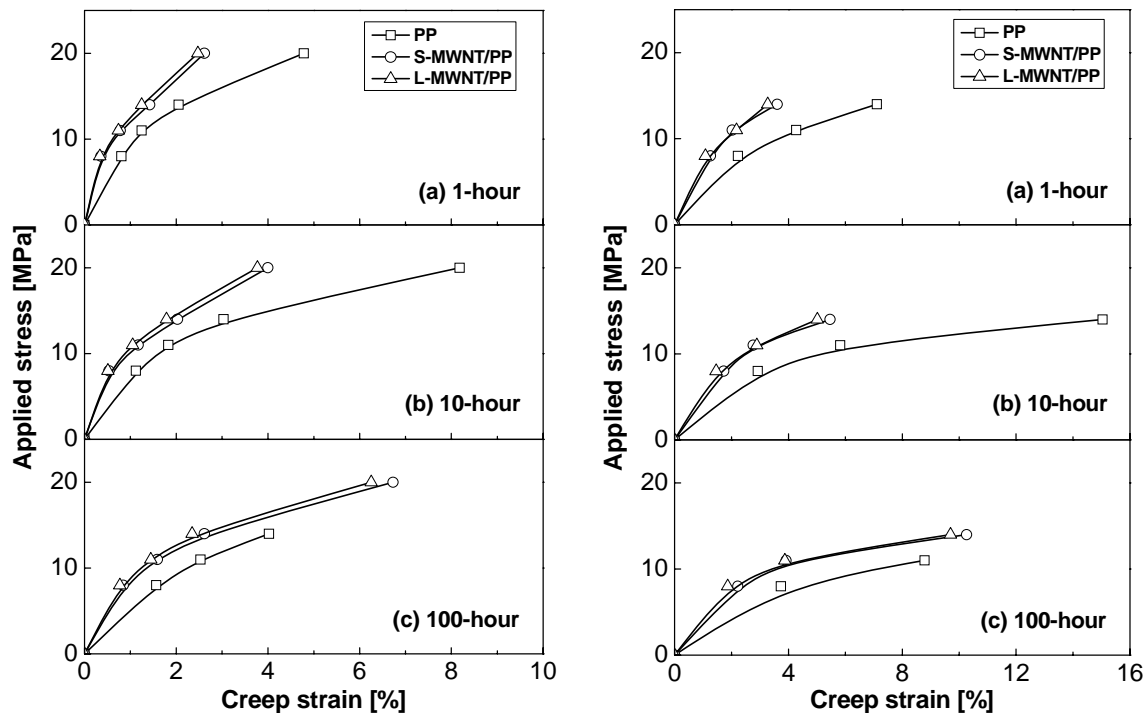
Figure 7.5(left): The isochronous stress-strain curves of the tested materials at 23 °C by 1 hour **(a)**, 10 hours **(b)**, and 100 hours **(c)**.

Figure 7.6(right): The isochronous stress-strain curves of the tested materials at 50 °C by 1 hour **(a)**, 10 hours **(b)**, and 100 hours **(c)**.

rate decreased with time, and the tertiary creep region, where the creep rate increased with time after reaching a minimum value and an accelerating creep process occurred finally with advanced necking of material. The secondary creep region was very short at high stress level compared to that of the composites. To compare the creep rate at certain time, creep rupture was not necessary since for the small stress cases there was no tertiary region even after a sufficiently long time of observation (cf. creep curves under 14 MPa in Figure 7.4(a)).

During the beginning creep stage within 0.1 hour, the creep rate was nearly the same for all specimens under the same condition. The composites thereafter displayed a greater decrease in creep rate with time. Additionally, the onset of tertiary creep was deferred for a longer time by the loading of nanotubes. This retardation led to a longer duration of both primary and secondary creep regions, resulting in a lower minimum creep rate and longer time to failure, as shown in Figure 7.7.
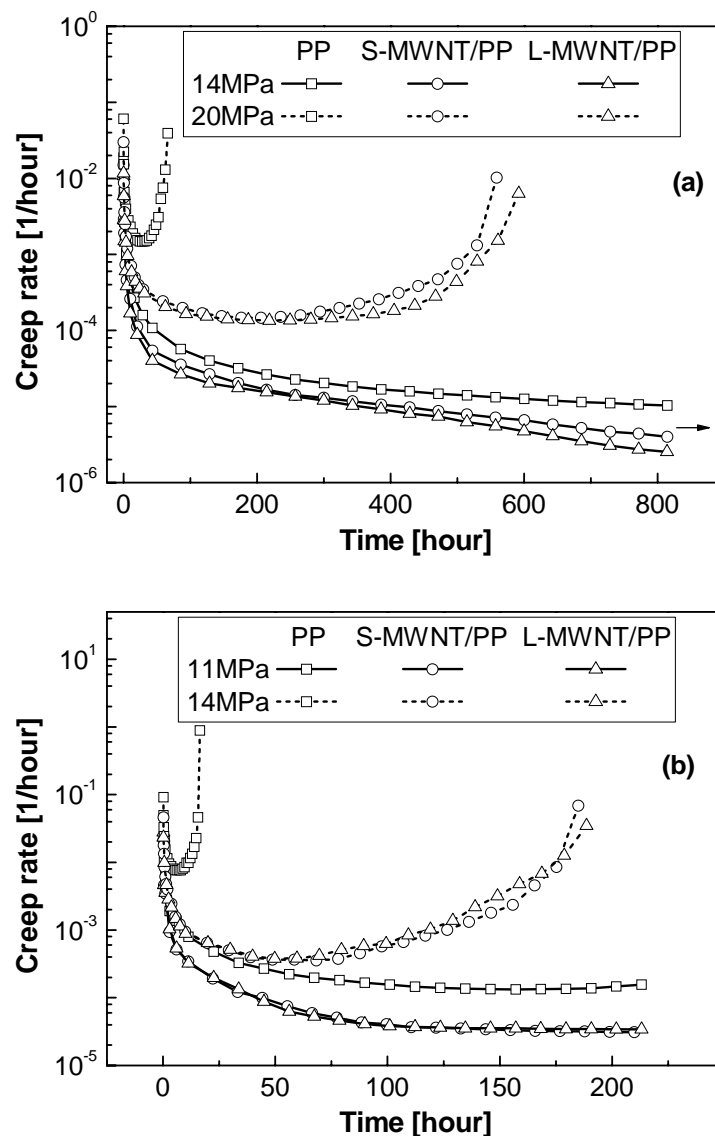
Figure 7.7: The sample curves of creep rate versus time at 23 °C **(a)** and 50 °C **(b)** under different stress levels.

It can also be seen that stress level and temperature had different effects on creep rate. Figures 7.8 (a) and (b) compare creep rates at different stress levels at 23 °C and 50 °C, respectively. The minimum creep rate of the materials with a tertiary creep stage and the 200-hour creep rate of the materials without a tertiary creep stage in the observed time scale are plotted for comparison. The creep rate at the same temperature increased nonlinearly with increasing load, especially at high stress level. The creep rate of each material under the same load increased obviously with increasing temperature. However, the presence of nanotubes greatly reduced the creep rate, and the reinforcing efficiency was increased with increasing
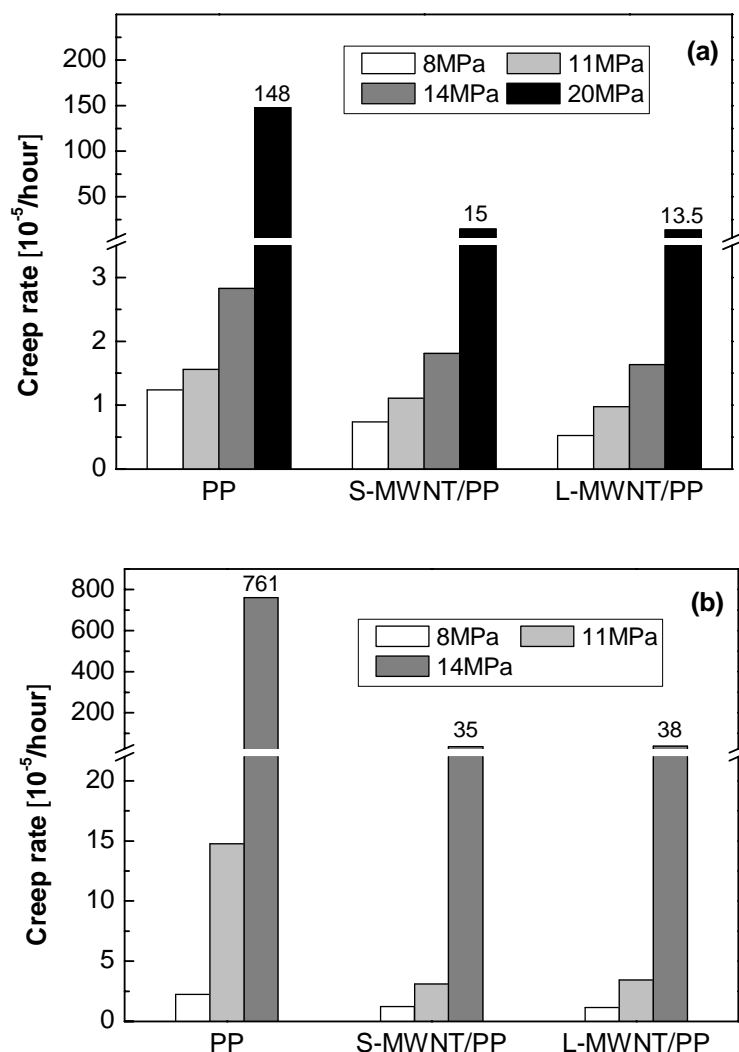
Figure 7.8: Creep rate as a function of time at 23 °C **(a)** and 50 °C **(b)** under different stress levels.

stress level, as shown in Figure 7.8. The aspect ratio of nanotubes in the observed range had a negligible influence on the resulting creep rate. It is noteworthy to point out that the creep rate of the nanocomposites was decreased considerably compared to that of baseline matrix, by 91 % and 95 % at 23°C/20MPa and at 50°C/14MPa, respectively.

To understand the creep deformation mechanisms of nanotubes/ polymer composites, further experiments were also performed. The glass transition temperature, T_g, of the pure and MWNT filled system before and after creep experiments was also measured using a dynamic mechanical thermo-analyzer
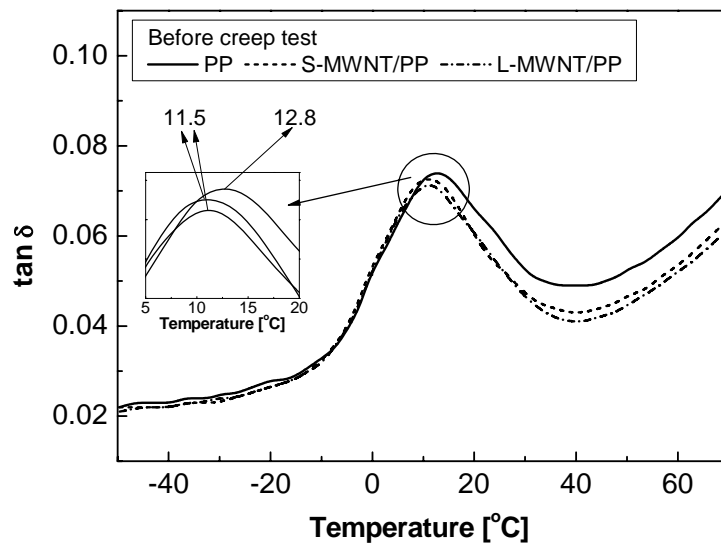
Figure 7.9: DMTA results showing the change of T_g of neat PP and MWNT composites before creep experiments.

(DMTA). The obtained T_g of the MWNT filled PP (11.5 °C) was very close to that of neat PP (12.8 °C), as shown in Figure 7.9. This finding indicates that the addition of nanotube fillers had no significant effect on its cure chemistry. The slight decrease in T_g might be a result of intertube sliding or stick-slip [107, 171]. In addition, the crystallinity of the specimens before and after creep experiments was measured using a differential scanning calorimeter (DSC), and the results are displayed in Figure 7.10. The samples for DSC were cut from the advanced necking regions in the specimens after creep failure under 20MPa/23°C. Crystallinity decreased only slightly, by about 1 %, after the addition of nanotubes. However, after creep failure crystallinity increased by 4.7 % in PP and by 3.5 % and 1.8 % in S-MWNT/PP and L-MWNT/PP, respectively, on each basic value before experiment.

The different crystallinity changes in the specimens after creep tests indicate that carbon nanotubes participated to reduce orientation crystallization, suggesting that a load transfer effect occurred successfully and the mobility of polymer chains was thus effectively constrained. Two possible mechanisms of load transfer could have contributed to the observed enhancement in creep resistance: (1) fairly good interfacial strength between MWNTs and polymer matrix, and (2) high aspect ratio of multiwalled carbon nanotubes. As mentioned above, the tensile properties, except
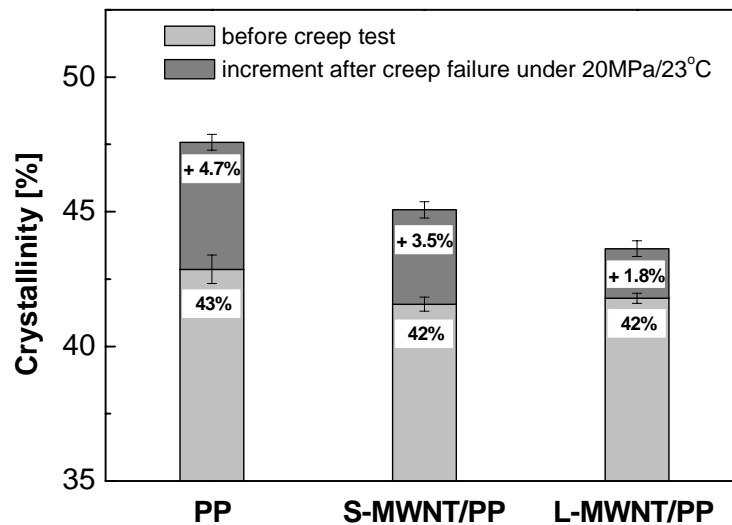
Figure 7.10: DSC results showing the change in crystallinity of neat PP and MWNT composites before and after creep experiments.

for the reduced ductibility, the Young's modulus and tensile strength of the composites increased to some extent. The tensile results were consistent with those reported in references [110-114], indicating that the external tensile loads were successfully transmitted to the nanotubes through the CNT/PP interface. Additionally, under low tensile stress any decrease in creep rate of composites might be negated by the occurrence of intertube sliding or stick-slip [107, 171], which is consistent with the observation of T_g. However, under high tensile stress level the large deformation of specimens could introduce high interfacial shear stress to the nanotubes across the interface. Most tubes in the matrix would slip extensively in a short time period, resulting in a relatively high creep rate (Figures 7.7 and 7.8). The negative influence of intertube sliding was thereafter minor due to the extensively stretched polymer chains. The outmost nanotubes bonded to the matrix were then transferred to sustain most external tensile load. A significant reduction in creep rate and deformation was then achieved. The load-bearing capability was enhanced and the secondary creep stage was prolonged under high stress level.

To understand the importance of the filler aspect ratio mechanism, it is necessary to compare earlier results of traditional carbon fibre reinforced polymers. Qian et al. [111] compared their tensile results of MWNT (l/d=450)/polystyrene (PS) with those of vapor-grown carbon fibre (VGCF, l/d=18)/PP and a commercial high-modulus

carbon fibre (E-75, *l/d*=44)/PS composite. The filler content was the same, at 0.5 vol. %. The experimental moduli of MWNT/PS, VGFC/PP and E-75/PS were close to the corresponding calculated values [111]. The nanocomposite was superior to the fibre-composites under the same filler loadings, a finding which was attributed to their large aspect ratio. In view of those results, it seems reasonable to believe that the aspect ratio of the MWNTs in the composites investigated in the present study played an important role in transferring load and thus enhancing creep resistance. It should be mentioned that the similar performance of S- and L-MWNT/PP nanocomposites might result from two aspects in the material processing. In the melt extrusion, longer tubes were more easily shortened and entangled than shorter ones due to the existence of thermal and torsional actions. These deleterious effects were responsible for the poorer results of L-MWNT/PP. In addition, there was a high orientation-induced crystallinity in neat PP. Large aspect ratio nanotubes could reduce this orientation-induced crystallinity slightly more effectively than small aspect ratio ones, as shown in Figure 7.10. This finding revealed that nanotubes hindered the orientation movement of polymer chains and the effectiveness of large aspect ratio nanotubes was greater than that of small aspect ratio ones at high load levels. Other minor stress transfer mechanisms were possible as well, namely that stress
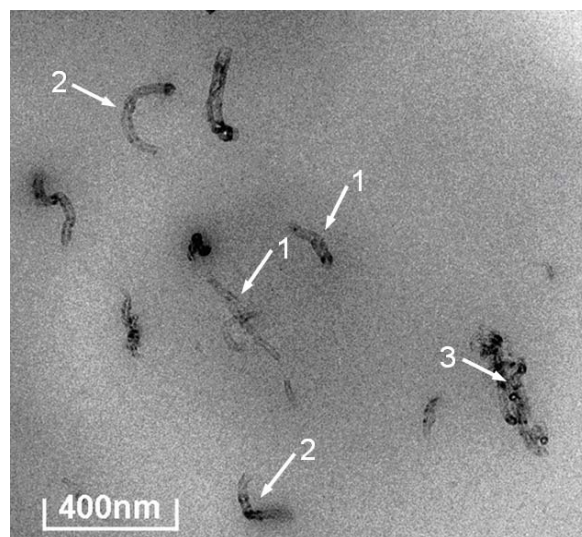
Figure 7.11: TEM micrograph of S-MWNT/PP composite. This TEM photograph shows a fairly good dispersion of nanotubes displaying different forms caused by thermal and torsional action during the melt extruding process. Arrow 1, straight tubes; arrow 2, curved tubes; arrow 3, entangled tubes.

was also transferred in tension through the nanotube ends [172] and curved and entangled nanotubes, as shown in the TEM image in Figure 7.11. The curved and entangled tubes were formed due to thermal and torsional action during melt mixing in an extruder. The efficiency of this type of load transfer mechanism was obviously lower than that of shear force transfer along the loading direction. However, the precise effect is difficult to evaluate at this point. The effects of other parameters, including wall thickness and tube diameter, on interfacial strength and load transfer efficiency remain to be studied.

7.2.3 Creep compliance

The curves of creep compliance versus creep time of MWNT/PP system were obtained under different loads and temperatures, as shown in Figure 7.12 with the same axial scale in logarithmic coordinates. It is evident from the curves that at room temperature and 50 °C the creep compliance curves of each specimen were distinct from each other without overlap, suggesting that the materials exhibited nonlinear viscoelasticity under the observed stress range. This was accordant with the results of isochronous stress-strain relationship as discussed above. With increase in load at constant temperature or with increase in temperature under constant load, the
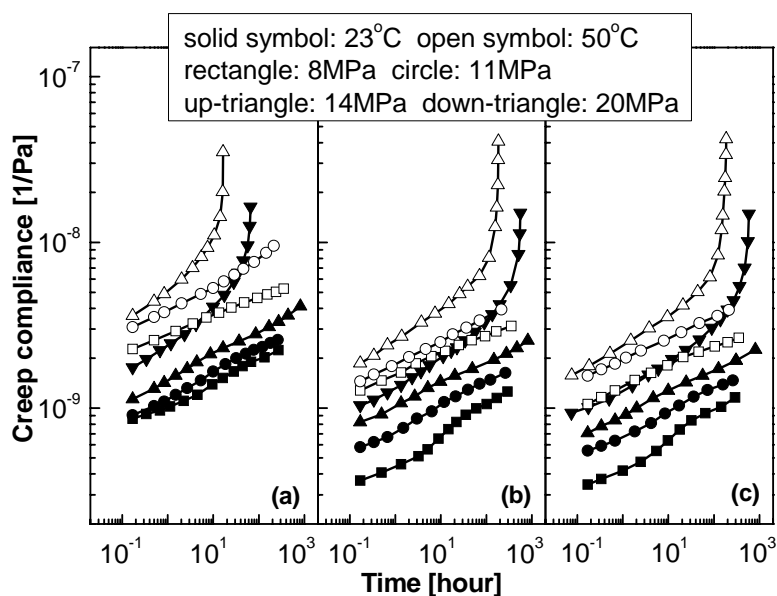
Figure 7.12: Stress and temperature dependence of creep compliance of tested specimens: (a) PP, (b) S-MWNT/PP, and (c) L-MWNT/PP.

creep compliance of each specimen also increased obviously and viscous flow became severe with advanced increase in compliance at very high load levels, as shown in Figure 7.12.

Nanocomposites showed enhanced creep resistance by significantly reducing compliance compared to PP matrix under each condition, and the long nanotubes exhibited an advantage over short ones at this point, as displayed in Figure 7.12. These improved results also implied that the carbon nanotubes played a key role in the load transfer effect.

In addition, the non-overlapping creep compliance curves made it possible to apply the time-stress superposition principle by shifting the curves to overlap with the reference one to obtain a master curve at each temperature. This is discussed in a subsequent chapter.

8 Creep Modeling Analysis and Prediction of Long-term Behaviors of Polymer-based Nanocomposites

8.1 Creep modeling analysis

8.1.1 Nanoparticle/PA system

Simulated curves using the Burgers model and Findley power law were drawn with solid lines and dashed lines, respectively, with the experimental creep strain at 50 °C, as presented in Figure 8.1. It can be seen that both modeling curves show satisfactory agreement with the experimental data under each condition. Detailed discussion based on the modeling parameters is presented in the following subsections.
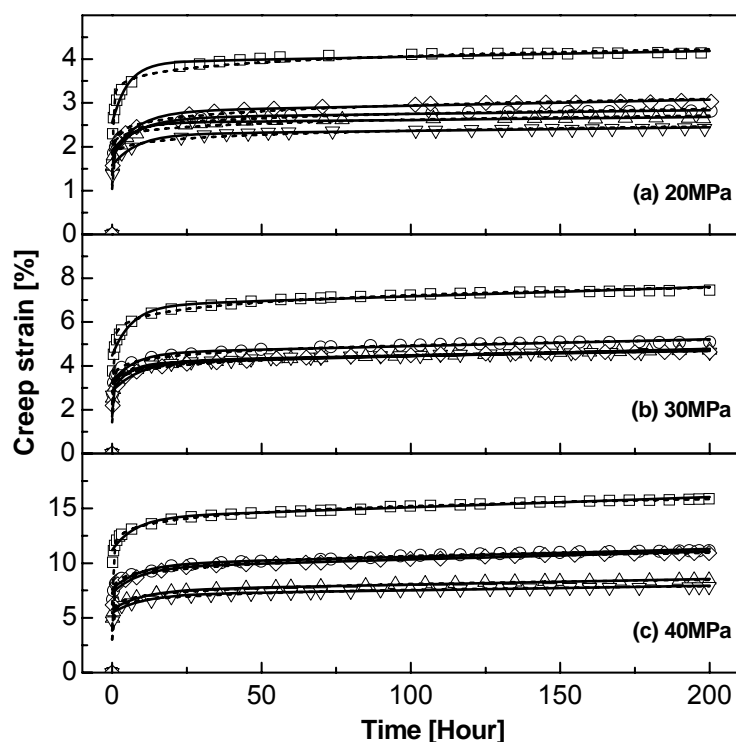
Figure 8.1: Modeling results of partial curves of creep strain versus creep time obtained at 50 °C and (a) 20 MPa, (b) 30 MPa, and (c) 40 MPa. Experimental data: PA (□), 300/PA (O), 21-SM/PA (△), 21/PA (▽), Clay/ PA (◇). Modeling curves: Burgers model (——) and Findley power law (------).

8.1.1.1 Burgers model

The complete modeling parameters of the tested samples are listed in Table 8.1. Discussion based on these parameters is presented below.

I.   Time independent elasticity E_M

According to the constitutive Equation (4.10), the modulus E_M of the Maxwell spring determins the instantaneous elastic creep strain, which can be immediately recovered upon removal of stress. In general, the composites displayed higher values of E_M than neat matrix under each condition. Among the composites 21/PA had the highest elasticity, 21-SM/PA was next in the hierarchy, and 300/PA and Clay/PA were both close, indicating that smaller nanoparticles without surface modification were much more effective in reinforcing the elasticity of polymer matrix, and that nanoclay layers, although with a different structure from nanoparticles, effected a similar reinforcement to large nanoparticles in elasticity, as shown in Table 8.1. However, the variations in E_M of the tested materials showed different dependence on the various loads and temperatures.

The E_M of each specimen showed a decreasing function with temperature, which was easily understood in that the bulk materials became soft at elevated temperatures and the stiffness thus decreased with diminished instantaneous modulus. However, stress dependent E_M was much more complicated. To assist in understanding the relationship between the parameterized model and the real structure of the materials, a representative configuration of the nanofiller/polymer composites (cf. Figure 5.9) is again referred to here. The essential parts, including crystallized chains, amorphous and entanglement regions, segment and crystalline bridging between fillers, polymer-filler junction, and intercrystalline tie molecules, exhibited different responses under various stresses and temperatures.

At 23 °C, E_M was non-sensitive to the load within the observed range except for PA under 40 MPa, where an obvious drop in E_M occurred due to the poor load bearing ability. This performance was consistent with the fact that the short time response at room temperature, as determined for example from the one-hour isochronous

Table 8.1: The simulated parameters of the Burgers model and the activation volume υ at higher stress levels.

T	Sample	σ_0 (MPa)	$E_{tensile}$ (MPa)	E_K (MPa)	E_K (MPa)	η_M (GPa·hr)	η_K (GPa·hr)	τ (hour)	υ (nm³)
23°C	PA66	20	2280	3709	16617	889	236	14.2	
		30		3653	8673	991	113	13.1	
		40		2490	1616	404	23.7	14.7	0.590
	300/PA	20	2650	1909	16665	1270	253	15.2	
		30		2536	6580	1311	102	15.5	0.474
		40		2647	2646	681	38.1	14.4	(-20%)
	21-SM/PA	20	2270	3509	19642	2394	315	16	
		30		3204	8514	1928	185	21.7	0.425
		40		3442	3584	896	60	16.8	(-28%)
	21/PA	20	2760	4348	22815	1819	272	11.9	
		30		4267	8713	1841	183	20.9	0.361
		40		3708	4652	1033	91.7	19.7	(-39%)
	Clay/PA	20	2770	3344	24411	1330	406	16.6	
		30		4418	7371	1301	105	14.3	0.536
		40		3130	3900	696	78.1	20	(-9.2%)
50°C	PA66	20	1470	784	1458	1487	76.4	5.24	
		30		671	1317	706	85.6	6.5	
		40		357	1348	429	10.4	7.7	0.418
	300/PA	20	1690	1039	2718	2248	25.3	9.3	
		30		918	2269	956	16.6	7.31	0.426
		40		525	1773	570	16	9.04	(+1.9%)
	21-SM/PA	20	2020	1163	2421	2963	13.6	5.6	
		30		1068	2295	906	11.4	4.98	0.234
		40		692	2302	774	23.4	10.2	(-44%)
	21/PA	20	1820	1274	2809	2446	22.8	8.13	
		30		991	2567	1169	16.3	6.35	0.279
		40		732	2418	988	24.9	10.3	(-33%)
	Clay/PA	20	1810	1087	2083	1455	17.2	8.28	
		30		1059	2242	1043	19.8	8.85	0.467
		40		551	1712	544	15.2	8.88	(+12%)
80°C	PA66	20	860	400	1835	1675	7.34	4	
		30		284	1336	818	6.77	5.1	
		40		156	232	207	0.75	3.2	0.818
	300/PA	20	1030	584	2714	3239	14.9	5.5	
		30		412	2120	1772	11.06	5.22	1.147
		40		181	586	322	5.65	9.65	(+40%)
	21-SM/PA	20	980	680	2599	2146	9.85	3.79	
		30		470	2262	2179	9.55	4.22	0.956
		40		290	1128	573	12.3	10.9	(+17%)
	21/PA	20	1060	707	2987	3652	19	6.37	
		30		465	2360	1976	14.3	6.08	0.371
		40		289	1428	793	14.2	9.97	(-55%)
	Clay/PA	20	1050	602	1841	1997	6.17	3.35	
		30		407	1753	1239	9.32	5.32	0.983
		40		190	619	319	7.47	12.1	(+20%)

$E_{tensile}$ is the Young's modulus obtained from the quasi-static tensile experiments. The activation volume υ was calculated under high stress levels (30-40 MPa) with relative change of composites compared to the value of neat matrix.

modulus, was linear, i.e. strain proportional to stress, which was conformably shown in Figure 5.6(a) in the earlier section. In addition, the linear range of stress was broadened by the addition of nanofillers. Among the tested materials, E_M showed comparatively small changes in neat matrix PA66, 21-SM/PA and Clay/PA. The increment of E_M in 21/PA and the decrement of E_M in 300/PA were both small. This demonstrated that instantaneous elasticity was not greatly altered by the addition of nanofillers. The instantaneous elasticity E_M corresponded reasonably well to the elasticity of the crystallized polymer or regular chain folds which bore the immediate load due to high stiffness, compared to amorphous polymers, as illustrated in Figure 5.9. However, although the crystalline morphology was changed by the addition of nanofillers (cf. Figure 5.10), the crystallinity of each specimen was not obviously altered, as shown in Table 8.2, which implies that the load bearing parts were not greatly different between neat matrix and nanocomposites.

At 50 °C, E_M of each specimen decreased with increasing stress levels, with similar values under 20 MPa and 30 MPa and significantly diminished values under 40 MPa. It is reasonable to believe that a threshold of linear viscoelasticity existed around the stress of 30 MPa for the short-term response, which was also consistent with the one-hour isochronous stress-strain relationship in Figure 5.6(b). Among the observed specimens, the nanocomposites displayed much better elasticity than the pure matrix, showing the effectiveness of reinforcement by the addition of nanofillers near the glass transition temperature. E_M increased with decreasing particle size under each stress level, while the value of 21-SM/PA was very close to that of 21/PA, demonstrating that at 50 °C, nanoparticles with surface modification made no

Table 8.2: The crystallinity and glass transition temperature of the specimens measured using a differential scanning calorimeter.

Sample	Crystallinity	T_g [°C]	
		Onset	Middle
PA66	38.67 %	45.67	52.13
300/PA	37.51 %	50.72	56.83
21-SM/PA	37.24 %	46.15	51.58
21/PA	34.36 %	46.47	54.79
Clay/PA	36.53 %	48.82	55.24

obvious contribution to the elasticity of the bulk material compared to non-surface modified particles. E_M of Clay/PA was slightly higher than that of 300/PA, showing that the reinforcing effectiveness of nanoclay layers was of a similar level to that of large nanoparticles. Near the glass transition temperature polymer chains became active. Consequently the stiffness of bulk material decreased, resulting in a low value of E_M compared to that at RT. Reasoning from the dependency of E_M on stress, it might be considered that the elastic limit of each tested material was slightly higher than 30 MPa, below which a minute change in E_M occurred, while a large fall-off occurred under 40 MPa. As described in Chapter 5, the amount of small particles in unit volume matrix was higher than that of large particles by several orders of magnitude. A much denser network could be formed with small particles compared to large ones, although there were agglomerates. This three dimensional network, together with the crystallized polymer chains, could markedly enhance the capability to bear load at elevated temperatures. In the case of Clay/PA, the nanoclay layers could bear load due to the large aspect ratio of individual platelet but this capacity was negated by the large amount of non-exfoliated layers. Hence the resulting E_M of Clay/PA was very close to that of 300/PA.

At a temperature above T_g, i.e. 80 °C, the E_M of each specimen clearly decreased with increasing stress, showing non-elastic deformation in the short-term response due to the easy viscous flow of the bulk materials. The nanocomposites possessed high elasticity under each stress level, indicating that the nanofillers were enhanced the elasticity of the polymer matrix even at elevated temperatures. 21-SM/PA and 300/PA displayed elasticity very close to that of 21/PA and Clay/PA, respectively. This similar performance again illustrated that at elevated temperature surface modification made no apparent contribution to the elasticity of bulk materials. Because of the enhanced mobility of amorphous chains and even chain folds at very high temperature, the stiffness of the bulk materials decreased significantly with very low E_M. The limit of elasticity of each material was somewhat below 20 MPa since E_M was clearly dependent on the stress observed from 20 MPa to 40 MPa. The network of small particles was much more effective in enhancing elasticity than that of large ones and clay layers. For the same reasons as at 50 °C mentioned above, 300/PA and Clay/PA exhibited similar E_M but with lower value.

II. Retardant elasticity E_K and viscosity η_K

The retardant elasticity E_K and viscosity η_K of each specimen showed a similar dependency on temperature, decreasing with increasing temperature. It could be alternatively stated that the deformation of the Kelvin unit of each material increased with increasing temperature. However, the stress dependent E_K showed a considerably different scenario from the instantaneous elasticity E_K. The time dependent E_K and η_K in the Kelvin unit might be associated with the stiffness and viscous or orientated flow of amorphous polymer chains, respectively.

At room temperature, E_K and η_K decreased considerably with increasing load, showing high stress dependency. This finding indicated that the materials with relatively high bulk modulus deformed very little under low stress, showing that the Kelvin unit displayed extremely high modulus and highly viscous flow. With increasing stress, the orientation movement of amorphous chains including elastic deformation and viscous flow became exaggerated, resulting in reduced E_K and η_K. The consistent change of E_K and η_K with stress led to a nearly constant retardant time τ for each specimen, as listed in Table 8.1.

With temperature in the T_g range, amorphous segments became much more active and were promptly oriented in the short term once the stress was loaded. The polymer chains thereafter lay in a high potential energy site due to orientational hardening [161, 168]. However, the Kelvin unit could not be activated to reorientate in advance in the observed time span, i.e., 200 hours, because of relatively low stress resulting in nearly constant E_K and η_K of each specimen except for PA66 under 40 MPa, where an obvious viscous flow occurred. The retardant time τ also remained constant.

Since the mobility of amorphous polymer at 80 °C was much greater, the reorientation of amorphous polymer chains was markedly different from the case at T_g. According to the parameters obtained under various stress levels, a threshold stress existed near 30 MPa, below which the reorientation of amorphous polymer could not be activated with nearly constant E_K, η_K, and τ, but above which the Kelvin

elements were activated with advanced reorientation including significant plastic deformation and viscous flow of amorphous chains and reduced retardant time τ.

It should be pointed out that all nanofillers showed a positive effect on the Kelvin unit. Among the observed fillers, small-sized particles with a tridimensional network in matrix were the most effective in retarding the deformation of the Kelvin elements. Generally 21-SM/PA was slightly weaker because of the deterioration in interfacial strength caused by the modified surfaces of particles. 300/PA and Clay/PA displayed similar performance.

III. Permanent viscous flow η_M

On the basis of the discussion of the instantaneous and time-dependent recoverable components, which showed enhancement to some extent by the presence of nanofillers, we now provide an analysis of a more important parameter η_M, which represented irrecoverable creep and was a factor several to ten times higher than η_K,
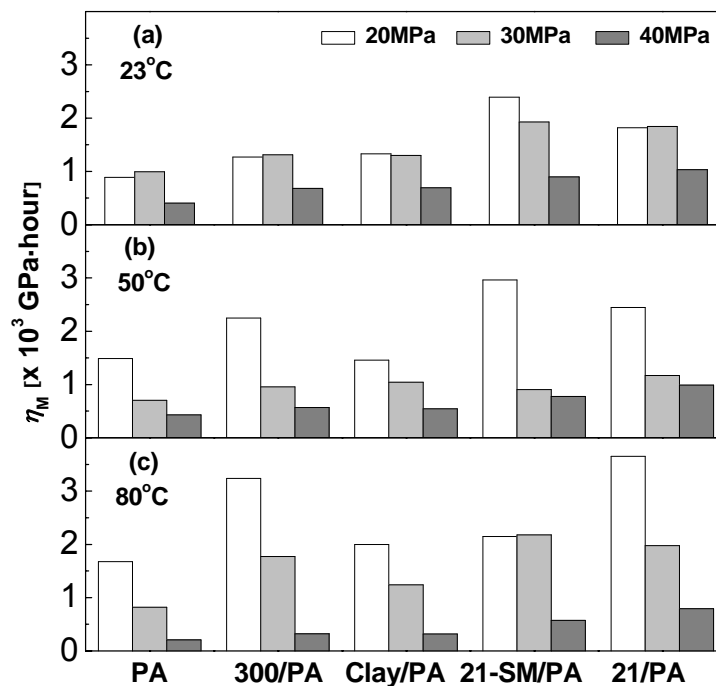
Figure 8.2: Model parameter η_M showing stress effects at **(a)** 23 °C, **(b)** 50 °C, and **(c)** 80 °C.

and very sensitive to stress except at 23 °C below 30 MPa, as compared in Figure 8.2 showing stress influence and Figure 8.3 showing temperature effect. It was therefore necessary to develop a more detailed understanding of η_M.

From Table 8.1 it can be seen that η_M was not strongly dependent on temperature, like E_M, E_K and η_K. It could be considered that η_M was associated with the damage from crystallized polymer or oriented noncrystalline regions, such as the pulling out of chain folds by a crystal slip process and the breaking of an intercrystalline tie molecule, and with the irreversible deformation from amorphous regions, such as the breaking or detaching of bridging segments, disengaged junctions between fillers and polymer chains, and the pulling out of a chain entanglement, as illustrated in Figure 5.9. Therefore a stress activated Eyring process was adopted as introduced in a previous chapter. The activation volume under higher stress levels is given in Table 8.1 and is discussed in the following analysis.

At room temperature, η_M was not sensitive to stress below 30 MPa while it decreased under 40 MPa, as clearly demonstrated in Figure 8.2(a), which shows that the damage to crystallized polymers was of the same level under low stress but became severe under high stress or when the elastic limit of crystallized regions was exceeded. Under low stress the Eyring process was probably associated with the separation of segment or crystalline bridging, while under 40 MPa the activated process corresponded to the large plastic deformation of crystallized polymer, as shown in Figure 5.9. Enhanced non-deformability of the Eyring dashpot was obtained due to the presence of nanofillers, which changed the crystalline morphology of the matrix and formed a stiff three dimensional network together with crystallized molecules. This could also be explained by considering the change of activation volume. The activation volumes of all composites were smaller than that of pure PA (~0.59 nm^3) at RT to different extents, as shown in Table 8.1, suggesting that the mobile unit of polymer chains was restricted to a small local region. Among the composites, 21/PA displayed the smallest activation volume and the highest η_M and thus best non-deformability, followed by 21-SM/PA. Large particles and nanoclay layers exhibited similar performance.

At 50 °C, η_M decreased significantly with increasing stress, reflecting the increment of irrecoverable deformation, as shown in Figure 8.2(b). The activation volume of each specimen was smaller than that at 23 °C, indicating a much more local molecular process near T_g, such as the breaking of an intercrystalline tie molecule and detaching of a polymer-filler junction, as illustrated in Figure 5.9. The irreversible creep strain was diminished by the addition of nanofillers, which enhanced the immobility of polymer chains and resulted in a much more local Eyring process. 21/PA displayed the least permanent deformation while 21-SM/PA showed the smallest activation volume due to uniform dispersion of particles with surface modification. Nanoclay layers had no obvious advantage over large nanoparticles in affecting the molecular process.

A similar scenario occurred at 80 °C in that η_M decreased considerably with increasing stress, as shown in Figure 8.2(c). However, an interesting phenomenon was that the activation volume of each specimen was larger than at any other temperature, probably indicating a different stress activated process at 80 °C. Polymer chains were highly thermally activated at this temperature and exhibited a rubber-like state. Large deformation of crystallized polymer, such as the pulling out of chain folds by a crystal slip process, and irreversible transition of amorphous polymer, such as the pulling out of chain entanglement or disentanglement under external stress [169, 170], occurred, which was relatively large scale cooperation of deformation. The stress activated process could be partially resisted by the presence of nanofillers, which retarded or prevented the slippage of crystallized polymer by reducing the size of the crystal part, and by disentanglement of amorphous chains acting as blocking sites. Among the observed fillers, small particles without surface modification showed the greatest effectiveness and resulted in the smallest activation volume, indicating that the mobile unit of polymer segments was still restricted to a much more local region even at the temperature above T_g. However, other composites displayed better η_M with a larger activation volume than neat matrix, indicating that the mobility of these fillers in matrix became more active compared with that of small particles without surface modification.

η_M showed an explicit dependence on stress and was explained using the Eyring

stress activated process. It is noteworthy to point out that η_M displayed much more complex dependence on temperature, as shown in Figure 8.3. In general, η_M increased with increasing temperature under 20 MPa except in the case of 21-SM/PA, in which η_M decreased at 80 °C, as illustrated in Figure 8.3(a). This scenario indicates that under low stress levels the permanent creep strain of each specimen decreased at elevated temperatures, which might be due to the load being too small to activate many polymer segments and then to damage polymer structure permanently at high temperatures. The bulk materials were more thermally than stress activated at elevated temperatures and thus displayed strong recoverableility capacity, confirmed by a decreased retardant time under 20 MPa, as shown in Table 8.1. However, at higher stress levels, e.g. 40 MPa, advanced creep processes were stress activated, such as slippage of crystallized polymer and disentanglement of amorphous polymer, on a large scale of mobility with great irreversible deformation and large activation volume, as shown in Figure 8.3(c) and Table 8.1, respectively. It is worth pointing out that under 30 MPa η_M showed an implicit dependence on temperature. η_M at 80 °C was only slightly changed compared to that at 23 °C for
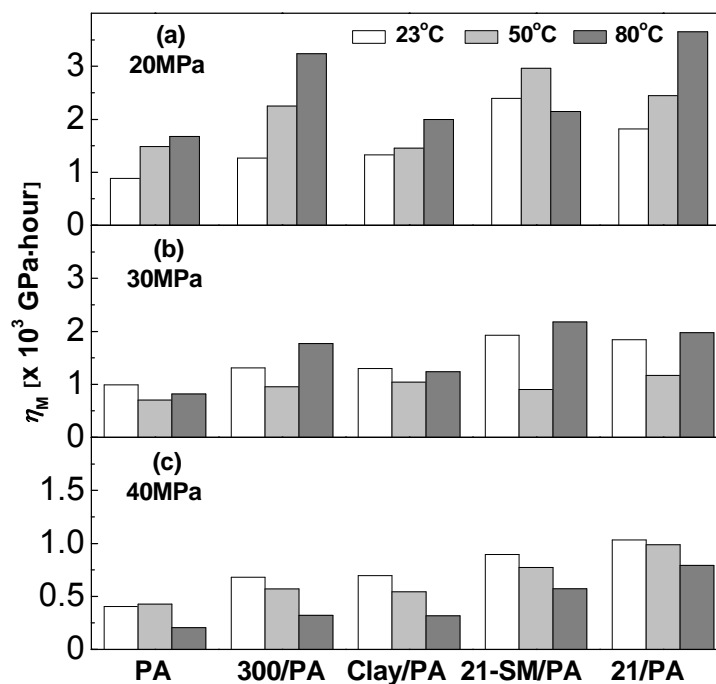
Figure 8.3: Model parameter η_M showing temperature effects under **(a)** 20 MPa, **(b)** 30 MPa, and **(c)** 40 MPa.

each specimen; however, it decreased markedly to a similar value for all observed materials at 50 °C, as shown in Figure 8.3(b). At 23 °C, since the materials were not thermally activated and the moderately low external stress could not cause a pronounced creep process, viscous flow was not obviously activated and was at a relatively low level. However, at 80 °C large instantaneous deformation resulted, due to the many thermally activated polymer chains under external stress. Therefore orientation of polymer chains occurred to great extent and resulted in high orientation hardening in the bulk materials [161, 168]. Thereafter advanced creep flow became much more difficult and the resulting η_M at 80 °C was very close to that at 23 °C. There was a different scenario at 50 °C, at which materials began to enter the glass transition region and the number of thermally activated chains was small. The most important feature was the degree of instantaneous deformation and orientation, which were very mild and resulted in lower orientation hardening than at 80 °C. This finding indicated that the materials had the potential to display advanced viscous flow with increasing time under this condition.

The stress or temperature dependent η_M displayed a consistency with the creep rate directly superimposed on the experimental data, as shown in Figure 8.2 and Figure 5.13, Figure 8.3 and Figures 5.14, 5.15 and 5.16. Considering Equation (4.11), when creep time $t \gg \tau$, the second term can be ignored and η_M becomes dominant in determining creep rate. A reciprocal relationship between η_M and creep rate is then simplified to Equation (4.12), and shown in the corresponding figures.

8.1.1.2 Findley power law

The Burgers model provided a constitutive representativeon and the modeling parameters showed the detailed structure-to-property relationship of the polymer composites. Additionally, an empirical model, the Findley power law, is frequently applied to simulate and predict long-term creep properties due to its simple expression and satisfactory applicability [1]. Here this method was also adopted to provide a broad understanding of the creep performance of the nanocomposites.

The simulated sample curves of specimens at 50 °C are illustrated in dashed lines in

Figure 8.1 under 20 MPa (a), 30 MPa (b), and 40 MPa (c). It can be seen that the superimposed curves agree very well with the experimental data. Since the power n of each specimen was not sensitive to stress, it was considered constant at each temperature. The complete modeling parameters ε_{F0}, ε_{F1} and n under each condition are listed in Table 8.3, from which an explicit dependency on both stress and temperature of the modeling parameters becomes evident. On the one hand, both the time-independent strain ε_{F0} and time-dependent term ε_{F1} show obvious growth with increasing stress level at each temperature; on the other hand, it illustrates the same behavior in that ε_{F0} and ε_{F1} increased with increasing temperature under each stress level. However, the increasing amplitude of ε_{F1} quickly slowed from 50 °C to 80 °C under stress below 30 MPa, showing that ε_{F1} was not sensitive to temperature under a moderately low stress level. The behavior of ε_{F0} was equivalent to the instantaneous deformation ε_{M1} in the Burgers model in nature, where the representative parameter is the elasticity E_M of the Maxwell spring. Additionally, the increments of ε_{F0} and ε_{F1} dependent on either temperature or stress were significantly reduced by the addition of nanofillers. In particular, 21/PA displayed the minimum ε_{F0} and ε_{F1}, followed by 21-SM/PA. 300/PA and Clay/PA both showed slight enhancement compared to the matrix PA66. The performance of ε_{F0} was consistent with that of E_M.

Table 8.3: The simulated parameters of the Findley power law.

Sample	σ_0 (MPa)	23 °C ε_{F0} (%)	ε_{F1} ($10^{-4}\,hr^{1/n}$)	n	50 °C ε_{F0} (%)	ε_{F1} ($10^{-4}\,hr^{1/n}$)	n	80 °C ε_{F0} (%)	ε_{F1} ($10^{-4}\,hr^{1/n}$)	n
PA66	20	0.312	15.0	0.296	1.826	143	0.0978	3.942	169	0.0658
	30	0.601	22.7		2.249	317		7.259	442	
	40	1.109	102.1		6.222	573		12.78	2380	
300/PA	20	0.862	13.3	0.276	1.360	84.5	0.108	2.955	86.7	0.0848
	30	0.994	24.8		1.834	188.4		6.159	185	
	40	1.105	71.0		4.173	394		11.30	1280	
/21-SM/PA	20	0.488	7.2	0.288	1.426	72.5	0.108	2.546	84.7	0.0896
	30	0.761	18.0		1.678	171		5.768	139	
	40	0.821	50.7		3.044	307		7.962	671	
21/PA	20	0.349	8.9	0.276	1.038	82.6	0.103	2.078	109	0.0663
	30	0.498	19.9		1.921	159		4.756	231	
	40	0.610	48.2		3.034	281		7.415	722	
Clay/PA	20	0.446	9.8	0.302	1.122	109	0.111	3.175	87.2	0.0951
	30	0.566	18.9		1.422	184		6.112	209	
	40	0.695	54.6		3.822	395		10.81	1160	

In addition, according to Equation (4.18), the fitting curves of Logarithm Strain Difference (creep strain ε_F - instantaneous strain ε_{F0}) versus Logarithm Time t for PA and 21/PA under various stress levels are provided in Figure 8.4 at 23 °C (a), 50 °C (b), and 80 °C (c). It can be seen that the fitting curves of each specimen are parallel and agree very well with the experimental data, especially over a large time span, indicating that the power n was independent of stress and state of stress. From the figures it can also be obvserved that the power n of 21/PA was almost the same as that of PA66 at 23 °C while slightly higher than that of PA66 at elevated temperatures. This phenomenon implies that the nanofillers used in this study did not greatly affect the parameter n, as shown in Table 8.3.

It can also be observed, however, that in the first few hours the fitting lines from the curves did not coincide well with the experimental ones. This finding might be due to the restriction of the loading system of the creep machine, by which the specimen was loaded to reach the desired stress asymptotically after some time [173], and the experimental data during the beginning stage were smaller than desired. The numbers on the left in Figure 8.4 indicate the strain at one hour. To determine the strain represented by the curves, shift the vertical scale to match this number.
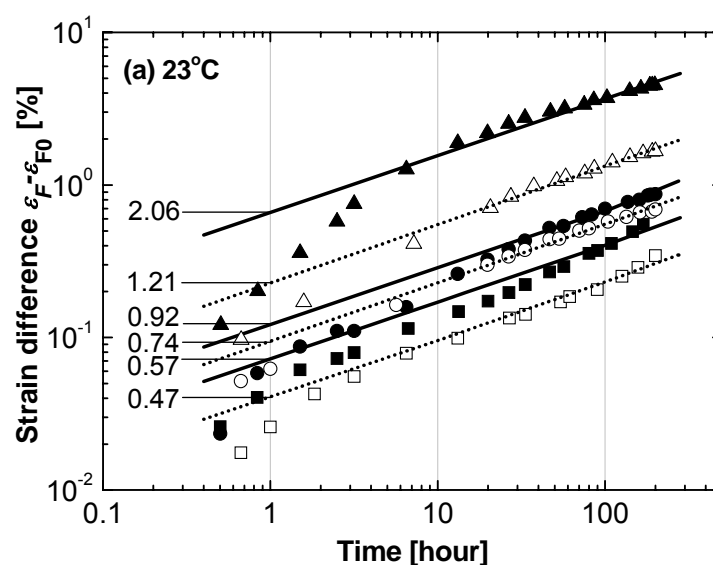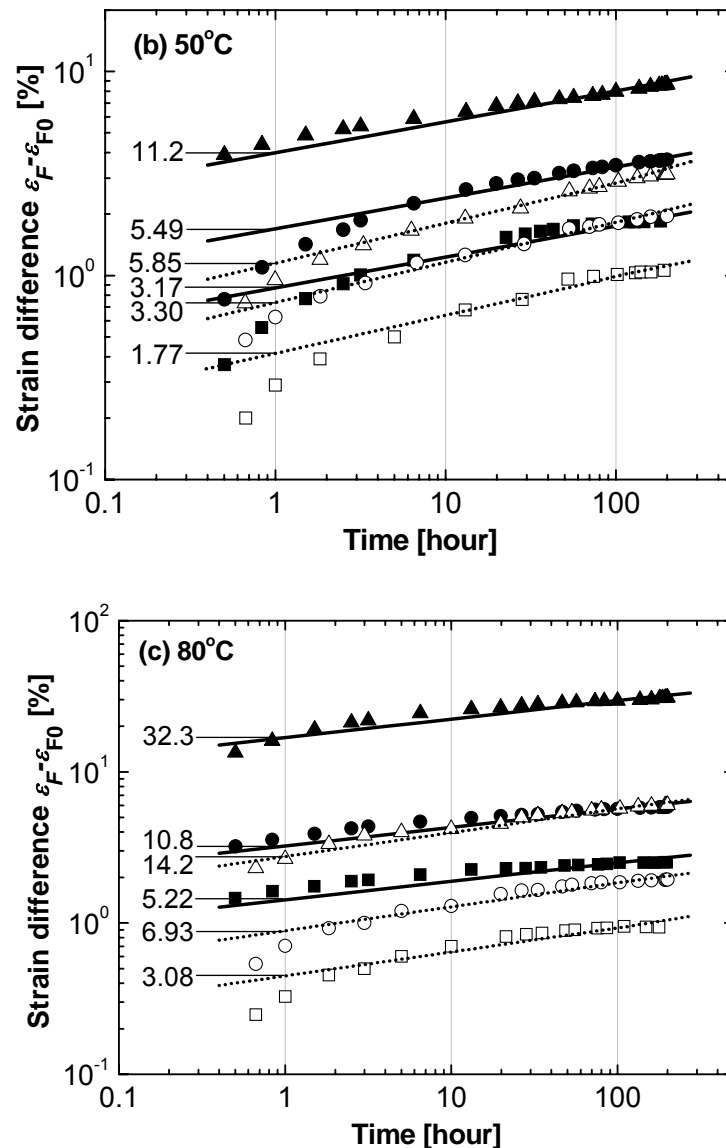
Figure 8.4: Log Strain Difference ε_F-ε_{F0} versus Log Time t for PA (solid symbols) and PA/21 (open symbols) at (a) 23 °C, (b) 50 °C, and (c) 80 °C. Discrete symbols are experimental data under different stress levels, Cube: 20 MPa, Circle: 30 MPa, Triangle: 40 MPa; Simulated results: PA (——), PA/21 (········). (Note: numbers on left indicate strain at one hour. To determine strain, shift the vertical scale to match this number.)

8.1.2 Nanoparticle/PP system

The simulated secondary creep curves using the Burgers model and the Findley power law, drawn with solid and dashed lines, respectively, are presented in Figure 8.5 with the experimental creep strain at 23 °C (a) and 50 °C (b). In the case of high

stress levels, i.e., 20 MPa at 23 °C and 14 MPa at 50 °C, the time when the minimum creep rate was reached was considered the end of the secondary creep stage. It can be seen that both modeling curves show good agreement with the experimental data under each condition. Comprehensive discussion of the model parameters is presented in the following subsections.

8.1.2.1 Burgers model

The complete modeling parameters of nanoparticle/PP material systems are listed in Table 8.4. Discussion based on these parameters is presented below.

I.   Time independent elasticity E_M

From Table 8.4 it can be found that the elasticity E_M of the materials exhibited similar trends of dependence on load level and temperature.

At ambient temperature, E_M of each specimen decreased with increasing load levels. Although E_M of 21/PP was very close to its Young's modulus under 8 MPa, in most cases E_M was lower than the corresponding Young's modulus, indicating that the applied stress levels were beyond the elastic limits and the materials deformed plastically even under stress as low as 8 MPa. In the nanoparticle composites, elasticity increased with decreasing particle size under each load, showing that small particles were more effective than large ones in reducing instantaneous plastic deformation.

At 50 °C, E_M was considerably lower than that at RT for each material under the same load level, indicating that plastic deformation became much more severe at elevated temperature. For each specimen E_M decreased from 8 MPa to 11 MPa but increased noticeably under 14 MPa with the highest value except for 300/PP, as listed in Table 8.4. This abnormal case of E_M under 14 MPa cannot be physically explained and remains a matter for further study. However, elasticity also improved with decreasing particle size, indicating that small nanoparticles could restrain plastic deformation effectively even at high temperature.
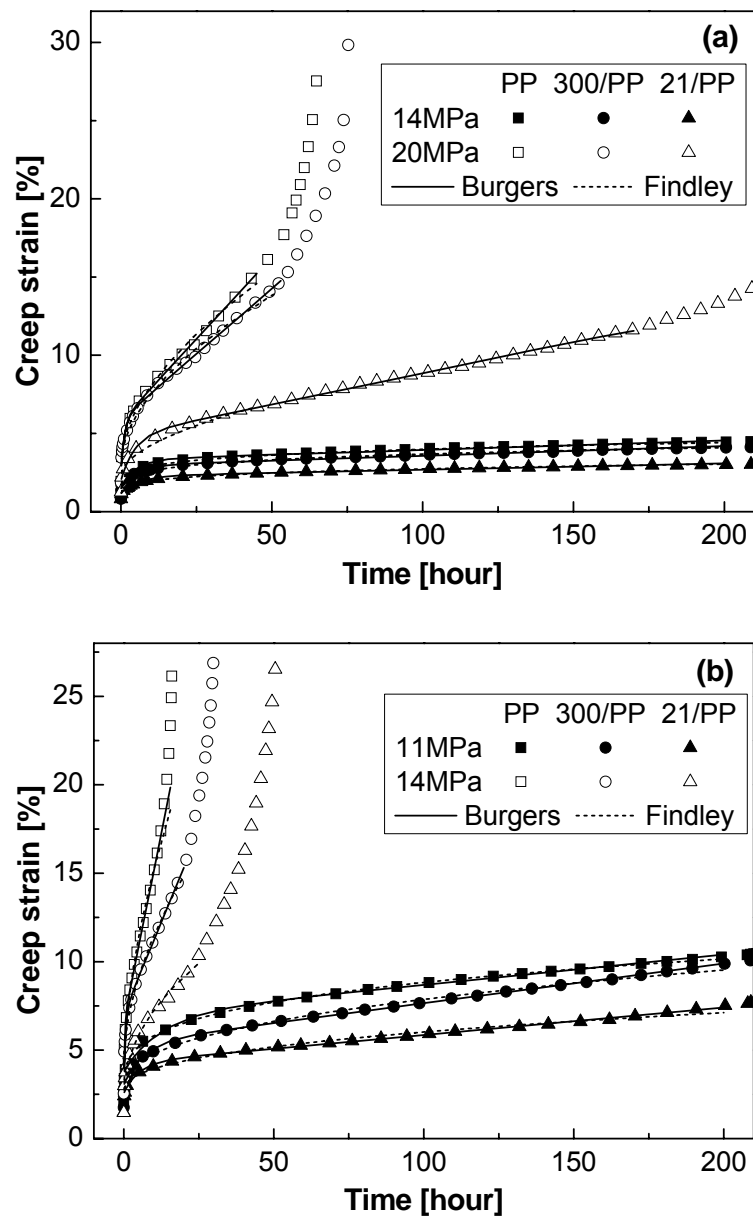
Figure 8.5: Sample modeling curves of creep strain versus creep time of nanoparticle/PP systems obtained at **(a)** 23 °C under 14 MPa and 20 MPa, and **(b)** 50 °C under 11 MPa and 14 MPa.

II. Retardant elasticity E_K and viscosity η_K

In Table 8.4 it can be easily seen that the retardant elasticity E_K and viscosity η_K of each material decreased with increase in either stress level or temperature. An alternative explanation is that the deformability of the Kelvin unit of each material increased with increasing stress level or temperature. However, the deformation of the spring was greatly retarded by the dashpot in the Kelvin unit. In addition, under

Table 8.4: The simulated parameters of the Burgers model and the activation volume υ calculated at higher stress levels.

T	Sample	σ_0 (MPa)	$E_{tensile}$ (MPa)	E_M (MPa)	E_K (MPa)	η_M (GPa·hr)	η_K (GPa·hr)	τ (hour)	υ (nm^3)
23°C	PP	8	1629	1085	1213	486	16.1	12.27	
		11		1019	962	383	10.4	10.8	
		14		897	789	231	3.97	5.04	
		20		718	662	9.56	0.811	1.22	2.694
	300/PP	8	1678	1460	1274	600	18.6	14.6	
		11		1281	1119	416	12.0	10.7	
		14		951	948	225	5.05	5.32	2.414
		20		752	616	12.0	0.769	1.25	(-10%)
	21/PP	8	1870	1866	1782	610	20.6	11.6	
		11		1282	1461	503	14.3	9.78	
		14		1176	1292	347	8.21	6.36	1.811
		20		991	708	49.9	3.26	4.60	(-33%)
50°C	PP	8	1047	431	551	217	4.31	7.82	
		11		290	345	64.4	4.32	12.5	
		14		505	361	1.65	0.102	0.28	5.857
	300/PP	8	1029	546	718	213	5.46	7.60	
		11		361	467	49.0	3.15	6.74	4.216
		14		420	372	3.41	0.242	0.65	(-28%)
	21/PP	8	1126	586	911	313	6.21	6.81	
		11		428	637	70.8	3.25	5.11	3.139
		14		734	452	6.85	0.336	0.744	(-46%)

$E_{tensile}$ is the Young's modulus obtained from the quasi-static tensile experiments. The activation volume υ was calculated under high stress levels (14-20MPa at 23°C and 11-14MPa at 50°C) with relative change of composites compared to the value of neat matrix.

the same condition nanoparticle/PP materials showed different behavior from nanoparticle/PA materials, in that E_K was very close to E_M in the former while considerably higher than E_M in the later. This might be due to the intrinsic differences between the matrices.

At room temperature, both E_K and η_K decreased clearly with increasing load, especially under the highest stress level, showing the increasing plastic deformation and orientational movement in the polymer chains. With increasing load, the rapid decrease of η_K compared to E_K led to a diminishing retardant time τ for each specimen. This finding implies that the retardant plastic deformation and orientational movement of polymer chains occurred in a much shorter time under high stress levels, as demonstrated in Table 8.4.

Since the mobility of polymer chains at 50 °C was much greater, the deformability of amorphous regions was markedly enhanced, with the result that both E_K and η_K decreased greatly compared to the values at RT. The retardant time τ also decreased considerably with increasing stress level, indicating that the retardant process of the Kelvin unit at 50 °C occurred in a much shorter time than at room temperature.

It should be pointed out that nanoparticles showed a positive effect on restraining the mobility of the Kelvin unit. Small particles were more effective in retarding the deformation of the Kelvin elements than large ones.

III. Permanent viscous flow η_M

Nanoparticles displayed some improvement in the instantaneous and time-dependent recoverable units of the Burgers model. The irrecoverable or permanent viscous flow of material was dominant in terms of η_M, which was a factor several to ten times higher than η_K. Unlike the nanoparticle/PA system, the η_M of nanoparticle/PP materials decreased markedly with increasing stress level or temperature, as shown in Table 8.4. As analyzed earlier, η_M was considered to be associated with the permanent damage of crystallized and amorphous regions. The activation volume under higher stress levels was also calculated and is given in Table 8.4.

At room or elevated temperatures, the materials showed nonlinear viscoelasticity and the Eyring rate process was activated even under stress as low as 8 MPa. The activation volumes of the observed specimens ranged from 1.8 to 6 nm^3, which were considerably larger than those in the PA systems (0.23~1.15 nm^3) and represented a large region of polymer segments participating as a whole in creep movement in the nanoparticle/PP system. This large scale cooperation of deformation of crystallized regions, such as the pulling out of chain folds by a crystal slip process, and the irreversible transition of amorphous regions, such as the pulling out of chain entanglement or the extreme disentanglement-induced orientation under external stress [169, 170], was considered to dominate the creep process. The marked

orientation deformation resulted in a highly regular rearrangement of amorphous segments and induced crystallization there, as shown in Figure 6.12 with increased crystallinity after creep failure under 20MPa/23°C.

However, the stress activated process in polymer could be partially resisted by the addition of nanoparticles, which retarded or prevented the slippage of crystallized polymer by reducing the size of the crystal part, e.g. spherulites shown in Figure 6.11, and disentanglement of amorphous chains acted as blocking sites. Small particles had better effectiveness than large ones and resulted in a smaller activation volume. Additionally, the orientation-induced crystallinity in 21/PP was slightly lower than that in 300/PP, as shown in Figure 6.12, indicating that the mobile unit of polymer segments was much more effectively restricted in a much more local region by small nanoparticles.

In addition, the stress or temperature dependent η_M indicated accordance with the creep rate directly fitting with the experimental data, as shown in Table 8.4 and Figure 6.8. It was confirmed again that η_M became dominant in determining the creep rate over a large time span.

8.1.2.2 Findley power law

The simulated curves of nanoparticle/PP system are illustrated by dashed lines in Figure 8.5 at (a) 23 °C under 14MPa and 20 MPa, and (b) 50 °C under 11 MPa and 14 MPa, respectively. It can be seen that the simulated curves agree quite well with the experimental data. The complete modeling parameters ε_{F0}, ε_{F1} and n under each condition are listed in Table 8.5, respectively, from which an explicit dependency both on stress and on temperature of the modeling parameters can be seen. The time-independent strain ε_{F0} was not sensitive to low stress levels at RT, but increased rapidly at 50 °C under each load level and at RT only under high load. The time-dependent term ε_{F1} showed obvious growth under low stress levels at RT and under high stress levels at 50 °C. It could alternatively be explained that ε_{F1} was insensitive to high loads (>14 MPa) at RT and to low loads (<11 MPa) at 50 °C. ε_{F0} and ε_{F1} exhibited similar temperature dependence, increasing with increasing

Table 8.5: The simulated parameters of the Findley power law.

T	Sample	σ_0 (MPa)	ε_{F0} (%)	ε_{F1} (10^{-2}hour$^{1/n}$)	n
23 °C	PP	8	0.3766	0.4795	0.1966
		11	0.4718	0.9135	0.1761
		14	0.9537	1.2543	0.1943
		20	3.2717	1.2892	0.5709
	300/PP	8	0.1918	0.4387	0.2019
		11	0.2311	0.7892	0.1894
		14	0.6074	1.3278	0.1816
		20	3.0065	1.3026	0.5413
	21/PP	8	0.1995	0.3065	0.2123
		11	0.3617	0.6327	0.1851
		14	0.6164	0.8727	0.1926
		20	2.2970	0.5626	0.5413
50 °C	PP	8	1.0556	1.2983	0.1557
		11	2.3043	1.8932	0.2685
		14	3.4412	3.2375	0.5624
	300/PP	8	0.7183	1.0028	0.1783
		11	2.8916	0.7378	0.4145
		14	4.2096	2.0489	0.5500
	21/PP	8	0.6922	0.9117	0.1524
		11	2.5890	0.5460	0.3992
		14	2.0855	1.8265	0.4519

temperature under each stress level. Additionally, the increments of ε_{F0} and ε_{F1} dependent on either temperature or stress were reduced by the addition of nanoparticles, and 21/PA displayed lower ε_{F0} and ε_{F1} than 300/PP, as listed in Table 8.5.

The power n was almost invariant under low stress levels but increased rapidly under 20 MPa at room temperature. It increased clearly with increasing stress level at elevated temperature. However, nanoparticles did not affect the value of power under each condition, as shown in Table 8.5. This finding implies that for nanoparticle/PP system the power n in the Findley model was controlled by the polymer matrix and the fillers had no influence.

8.1.3 MWNT/PP system

The simulated secondary creep curves using Burgers model and Findley power law are drawn in solid and dashed lines, respectively, in Figure 8.6 with the experimental data at 23 °C (a) and 50 °C (b). In the case of high stress levels, i.e., 20 MPa at 23 °C and 14 MPa at 50 °C, the time at which the minimum creep rate reached was considered to be the end of the secondary creep stage. It can be seen that both modeling curves showed good agreement with the experimental data under each condition. Detailed discussion of the model parameters is provided in the following subsections.

8.1.3.1 Burgers model

The entire modeling parameters of the MWNT/PP materials are listed in Table 8.6. It was found that in the case of MWNT/PP system the aspect ratio of nanotubes played an unimportant role in enhancing the elasticity of the Maxwell spring, i.e. both S- and L-MWNTs improved the Burgers model parameter equally, resulting from their similar experimental performance. Detailed discussion based on the parameters is presented below.

I.   Time independent elasticity E_M

It can also be seen from Table 8.6 that the elasticity E_M of each specimen displayed a close tendency of dependence on stress and temperature, which was similar to the case of nanoparticle/PP system.

At RT, the E_M of the composites decreased with a rapid decrease from 8 MPa to 11 MPa and a smooth reduction from 11 MPa to 20 MPa. Although E_M of the composites was slightly higher than their Young's moduli under 8 MPa, in other cases E_M was smaller than the corresponding modulus, suggesting that the stress levels applied were beyond the elastic limits and the materials deformed plastically. The elasticity of the composites was increased compared to that of the base matrix under each load, showing that nanotubes were effective in reducing instantaneous plastic deformation via successful load transfer effect.
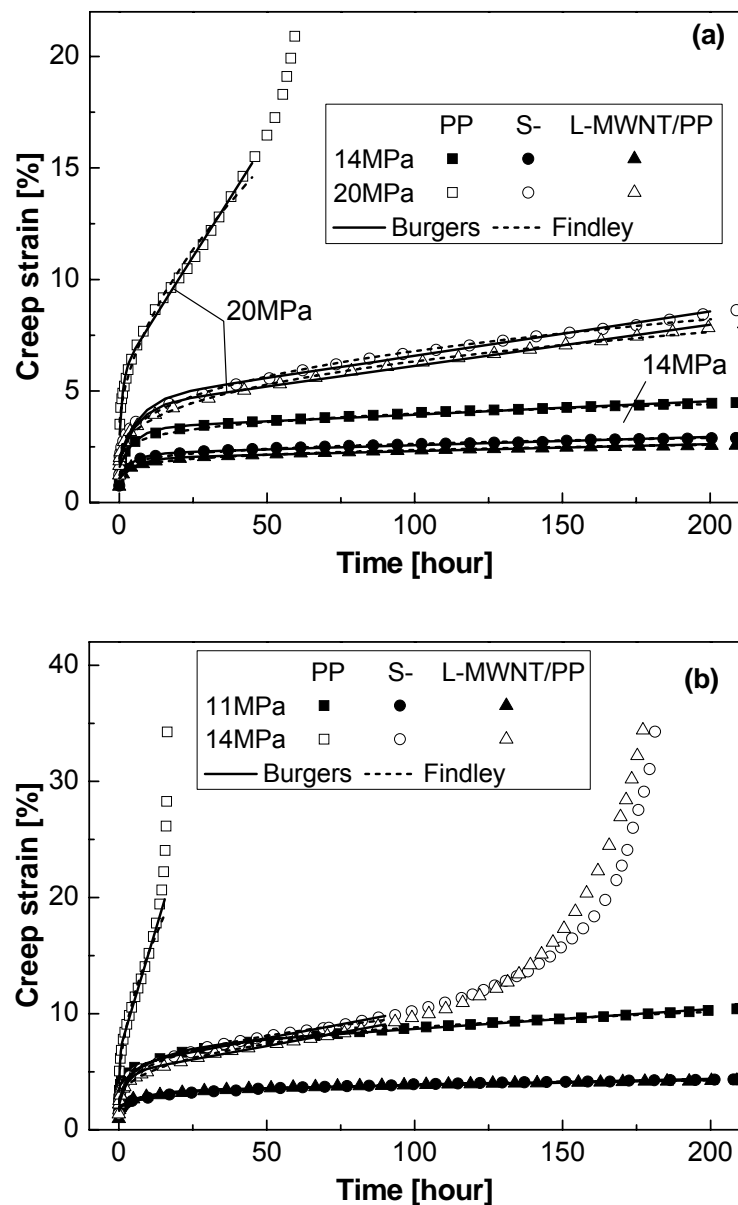
Figure 8.6: Sample modeling curves of creep strain versus creep time of MWNT/PP system obtained at **(a)** 23 °C under 14 MPa and 20 MPa, and **(b)** 50 °C under 11 MPa and 14 MPa.

At elevated temperature E_M was considerably lower than that at RT for each material under the same load level, indicating that plastic deformation became much more severe. E_M for the composites was obviously higher than that of matrix and decreased from 8 MPa to 11 Mpa, but changed only slightly from 11 MPa to 14 MPa (almost no variation for S-MWNT/PP but a little increase for L-MWNT/PP), as listed in Table 8.6. This abnormal finding for E_M under 14 MPa, as mentioned in the case of the nanoparticle/PP system, cannot be physically explained.

Table 8.6: The simulated parameters of the Burgers model and the activation volume _ calculated at higher stress levels.

T	Sample	σ_0 (MPa)	$E_{tensile}$ (MPa)	E_M (MPa)	E_K (MPa)	η_M (GPa·hr)	η_K (GPa·hr)	τ (hour)	υ (nm^3)
23°C	PP	8	1629	1085	1213	486	16.1	12.27	
		11		1019	962	383	10.4	10.8	
		14		897	789	231	3.97	5.04	
		20		718	662	9.56	0.811	1.22	2.694
	S-MWNT/PP	8	1870	2531	1918	728	27.4	14.3	
		11		1531	1695	527	16.0	9.43	
		14		1173	1401	371	7.00	5.00	1.426
		20		1007	768	101	5.04	6.57	(-47%)
	L-MWNT/PP	8	2076	2702	2107	815	26.5	12.6	
		11		1600	1831	740	21.0	11.5	
		14		1302	1531	444	9.08	5.93	1.439
		20		1119	802	108	4.66	5.81	(-47%)
50°C	PP	8	1047	431	551	217	4.31	7.82	
		11		290	345	64.4	4.32	12.5	
		14		505	361	1.65	0.102	0.28	5.857
	S-MWNT/PP	8	1239	724	970	329	6.06	6.24	
		11		579	782	203	8.46	10.8	3.617
		14		565	460	29.5	1.66	3.61	(-38%)
	L-MWNT/PP	8	1304	844	1146	401	8.03	7.00	
		11		553	800	237	7.49	9.36	3.573
		14		672	499	30.1	1.40	2.80	(-39%)

$E_{tensile}$ is the Young's modulus obtained from the quasi-static tensile experiments. The activation volume υ was calculated under high stress levels (14-20MPa at 23°C and 11-14MPa at 50°C) with relative change of composites compared to the value of neat matrix.

II. Retardant elasticity E_K and viscosity η_K

In Table 8.6 it was shown that the retardant elasticity E_K and viscosity η_K of the nanotube composites decreased with increase in either stress level or temperature. This could also be explained by the deformability of the Kelvin unit of each material increasing with increasing stress level or temperature. However, the deformation of the spring was greatly retarded by the dashpot in the Kelvin unit.

At ambient temperature, both E_K and η_K clearly decreased with increasing load, especially under the highest stress level, showing the increasing plastic deformation and orientational movement in polymer chains. With increasing load, the rapid decrease in η_K compared to E_K led to a diminishing retardant time τ for each

specimen, while τ did not vary between 14 MPa to 20 MPa for the composites. These findings indicate that the retardant plastic deformation and orientational movement of polymer chains proceeded in a much shorter time under high stress levels but were retarded by the presence of nanotubes, as shown in Table 8.6.

Since polymer chains were highly thermally activated at 50 °C the deformability of amorphous regions was greatly increased, which meant that E_K and η_K were obviously decreased compared to their values at RT. E_K also decreased with increasing stress level. η_K remained almost constant from 8 MPa to 11 MPa but diminished quickly under 14 MPa. The retardant time τ roughly showed no change under stresses below 11MPa but decreased under 14 MPa, indicating that the retardant process of the Kelvin unit at 50 °C occurred in a much shorter time under high stress level and was retarded by the addition of nanotubes.

III. Permanent viscous flow η_M

Carbon nanotubes effected improvement in the instantaneous and time-dependent recoverable units of the Burgers model. The irrecoverable viscous flow, η_M, of nanotube composites was also higher by a factor of tens to hundreds than the corresponding η_K, indicating that nanotubes displayed better reinforcing effectiveness than nanoparticles in PP matrix, as shown in Table 8.6. A different reinforcing mechanism of load transfer in nanotube composites from that of the filler network in nanoparticle composites was used in the earlier discussion to explain the resulting enhancement.

At either 23 °C or 50 °C, the composites also showed nonlinear viscoelasticity, and the Eyring rate process was activated even under the low stress level of 8 MPa. The activation volume in the observed composites was reduced by roughly 50 % and 40 % at RT and elevated temperature, respectively, compared to that in neat matrix. This finding implies that the large region of polymer segments which participated as a whole in the creep process in neat PP matrix was restricted to a much more local area in the nanotube composites. Other observations from the crystallinity change of the materials before and after creep failure also confirmed the above results. The

orientation-induced crystallinity increase was 4.7 % in neat PP, 3.5 % in S-MWNT/PP, and 1.8 % in L-MWNT/PP, as shown in Figure 7.10. This finding indicates that nanotubes effectively constrained the orientation movement of amorphous segments, and long tubes were more effective than short ones at this point. However, much more serious intertube slippage or even tube pullout could occur in L-MWNTs [107, 127] that discounted their advantage and led to a reinforcing effectiveness close to that of S-MWNTs.

8.1.3.2 Findley power law

The simulated curves of the MWNT/PP system using the Findley power law are also presented with dashed lines in Figure 8.6 at (a) 23 °C under 14MPa and 20 MPa, and (b) 50 °C under 11 MPa and 14 MPa, respectively. The simulated curves agree very well with the experimental data. The complete modeling parameters ε_{F0}, ε_{F1} and n under each condition are listed in Table 8.7. A clear dependence of the modeling parameters on both stress and temperature was observed. The time-independent strain ε_{F0} increased slowly under low stress levels at RT, increased noticeably at 50 °C under each load level and at RT only under under high load level. The time-dependent term ε_{F1} showed obvious growth under each stress levels at either RT or 50 °C. ε_{F0} and ε_{F1} exhibited similar temperature dependence, increasing with increasing temperature under each stress level. Additionally, the increase in ε_{F0} and ε_{F1} with stress or temperature was slowed by the addition of nanotubes, as shown in Table 8.7.

At either room or elevated temperature the power n of each material was varied only slightly under low stress levels while rapidly increasing under high load. Unlike the finding in nanoparticle/PP system where the power n of the materials was very similar under the same stress level, MWNTs showed a clear reduction in power n, especially under high stress levels, as shown in Table 8.7. This case implies that for MWNT/PP system the power n in the Findley model was influenced to large extent by nanotubes.

Table 8.7: The simulated parameters of the Findley power law.

T	Sample	σ_0 (MPa)	ε_{F0} (%)	ε_{F1} ($10^{-2}hr^{1/n}$)	n
23 °C	PP	8	0.3766	0.4795	0.1966
		11	0.4718	0.9135	0.1761
		14	0.9537	1.2543	0.1943
		20	3.2717	1.2892	0.5709
	S-MWNT/PP	8	0.1099	0.2607	0.2242
		11	0.3053	0.5327	0.1917
		14	0.5997	0.9360	0.1687
		20	1.4821	1.0839	0.3450
	L-MWNT/PP	8	0.0886	0.2673	0.2050
		11	0.2742	0.5032	0.1828
		14	0.5621	0.7886	0.1781
		20	1.4255	1.0127	0.3427
50 °C	PP	8	1.0556	1.2983	0.1557
		11	2.3043	1.8932	0.2685
		14	3.4412	3.2375	0.5624
	S-MWNT/PP	8	0.4991	0.8504	0.1512
		11	0.8347	1.2381	0.1964
		14	1.6392	1.8215	0.3238
	L-MWNT/PP	8	0.3755	0.7557	0.1481
		11	0.7734	1.4498	0.1650
		14	1.6471	1.4967	0.3447

8.2 Prediction of long-term behaviors

8.2.1 Prediction by using creep models

8.2.1.1 The predicting ability of the models

Both the Burgers model and the Findley power law were successfully applied to simulate the experimental data. Here these two models are compared to predict the long-term creep behaviors based on the short-term experimental data, which were part of the long-term experimental data. The prediction results together with the experimental strains are shown in Figure 8.7 for (a) PA systems based on 100-hour creep data to predict 350-hour data under 80°C/30MPa, and (b) PP systems based on 200-hour creep data to predict 800-hour data.

Although both models displayed satisfactory simulation performance within the base

data, their predictive abilities were very different. It can obviously be seen that over the prediction period the results from the Findley power law were very close to the experimental data; the results from the Burgers model, however, showed huge deviation from the experimental data, as shown in Figure 8.7. The strains and relative deviations of the models from the experimental data were selected at a certain time in the prediction period, i.e. the 350th hour for PA system and the 800th
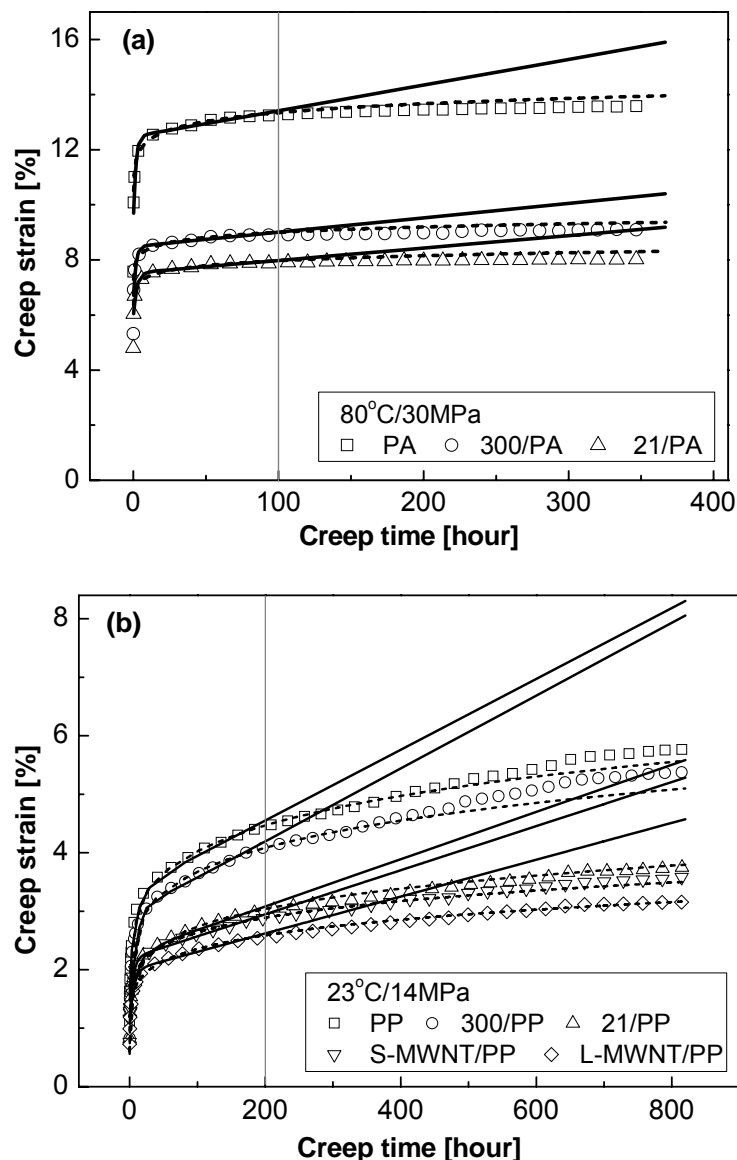

Figure 8.7: Comparison of the experimental data and the predicted results of the Burgers model (——) and Findley power law (------) for **(a)** PA system based on 100-hour creep to predict 350-hour data under 30MPa/80°C, and **(b)** PP system based on 200-hour creep to predict 800-hour data under 14MPa/23°C.

Table 8.8: The deviation of long-term creep strain predicted by models from the experimental data.

Specimen	Condition	$\varepsilon_{experimental}$ (%)	$^{\dagger}\varepsilon_{Burgers}$ (%)	$^{\dagger}\varepsilon_{Findley}$ (%)
PA66	80 °C / 30 MPa	13.6	15.7 (+15%)	13.9 (+2.2%)
300/PA	(100-hour →	9.11	10.3 (+13%)	9.35 (+2.6%)
21/PA	350-hour)	8.02	9.11 (+14%)	8.30 (+3.5%)
PP	23 °C / 14 MPa	5.76	8.18 (+42%)	5.55 (-3.6%)
300/PP	(200-hour →	5.37	7.93(+48%)	5.08 (-5.4%)
21/PP	800-hour)	3.75	5.50 (+47%)	3.78 (+0.8%)
S-MWNT/PP		3.57	5.21 (+46%)	3.49 (-2.2%)
L-MWNT/PP		3.15	4.51 (+43%)	3.16 (+0.3%)

† The percentage in brackets is the relative change in the predicted value compared to the corresponding experimental datum.

hour for PP system. The results and comparison are listed in Table 8.8. In the case of PA systems, the relative deviation (RD) of the Burgers model from the experimentaldata was greater than 13 %; however, the RD of the Findley power law was less than 3.5 %, which was in quite an acceptable range. In the case of the PP systems, the RD of the Burgers model and Findley power law was above 42 % and below 5 %, respectively. The high deviation of the Burgers model means that it was incapable of predicting long-term behavior, whereas the Findley power law displayed extremely good predictive ability, e.g. its RD was within 0.3 % for L-MWNT/PP in Table 8.8.

The distinct predicting ability of the models might result from their intrinsic differences. As described in Burgers model, both the Kelvin unit and Maxwell dashpot were time-dependent. According to the earlier simulated results, the model parameters basically represented the current status of material and were very variable if the structure of the material changed with time. Consequently, the parameters of the Burgers model obtained at the current time could not be applied to satisfactorily describe the future behavior of material. Comparatively, the creep rate equation of the Findley power law could imply the actual case that the thermoplastic nanocomposites displayed a non-pronounced secondary creep stage under

moderate or low stress levels with nearly constant creep rate, which was insensitive to time. Therefore it was capable of satisfactorily predicting the creep characteristics even over a large time span, as shown in Figure 8.7.

8.2.1.2 Application of Findley power law

In the above section the predictive ability of the models was compared and the Findley power law was verified as an effective method. Some example applications are provided here using the power law.

Experiments performed under low stress levels were considered and the prediction based on the experimental data was executed within 2000 hours. The predicted results for PA and PP systems are given below.

From the example applications displayed in Figures 8.8 and 8.9, it can be seen that the power law displayed extremely good predictive performance. This is the reason that it is widely applied in engineering applications [1]. Although the power law exhibited good predictive ability, there was still a deficiency in that it could only be applied in cases where there had been no pronounced deformation, i.e., normally
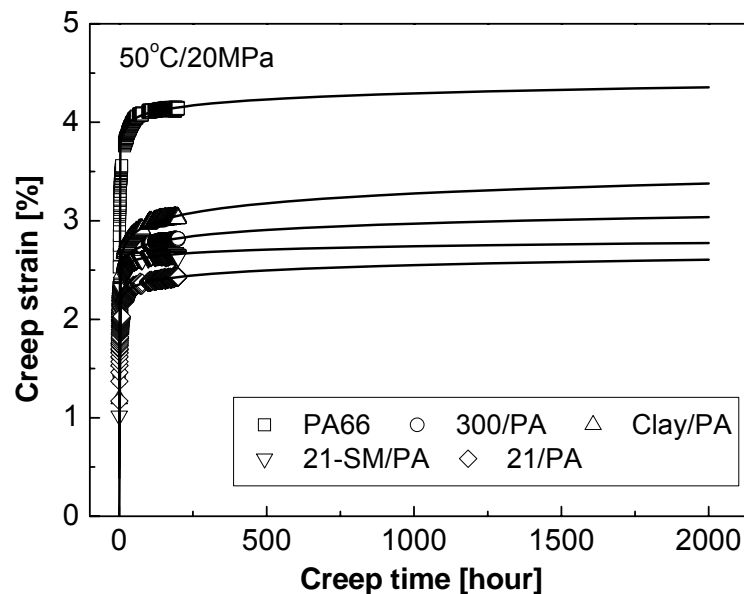

Figure 8.8: The predicted creep strains within 2000 hours of PA system using Findley power law. Symbols: experimental data, solid lines: predicted results.
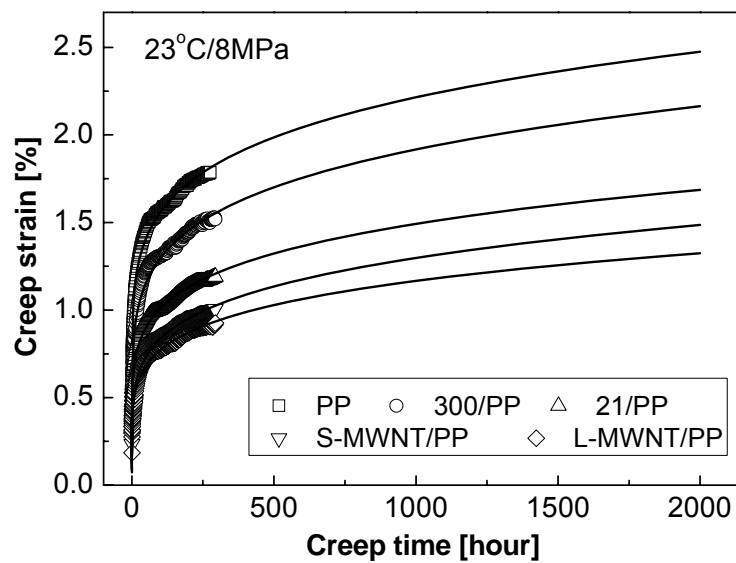
Figure 8.9: The predicted creep strains within 2000 hours of PP system using Findley power law. Symbols: experimental data, solid lines: predicted results.

under low stress levels. If there was indeed an accelerating deformation the power law became invalid.

8.2.2 Prediction using time-temperature-stress superposition method

8.2.2.1 Application of time-temperature superposition principle

The analysis in the former subsection confirmed that the Findley power law was a satisfactory way to predict long-term creep performance. We would, however, like to provide another method, the time-temperature superposition principle (TTSP), for observing the long-term properties of nanoparticle/PA composites. The creep strains were measured at 23 °C, 40 °C, and 50 °C, respectively, under a constant load of 15 MPa over an appropriate time span to ensure strain overlap at neighboring temperatures. The sample curves of PA66 and 21/PA are presented in terms of creep compliance in Figure 8.10(a). It can also be seen that both creep compliance and creep rate were significantly reduced in 21/PA at each temperature. The master curves are illustrated in Figure 8.10(b) with the simulation results using the Findley power law. The master curves were extended up to 10^{10} seconds in the time scale. The creep compliance of 21/PA was obviously lower than that of PA, which showed the reinforcing effectiveness of nanoparticles. The increment of compliance with time slowed from 10^9~10^{10} seconds, showing that the materials entered a rubbery state
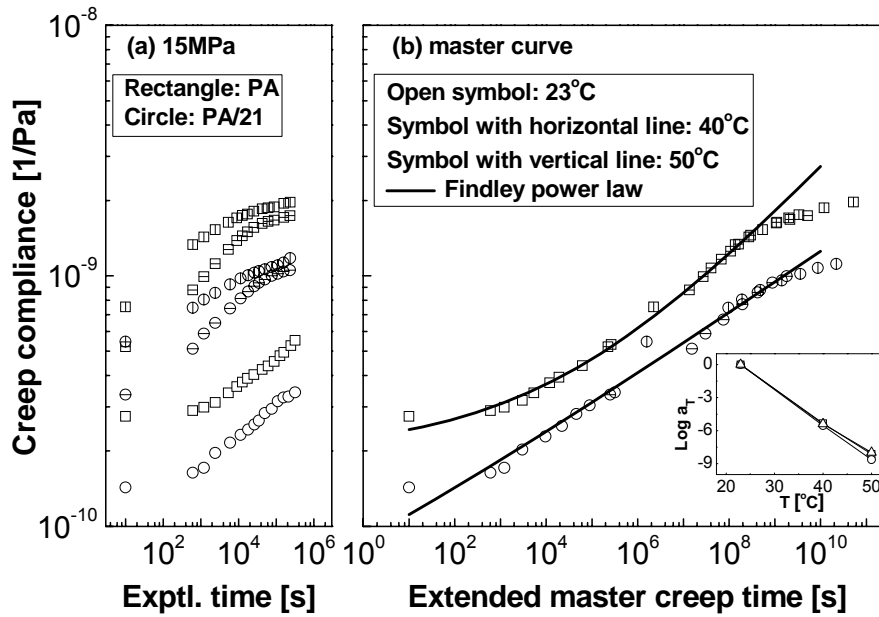
Figure 8.10: TTSP applied in nanoparticle/PA system. **(a)** The experimental creep data obtained under 15 MPa at different temperatures; **(b)** The master curves obtained at the reference temperature of 23 °C; The insertion graph shows the shifting factor a_T as a function of temperature.

after an extremely long period of time [2]. Additionally, the shifting factor a_T showed good linear dependence on temperature, as illustrated in Figure 8.10(b) with the insertion graph.

8.2.2.2 Application of time-stress superposition principle

In addition to TTSP, another method that could predict long-term properties based on short-term experiments is the time-stress superposition principle (TSSP) introduced earlier. As an example application of TSSP method, the experimental data of the PP system under different stress levels are shown in Figure 8.11(a).

The experimental data were horizontally shifted on the reference stress of 8 MPa to provide a best overlap. The master curves of PP, 21/PP and L-MWNT/PP are presented in Figure 8.11(b). The master creep compliance was then greatly extended up to 16,000, 80,000, and 600,000 hours until failure for PP, 21/PP, and L-MWNT/PP, respectively. These findings indicated that the creep lifetime of neat PP under 8 MPa was improved by 500 % and 3,800 % by the addition of nanoparticles

and carbon nanotubes, respectively.
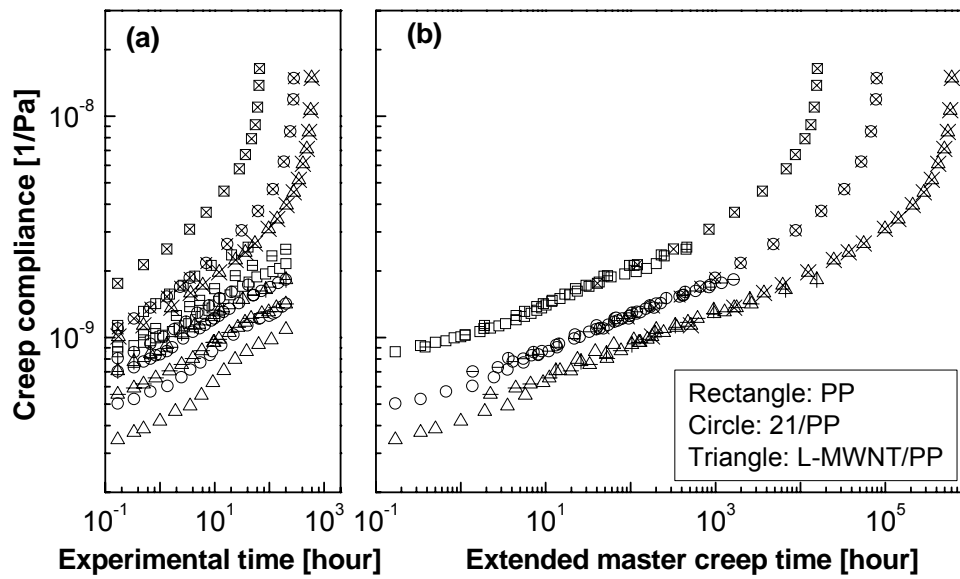
Figure 8.11: TSSP method applied to PP system. **(a)** The experimental creep data performed under various stress levels at 23 °C; **(b)** The master curves obtained on the basis of the reference stress of 8 MPa.

9   Summary and Outlook

The current work was focused on the characterization, modeling and prediction of creep resistant nanocomposites. For this purpose, different types of nanofillers, i.e. TiO_2 nanoparticles, nanoclay platelets and multiwalled carbon nanotubes, were compounded with two kinds of thermoplastics, PA66 and PP, to observe the creep resistance of the nanocomposites. Creep modeling analysis and prediction methods were also applied in order to comprehensively understand these behaviors. The results and conclusions obtained in this work are summarized in the following paragraphs. Suggestions for future studies are also given.

Nanoparticle/PA system

In this material system, tensile creep experiments were carried out under different stress levels at room and elevated temperatures. Additionally static tensile tests were performed at corresponding temperatures. The creep deformation, isochronous stress-strain relationship, creep rate and creep compliance were obtained and generally discussed both according to the changes in polymer structure based on the experimental results and according to orientational hardening and thermally and stress activated process methods. The creep characterization of PA66 and nanocomposites was concluded as follows:

➢ The static tensile properties of nanocomposites were not seriously impaired by the addition of nanofillers compared to those of neat PA66 matrix.

➢ The creep deformation and creep rate displayed complex dependence on temperature and stress level with thermally and stress activated processes. Both parameters decreased to different extents with the addition of nanofillers. Among the changes, the greatest reductions in creep strain and creep rate were found in 21/PA by 62 % and 67 %, respectively, compared to matrix. Accordingly the dimensional stability of the bulk nanocomposites was enhanced.

➢ The limits of linear viscoelasticity could be obtained from the isochronous stress-strain relationship and decreased with increasing temperature. The limits of the

nanocomposites were higher than those of neat matrix, with approximate values of 30 MPa at 23 °C, 20-30 MPa at 50 °C, and 20 MPa at 80 °C, respectively.

➢ The creep compliance analysis confirmed the conclusion obtained in (3). Additionally, creep compliance was decreased by the addition of nanofillers. A rubbery-like or flow state with nonlinear viscoelasticity was observed at elevated temperatures.

➢ Creep resistance was enhanced by the addition of nanofillers. Clay/PA exhibited compromised performance close to that of 300/PA due to the slippage of non-exfoliated clay layers under shear stress resulting from viscous flow of the matrix. Although good dispersion occurred in 21-SM/PA, poor interfacial strength discounted the reinforcing effectiveness under some conditions. All in all, small sized nanoparticle modified PA66 displayed the best creep resistance.

Nanoparticle/PP system

In this material system, nanoparticles exhibited similar experimental results to those of the PA system. With observed temperatures above T_g the materials showed nonlinear viscoelasticity even under low stress levels. Creep deformation and creep rate displayed a clear temperature and stress dependence. The detailed conclusions drawn were as follows:

➢ The static tensile properties of nanoparticle/PP composites were not seriously impaired compared to those of PP matrix.

➢ The creep deformation and creep rate increased with increasing temperature and stress levels, especially under high stress levels. Both the parameters were decreased to different extents by the addition of nanoparticles. Small particles displayed more capacity to improve creep resistance than large ones. The dense 3-D network formed by small particles with close interparticle distance could effectively restrict the mobility of polymer chains.

➢ Due to low T_g, the materials showed nonlinear viscoelasticity under the observed conditions. The creep compliance confirmed this observation and was decreased by the addition of nanoparticles.

MWNT/PP system

Carbon nanotubes showed a much better reinforcing ability than nanoparticles due to their different dimension and extremely good properties. Nanotubes with large aspect ratio were considered an advantage resulting in load transfer effect, which was a key factor in reinforcing the properties of matrix. Detailed conclusions were drawn as follows:

➢ The static tensile properties of MWNT/PP composites were not obviously reduced compared to those of PP matrix.

➢ Nanotubes greatly improved the creep resistance of the matrix, with significantly reduced creep deformation and creep rate. Additionally, the creep lifetime of the composites was considerably extended by 1,000 % compared to that of neat matrix at elevated temperature. This improvement in creep resistance was attributed to efficient load transfer between the carbon nanotubes and surrounding polymer chains.

➢ The existence of intertube slip caused a decrement in the improvement. Intertube slip could become more serious under high stress levels in large aspect ratio tubes than in those with small aspect ratio, greatly decreasing the reinforcing effectiveness of L-MWNTs and leading to a similar performance to S-MWNTs.

➢ These findings should lead to improved grades of creep resistant polymer nanocomposites for engineering applications.

Modeling analysis and prediction of long-term behaviors

The modeling results and prediction of long-term creep behaviors provided a comprehensive understanding of creep of the composites. Both the Burgers model and the Findley power law were applied to satisfactorily simulate the experimental data. In addition, parameter analysis based on the Burgers model provided a possible explanation of structure-to-property relationships in nanocomposites. Due to their intrinsic features, the Findley power law was better able than the Burgers model to predict long-term behavior. The time-temperature-stress superposition principle was also adopted to predict long-term creep performance, and the short-term experimental curves were extended to a large time scale as master curves. The

prediction methods make it possible to save a large amount of experimental work by using less data to forecast the future behavior of materials.

Outlook

In this work there no information regarding changing filler content, because a constant filler fraction of 1 vol % was used. It will be necessary to investigate the creep behaviors of composites filled with various filler concentrations, to obtain optimal combinations for practical applications.

To explain the mechanisms of nanofillers in enhancing the creep resistance of composites, a network model and load transfer effect were proposed for nanoparticles and nanotubes, respectively. However, creep-deformation-induced structure damage and evolution is very complex and depends on many factors, including filler dimension, stiffness and shape, dispersion and agglomerate size, time and stress level and temperature.

The presence of these factors and their interactions make it a challenging task to clearly understand their roles in the creep process. This indicates that further work is needed in future studies. In particular, it is suggested that the following issues are worthy of attention:

➢ The changes in the network formed by nanoparticles before and after creep experiments should be characterized to obtain direct evidence that particles can restrict the mobility of polymer chains.

➢ Single wall carbon nanotube composites should be considered, to compare the effect of intertube slip with that in multiwalled tubes.

The information obtained will yield a comprehensive understanding of the reinforcing effects of nanofillers on creep resistance and should offer an effective method for the design of creep resistant composites.

10   References

[1]   Findley, W.N., Lai, J.S. and Onaran, K.: Creep and relaxation of nonlinear viscoelastic materials, New York: Dover Publications, Inc 1989.

[2]   Ward, I.M.: Mechanical Properties of Solid Polymers, Chichester: John Wiley and Sons 1983.

[3]   Rabotnov, G.N. and Shesterikov, S.A.: Creep stability of columns and plates, Journal of the Mechanics and Physics of Solids 6 (1957), pp.27-34.

[4]   Johnson, A.F.: Creep characterization of transversely-isotropic metallic materials, Journal of the Mechanics and Physics of Solids 25 (1977), pp.117-126.

[5]   Nieman, G.W., Weertman, J.R. and Siegel, R.W.: Tensile-strength and creep-properties of nanocrystalline palladium, Scripta Metallurgica et Materialia 24 (1990), pp.145-150.

[6]   Hahn, H. and Averback, R.S.: Low-temperature creep of nanocrystalline Titanium(Iv) oxide, Journal of the American Ceramic Society 74 (1991), pp.2918-2921.

[7]   Herzer, G.: Creep Induced Magnetic-Anisotropy In Nanocrystalline Fe-Cu-Nb-Si-B Alloys, IEEE Transactions on Magnetics 30 (1994), pp.4800-4802.

[8]   Taneike, M., Abe, F. and Sawada, K.: Creep-strengthening of steel at high temperatures using nano-sized carbonitride dispersions, Nature 424 (2003), pp.294-296.

[9]   Yin, W.M. and Whang, S.H.: The creep and fracture in nanostructured metals and alloys, Journal of the Minerals, Metals & Materials Society 57 (2005), pp.63-70.

[10]   Betten, J.: Creep Mechanics, Berlin: Springer 2005.

[11]   Afrin, N. and Ngan, A.H.W.: Creep of micron-sized Ni3Al columns, Scripta Materialia 54 (2006), pp.7-12.

[12]   Sherby, O.D. and Dorn, J.E.: Anelastic creep of polymethyl methacrylate, Journal of the Mechanics and Physics of Solids 6 (1958), pp.145-162.

[13]   Turner, S.: Creep in thermoplastics-Polythene: Part I, British Plastics 9 (1964), pp.501-505.

[14]   Turner, S.: Creep in thermoplastics-Polythene: Part II, British Plastics 10 (1964), pp.567-568.

[15]   Turner, S.: Creep in thermoplastics-Unplasticized PVC, British Plastics 12 (1964), pp.682-685.

[16]   Turner, S.: Creep in thermoplastics-Nylon 66, British Plastics 1 (1965), pp.44-45.

[17]   Darlington, M.W.: Creep in Short Fiber Reinforced Thermoplastics, Journal of

Rheology 24 (1980), pp.902-902.

[18]   Trantina, G.G.: Creep analysis of polymer structures, Polymer Engineering and Science 26 (1986), pp.776-780.

[19]   Read, B.E., Dean, G.D. and Tomlins, P.E.: Effects of physical aging on creep in polypropylene, Polymer 29 (1988), pp.2159-2169.

[20]   Brinson, L.C. and Gates, T.S.: Effects of Physical Aging on Long-Term Creep of Polymers and Polymer Matrix Composites, International Journal of Solids and Structures 32 (1995), pp.827-846.

[21]   Scott, D.W., Lai, J.S. and Zureick, A.H.: Creep-behavior of fiber-reinforced polymeric composites - a review of the technical literature, Journal of Reinforced Plastics and Composites 14 (1995), pp.588-617.

[22]   Mills, N.J. and Gilcrist, A.: Creep and recovery of polyolefin foams - Deformation mechanisms, Journal of Cellular Plastics 33 (1997), pp.264-292.

[23]   Kolarik, J., Fambri, L., Pegoretti, A., Penati, A. and Goberti, P.: Prediction of the creep of heterogeneous polymer blends: Rubber-toughened polypropylene/poly(styrene-co-acrylonitrile), Polymer Engineering and Science 42 (2002), pp.161-169.

[24]   Smock, D.: Nanocomposites showing promise in automotive and packaging roles, Modern Plastics 75 (1998), pp.26-27.

[25]   Lee, A. and Lichtenhan, J.D.: Thermal and viscoelastic property of epoxy-clay and hybrid inorganic-organic epoxy nanocomposites, Journal of Applied Polymer Science 73 (1999), pp.1993-2001.

[26]   Garces, J.M., Moll, D.J., Bicerano, J., Fibiger, R. and McLeod, D.G.: Polymeric nanocomposites for automotive applications, Advanced Materials 12 (2000), pp.1835-1839.

[27]   Peigney, A., Laurent, C., Flahaut, E. and Rousset, A.: Carbon nanotubes in novel ceramic matrix nanocomposites, Ceramics International 26 (2000), pp.677-683.

[28]   Pinnavaia, T.J. and Beall, G.W.: Polymer clay nanocomposites, New York: John Wiley and Sons 2001.

[29]   Dufresne, A., Paillet, M., Putaux, J.L., Canet, R., Carmona, F., Delhaes, P. and Cui, S.: Processing and characterization of carbon nanotube/poly(styrene-co-butyl acrylate) nanocomposites, Journal of Materials Science 37 (2002), pp.3915-3923.

[30]   Lepoittevin, B., Devalckenaere, M., Pantoustier, N., Alexandre, M., Kubies, D., Calberg, C., Jerome, R. and Dubois, P.: Poly(epsilon-caprolactone)/clay nanocomposites prepared by melt intercalation: mechanical, thermal and rheological properties, Polymer 43 (2002), pp.4017-4023.

[31]   Ajayan, P.M., Schadler, L.S. and Braun, P.V.: Nanocomposite science and technology, Weinheim: Wiley-VCH 2003.

[32]   Gong, Q.-m., Li, Z., Li, D., Bai, X.-d. and Liang, J.: Fabrication and structure: a study of aligned carbon nanotube/carbon nanocomposites, Solid State Communications 131 (2004), pp.399-404.

[33]   Peeterbroeck, S., Alexandre, M., Nagy, J.B., Pirlot, C., Fonseca, A., Moreau, N., Philippin, G., Delhalle, J., Mekhalif, Z. and Sporken, R.: Polymer-layered silicate-carbon nanotube nanocomposites: unique nanofiller synergistic effect, Composites Science and Technology 64 (2004), pp.2317-2323.

[34]   Broza, G., Kwiatkowska, M., Roslaniec, Z. and Schulte, K.: Processing and assessment of poly(butylene terephthalate) nanocomposites reinforced with oxidized single wall carbon nanotubes, Polymer 46 (2005), pp.5860-5867.

[35]   Hong, C.H., Lee, Y.B., Bae, J.W., Jho, J.Y., Nam, B.U. and Hwang, T.W.: Performance of polypropylene/clay nanocomposites for automotive parts applications, Journal of Industrial and Engineering Chemistry 11 (2005), pp.76-82.

[36]   Kashiwagi, T., Du, F.M., Winey, K.I., Groth, K.A., Shields, J.R., Bellayer, S.P., Kim, H. and Douglas, J.F.: Flammability properties of polymer nanocomposites with single-walled carbon nanotubes: effects of nanotube dispersion and concentration, Polymer 46 (2005), pp.471-481.

[37]   Lee, L.J., Zeng, C., Cao, X., Han, X., Shen, J. and Xu, G.: Polymer nanocomposite foams, Composites Science and Technology 65 (2005), pp.2344-2363.

[38]   Shan, Y. and Gao, L.: Synthesis and characterization of phase controllable ZrO2-carbon nanotube nanocomposites, Nanotechnology 16 (2005), pp.625-630.

[39]   Nicolais, L. and Carotenuto, G.: Metal-Polymer Nanocomposites, Hoboken: John Wiley and Sons 2005.

[40]   Wu, D.F., Zhou, C.X., Yu, W. and Xie, F.: Effect of blending sequence on the morphologies of poly(butylene terephthalate)/epoxy/clay nanocomposites by a rheological approach, Journal of Applied Polymer Science 99 (2006), pp.340-346.

[41]   Bueche, A.M.: Filler Reinforcement of Silicone Rubber, Journal of Polymer Science 25 (1957), pp.139-149.

[42]   Sumita, M., Tsukumo, Y., Miyasaka, K. and Ishikawa, K.: Tensile Yield Stress of Polypropylene Composites Filled with Ultrafine Particles, Journal of Materials Science 18 (1983), pp.1758-1764.

[43]   Iljima, S.: Helical microtubles of graphitic carbon, Nature 354 (1991), pp.56-58.

[44]   Ren, Z.F., Huang, Z.P., Xu, J.W., Wang, J.H., Bush, P., Siegal, M.P. and Provencio, P.N.: Synthesis of Large Arrays of Well-Aligned Carbon Nanotubes on Glass, Science 282 (1998), pp.1105-1107.

[45]   Lambert, J.M., Bernier, P. and Ajayan, P.M.: Synthesis of single and multi-

shell carbon nanotubes, Synthetic Metals 70 (1995), pp.1475-1476.

[46]   Shi, Z., Zhou, X., Jin, Z., Gu, Z., Wang, J., Feng, S., Xu, X. and Liu, Z.: High yield synthesis and growth mechanism of carbon nanotubes, Solid State Communications 97 (1996), pp.371-375.

[47]   Kokai, F., Takahashi, K., Kasuya, D., Ichihashi, T., Yudasaka, M. and Iijima, S.: Synthesis of single-wall carbon nanotubes by millisecond-pulsed CO_2 laser vaporization at room temperature, Chemical Physics Letters 332 (2000), pp.449-454.

[48]   Li, W.Z., Xie, S.S., Qian, L.X., Chang, B.H., Zou, B.S., Zhou, W.Y., Zhao, R.A. and Wang, G.: Large-Scale Synthesis of Aligned Carbon Nanotubes, Science 274 (1996), pp.1701-1703.

[49]   Zhu, H.W., Xu, C.L., Wu, D.H., Wei, B.Q., Vajtai, R. and Ajayan, P.M.: Direct synthesis of long single-walled carbon nanotube strands, Science 296 (2002), pp.884-886.

[50]   Zhang, Z., Dewan, C., Kothari, S., Mitra, S. and Teeters, D.: Carbon nanotube synthesis, characteristics, and microbattery applications, Materials Science and Engineering B 116 (2005), pp.363-368.

[51]   Goze, C., Bernier, P., Henrard, L., Vaccarini, L., Hernandez, E. and Rubio, A.: Elastic and mechanical properties of carbon nanotubes, Synthetic Metals 103 (1999), pp.2500-2501.

[52]   Ebbesen, T.W.: Carbon Nanotubes, Annual Review of Materials Science 24 (1994), pp.235-264.

[53]   Treacy, M.M.J., Ebbesen, T.W. and Gibson, J.M.: Exceptionally high Young's modulus observed for individual carbon nanotubes, Nature 381 (1996), pp.678-680.

[54]   Falvo, M.R., Clary, G.J., Taylor, R.M., Chi, V., Brooks, F.P., Washburn, S. and Superfine, R.: Bending and buckling of carbon nanotubes under large strain, Nature 389 (1997), pp.582-584.

[55]   Salvetat, J.P., Bonard, J.M., Thomson, N.H., Kulik, A.J., Forro, L., Benoit, W. and Zuppiroli, L.: Mechanical properties of carbon nanotubes, Applied Physics A-Materials Science and Processing 69 (1999), pp.255-260.

[56]   Walters, D.A., Ericson, L.M., Casavant, M.J., Liu, J., Colbert, D.T., Smith, K.A. and Smalley, R.E.: Elastic strain of freely suspended single-wall carbon nanotube ropes, Applied Physics Letters 74 (1999), pp.3803-3805.

[57]   Salvetat, J.P., Kulik, A.J., Bonard, J.M., Briggs, G.A.D., Stockli, T., Metenier, K., Bonnamy, S., Beguin, F., Burnham, N.A. and Forro, L.: Elastic modulus of ordered and disordered multiwalled carbon nanotubes, Advanced Materials 11 (1999), pp.161-165.

[58]   Ruoff, R.S. and Lorents, D.C.: Mechanical and thermal properties of carbon nanotubes, Carbon 33 (1995), pp.925-930.

[59]   Roche, S.: Carbon nanotubes: Exceptional mechanical and electronic properties, Annales de Chimie Science des Materiaux 25 (2000), pp.529-532.

[60]   Xie, S.S., Li, W.Z., Pan, Z.W., Chang, B.H. and Sun, L.F.: Mechanical and physical properties on carbon nanotube, Journal of Physics and Chemistry of Solids 61 (2000), pp.1153-1158.

[61]   Forro, L. and Schonenberger, C.: Physical properties of multi-wall nanotubes. Carbon Nanotubes Topics in Applied Physics 80 (2001), pp. 329-390.

[62]   Li, Y.H., Wei, J.Q., Zhang, X.F., Xu, C.L., Wu, D.H., Lu, L. and Wei, B.Q.: Mechanical and electrical properties of carbon nanotube ribbons, Chemical Physics Letters 365 (2002), pp.95-100.

[63]   Qian, D., Wagner, G.J., Liu, W.K., Yu, M.-F. and Ruoff, R.S.: Mechanics of carbon nanotubes, Applied Mechanics Reviews 55 (2002), pp.495-533.

[64]   Xia, Y.Y., Zhao, M.W., Ma, Y.C., Ying, M.J., Liu, X.D., Liu, P.J. and Mei, L.M.: Tensile strength of single-walled carbon nanotubes with defects under hydrostatic pressure, Physical Review B 65 (2002), Art. No. 155415.

[65]   Qi, H.J., Teo, K.B.K., Lau, K.K.S., Boyce, M.C., Milne, W.I., Robertson, J. and Gleason, K.K.: Determination of mechanical properties of carbon nanotubes and vertically aligned carbon nanotube forests using nanoindentation, Journal of the Mechanics and Physics of Solids 51 (2003), pp.2213-2237.

[66]   Qu, L.W., Lin, Y., Hill, D.E., Zhou, B., Wang, W., Sun, X.F., Kitaygorodskiy, A., Suarez, M., Connell, J.W., Allard, L.F. and Sun, Y.P.: Polyimide-functionalized carbon nanotubes: Synthesis and dispersion in nanocomposite films, Macromolecules 37 (2004), pp.6055-6060.

[67]   Wang, Y. and Lee, W.C.: Interfacial interactions in calcium carbonate-polypropylene composites. 2: Effect of compounding on the dispersion and the impact properties of surface-modified composites, Polymer Composites 25 (2004), pp.451-460.

[68]   Causin, V., Marega, C., Marigo, A. and Ferrara, G.: Assessing organo-clay dispersion in polymer layered silicate nanocomposites: A SAXS approach, Polymer 46 (2005), pp.9533-9537.

[69]   Song, Y.S. and Youn, J.R.: Influence of dispersion states of carbon nanotubes on physical properties of epoxy nanocomposites, Carbon 43 (2005), pp.1378-1385.

[70]   Kodgire, P., Kalgaonkar, R., Hambir, S., Bulakh, N. and Jog, J.P.: PP/clay nanocomposites: Effect of clay treatment on morphology and dynamic mechanical properties, Journal of Applied Polymer Science 81 (2001), pp.1786-1792.

[71]   Wu, C.L., Zhang, M.Q., Rong, M.Z. and Friedrich, K.: Silica nanoparticles filled polypropylene: effects of particle surface treatment, matrix ductility and particle species on mechanical performance of the composites, Composites

Science and Technology 65 (2005), pp.635-645.

[72]   Noguchi, T., Magario, A., Fukazawa, S., Shimizu, S., Beppu, J. and Seki, M.: Carbon nanotube/aluminium composites with uniform dispersion, Materials Transactions 45 (2004), pp.602-604.

[73]   Zheng, H., Zhang, Y., Peng, Z.L. and Zhang, Y.X.: Influence of clay modification on the structure and mechanical properties of EPDM/montmorillonite nanocomposites, Polymer Testing 23 (2004), pp.217-223.

[74]   Oberdisse, J., El Harrak, A., Carrot, G., Jestin, J. and Boue, F.: Structure and rheological properties of soft-hard nanocomposites: influence of aggregation and interfacial modification, Polymer 46 (2005), pp.6695-6705.

[75]   Zhao, J., Schaefer, D.W., Shi, D.L., Lian, J., Brown, J., Beaucage, G., Wang, L.M. and Ewing, R.C.: How does surface modification aid in the dispersion of carbon nanofibers?, Journal of Physical Chemistry B 109 (2005), pp.23351-23357.

[76]   Park, C., Ounaies, Z., Watson, K.A., Crooks, R.E., Smith, J., Lowther, S.E., Connell, J.W., Siochi, E.J., Harrison, J.S. and Clair, T.L.S.: Dispersion of single wall carbon nanotubes by in situ polymerization under sonication, Chemical Physics Letters 364 (2002), pp.303-308.

[77]   Goh, H.W., Goh, S.H., Xu, G.Q., Pramoda, K.P. and Zhang, W.D.: Dynamic mechanical behavior of in situ functionalized multi-walled carbon nanotube/phenoxy resin composite, Chemical Physics Letters 373 (2003), pp.277-283.

[78]   Tung, J., Gupta, R.K., Simon, G.P., Edward, G.H. and Bhattacharya, S.N.: Rheological and mechanical comparative study of in situ polymerized and melt-blended nylon 6 nanocomposites, Polymer 46 (2005), pp.10405-10418.

[79]   Zhao, C., Hu, G., Justice, R., Schaefer, D.W., Zhang, S., Yang, M. and Han, C.C.: Synthesis and characterization of multi-walled carbon nanotubes reinforced polyamide 6 via in situ polymerization, Polymer 46 (2005), pp.5125-5132.

[80]   Park, S.-J., Jeong, H.-J. and Nah, C.: A study of oxyfluorination of multi-walled carbon nanotubes on mechanical interfacial properties of epoxy matrix nanocomposites, Materials Science and Engineering A 385 (2004), pp.13-16.

[81]   Pecastaings, G., Delhaes, P., Derre, A., Saadaoui, H., Carmona, F. and Cui, S.: Role of interfacial effects in carbon nanotube/epoxy nanocomposite behavior, Journal of Nanoscience and Nanotechnology 4 (2004), pp.838-843.

[82]   Wang, M., Pramoda, K.P. and Goh, S.H.: Enhancement of interfacial adhesion and dynamic mechanical properties of poly(methyl methacrylate)/multiwalled carbon nanotube composites with amine-terminated poly(ethylene oxide), Carbon 44 (2006), pp.613-617.

[83]   Shah, D., Maiti, P., Jiang, D.D., Batt, C.A. and Giannelis, E.P.: Effect of nanoparticle mobility on toughness of polymer nanocomposites, Advanced Materials 17 (2005), pp.525-528.

[84]   Yang, J.-L., Zhang, Z. and Zhang, H.: The essential work of fracture of polyamide 66 filled with TiO2 nanoparticles, Composites Science and Technology 65 (2005), pp.2374-2379.

[85]   Zhang, H., Zhang, Z., Yang, J.-L. and Friedrich, K.: Temperature dependence of crack initiation fracture toughness of various nanoparticles filled polyamide 66, Polymer 47 (2006), pp.679-689.

[86]   Bohning, M., Goering, H., Hao, N., Mach, R. and Schonhals, A.: Polycarbonate/SiC nanocomposites - influence of nanoparticle dispersion on molecular mobility and gas transport, Polymers for Advanced Technologies 16 (2005), pp.262-268.

[87]   Zhang, Z., Yang, J.-L. and Friedrich, K.: Creep resistant polymeric nanocomposites, Polymer 45 (2004), pp.3481-3485.

[88]   Yang, J.-L., Zhang, Z., Schlarb, A.K. and Friedrich, K.: On the characterization of tensile creep resistance of polyamide 66 nanocomposites. Part I. Experimental results and general discussions, Polymer (2006), pp.2794-2804.

[89]   Kim, J.-K. and Mai, Y.-W.: Engineered interfaces in fiber reinforced composites, Oxford: Elsevier Science Ltd 1998.

[90]   Yoshihara, T.: Dispersion of surface-modified ultrafine particles by use of hydrophobic monomers, International Journal of Adhesion and Adhesives 19 (1999), pp.353-357.

[91]   Zhu, F., Zhang, J., Yang, Z.X., Guo, Y., Li, H. and Zhang, Y.F.: The dispersion study of TiO2 nanoparticles surface modified through plasma polymerization, Physica E-Low-Dimensional Systems and Nanostructures 27 (2005), pp.457-461.

[92]   Dai, H.J.: Carbon nanotubes: opportunities and challenges, Surface Science 500 (2002), pp.218-241.

[93]   Popov, V.N.: Carbon nanotubes: properties and application, Materials Science and Engineering R-Reports 43 (2004), pp.61-102.

[94]   Pantano, A., Parks, D.M. and Boyce, M.C.: Mechanics of deformation of single- and multi-wall carbon nanotubes, Journal of the Mechanics and Physics of Solids 52 (2004), pp.789-821.

[95]   Harris, B.: Fatigue in composites - science and technology of the fatigue response of fibre-reinforced plastics, Cambridge: CRC Press 2003.

[96]   Lazzeri, A., Zebarjad, S.M., Pracella, M., Cavalier, K. and Rosa, R.: Filler toughening of plastics. Part 1 - The effect of surface interactions on physico-mechanical properties and rheological behaviour of ultrafine CaCO3/HDPE nanocomposites, Polymer 46 (2005), pp.827-844.

[97]   Chae, D.W., Lee, K.H. and Kim, Y.C.: Rheological properties of ferrite nanocomposites based on nylon-66, Journal of Polymer Science Part B-Polymer Physics 44 (2006), pp.371-377.

[98]   Sarvestani, A.S. and Picu, C.R.: Network model for the viscoelastic behavior of polymer nanocomposites, Polymer 45 (2004), pp.7779-7790.

[99]   Galgali, G., Ramesh, C. and Lele, A.: A rheological study on the kinetics of hybrid formation in polypropylene nanocomposites, Macromolecules 34 (2001), pp.852-858.

[100]   Pegoretti, A. and Penati, A.: Recycled poly(ethylene terephthalate) and its short glass fibres composites: effects of hygrothermal aging on the thermo-mechanical behaviour, Polymer 45 (2004), pp.7995-8004.

[101]   Ranade, A., Nayak, K., Fairbrother, D. and D'Souza, N.A.: Maleated and non-maleated polyethylene-montmorillonite layered silicate blown films: creep, dispersion and crystallinity, Polymer 46 (2005), pp.7323-7333.

[102]   Vlasveld, D.P.N., Bersee, H.E.N. and Picken, S.J.: Creep and physical aging behaviour of PA6 nanocomposites, Polymer 46 (2005), pp.12539-12545.

[103]   Blackwell, R.I. and Mauritz, K.A.: Mechanical creep and recovery of poly(styrene-b-ethylene/butylene-b-styrene)(SEBS), sulfonated SEBS (sSEBS), and sSEBS/siticate nanostructured materials, Polymers for Advanced Technologies 16 (2005), pp.212-220.

[104]   Gong, X.Y., Liu, J., Baskaran, S., Voise, R.D. and Young, J.S.: Surfactant-assisted processing of carbon nanotube/polymer composites, Chemistry of Materials 12 (2000), pp.1049-1052.

[105]   Jin, Z., Pramoda, K.P., Xu, G. and Goh, S.H.: Dynamic mechanical behavior of melt-processed multi-walled carbon nanotube/poly(methyl methacrylate) composites, Chemical Physics Letters 337 (2001), pp.43-47.

[106]   Fisher, F.T., Eitan, A., Andrews, R., Schadler, L.S. and Brinson, L.C.: Spectral response and effective viscoelastic properties of MWNT-reinforced polycarbonate, Advanced Composites Letters 13 (2004), pp.105-111.

[107]   Suhr, J., Koratkar, N., Keblinski, P. and Ajayan, P.: Viscoelasticity in carbon nanotube composites, Nature Materials 4 (2005), pp.134-137.

[108]   Velasco-Santos, C., Martinez-Hernandez, A.L. and Castano, V.M.: Carbon nanotube-polymer nanocomposites: The role of interfaces, Composite Interfaces 11 (2005), pp.567-586.

[109]   Thostenson, E.T., Ren, Z. and Chou, T.-W.: Advances in the science and technology of carbon nanotubes and their composites: a review, Composites Science and Technology 61 (2001), pp.1899-1912.

[110]   Schadler, L.S., Giannaris, S.C. and Ajayan, P.M.: Load transfer in carbon nanotube epoxy composites, Applied Physics Letters 73 (1998), pp.3842-3844.

[111] Qian, D., Dickey, E.C., Andrews, R. and Rantell, T.: Load transfer and deformation mechanisms in carbon nanotube-polystyrene composites, Applied Physics Letters 76 (2000), pp.2868-2870.

[112] Qian, D., Liu, W.K. and Ruoff, R.S.: Load transfer mechanism in carbon nanotube ropes, Composites Science and Technology 63 (2003), pp.1561-1569.

[113] Gou, J.H., Liang, Z.Y., Zhang, C. and Wang, B.: Computational analysis of effect of single-walled carbon nanotube rope on molecular interaction and load transfer of nanocomposites, Composites Part B-Engineering 36 (2005), pp.524-533.

[114] Zhang, Y.C. and Wang, X.: Thermal effects on interfacial stress transfer characteristics of carbon nanotubes/polymer composites, International Journal of Solids and Structures 42 (2005), pp.5399-5412.

[115] Barber, A.H., Cohen, S.R. and Wagner, H.D.: Measurement of carbon nanotube-polymer interfacial strength, Applied Physics Letters 82 (2003), pp.4140-4142.

[116] Velasco-Santos, C., Martinez-Hernandez, A.L., Fisher, F.T., Ruoff, R. and Castano, V.M.: Improvement of thermal and mechanical properties of carbon nanotube composites through chemical functionalization, Chemistry of Materials 15 (2003), pp.4470-4475.

[117] Pham, J.Q., Mitchell, C.A., Bahr, J.L., Tour, J.M., Krishanamoorti, R. and Green, P.F.: Glass transition of polymer/single-walled carbon nanotube composite films, Journal of Polymer Science Part B-Polymer Physics 41 (2003), pp.3339-3345.

[118] Ogasawara, T., Ishida, Y., Ishikawa, T. and Yokota, R.: Characterization of multi-walled carbon nanotube/phenylethynyl terminated polyimide composites, Composites Part A-Applied Science and Manufacturing 35 (2004), pp.67-74.

[119] Sreekumar, T.V., Liu, T., Min, B.G., Guo, H., Kumar, S., Hauge, R.H. and Smalley, R.E.: Polyacrylonitrile single-walled carbon nanotube composite fibers, Advanced Materials 16 (2004), pp.58-61.

[120] Barrau, S., Demont, P., Maraval, C., Bernes, A. and Lacabanne, C.: Glass transition temperature depression at the percolation threshold in carbon nanotube-epoxy resin and polypyrrole-epoxy resin composites, Macromolecular Rapid Communications 26 (2005), pp.390-394.

[121] Bhattacharyya, S., Sinturel, C., Salvetat, J.P. and Saboungi, M.L.: Protein-functionalized carbon nanotube-polymer composites, Applied Physics Letters 86 (2005), Art. No. 113104.

[122] Guo, H., Sreekumar, T.V., Liu, T., Minus, M. and Kumar, S.: Structure and properties of polyacrylonitrile/single wall carbon nanotube composite films, Polymer 46 (2005), pp.3001-3005.

[123] Kwon, J.Y. and Kim, H.D.: Preparation and properties of acid-treated multiwalled carbon nanotube/waterborne polyurethane nanocomposites, Journal of Applied Polymer Science 96 (2005), pp.595-604.

[124] Suhr, J., Zhang, W., Ajayan, P.M. and Koratkar, N.A.: Temperature-activated interfacial friction damping in carbon nanotube polymer composites, Nano Letters 6 (2006), pp.219-223.

[125] Suhr, J. and Koratkar, N.: Effect of pre-strain on interfacial friction damping in carbon nanotube polymer composites, Journal of Nanoscience and Nanotechnology 6 (2006), pp.483-486.

[126] Lourie, O. and Wagner, H.D.: Evidence of stress transfer and formation of fracture clusters in carbon nanotube-based composites, Composites Science and Technology 59 (1999), pp.975-977.

[127] Qian, D. and Dickey, E.C.: In-situ transmission electron microscopy studies of polymer-carbon nanotube composite deformation, Journal of Microscopy 204 (2001), pp.39-45.

[128] Liao, K. and Li, S.: Interfacial characteristics of a carbon nanotube-polystyrene composite system, Applied Physics Letters 79 (2001), pp.4225-4227.

[129] Xu, X.J., Thwe, M.M., Shearwood, C. and Liao, K.: Mechanical properties and interfacial characteristics of carbon-nanotube-reinforced epoxy thin films, Applied Physics Letters 81 (2002), pp.2833-2835.

[130] Wong, M., Paramsothy, M., Xu, X.J., Ren, Y., Li, S. and Liao, K.: Physical interactions at carbon nanotube-polymer interface, Polymer 44 (2003), pp.7757-7764.

[131] Lau, K.T.: Interfacial bonding characteristics of nanotube/polymer composites, Chemical Physics Letters 370 (2003), pp.399-405.

[132] Namilae, S. and Chandra, N.: Multiscale model to study the effect of interfaces in carbon nanotube-based composites, Journal of Engineering Materials and Technology-Transactions of the ASME 127 (2005), pp.222-232.

[133] Ma, J., Yu, Z.Z., Kuan, H.C., Dasari, A. and Mai, Y.W.: A new strategy to exfoliate silicone rubber/clay nanocomposites, Macromolecular Rapid Communications 26 (2005), pp.830-833.

[134] Yu, M.-F., Lourie, O., Dyer, M.J., Moloni, K., Kelly, T.F. and Ruoff, R.S.: Strength and breaking mechanism of multiwalled carbon nanotubes under tensile load, Science 287 (2000), pp.637-640.

[135] Aklonis, J.J. and MacKnight, W.J.: Introduction to polymer viscoelasticity, New York: John Wiley and Sons 1983.

[136] Marais, C. and Villoutreix, G.: Analysis and modeling of the creep behavior of the thermostable PMR-15 polyimide, Journal of Applied Polymer Science 69 (1998), pp.1983-1991.

[137] Adalja, S.B. and Otaigbe, J.U.: Creep and recovery behavior of novel organic-inorganic polymer hybrids, Polymer Composites 23 (2002), pp.171-181.

[138] Nunez, A.J., Marcovich, N.E. and Aranguren, M.I.: Analysis of the creep behavior of polypropylene-woodflour composites, Polymer Engineering and Science 44 (2004), pp.1594-1603.

[139] McClure, G. and Mohammadi, Y.: Compression Creep of Pultruded E-Glass-Reinforced-Plastic Angles, Journal of Materials in Civil Engineering 7 (1995), pp.269-276.

[140] Knox, E.M., Cowling, M.J. and Hashim, S.A.: Creep analysis of adhesively bonded connections in GRE pipes including the effect of defects, Composites Part A-Applied Science and Manufacturing 31 (2000), pp.583-590.

[141] Choi, Y. and Yuan, R.L.: Time-dependent deformation of pultruded fiber reinforced polymer composite columns, Journal of Composites for Construction 7 (2003), pp.356-362.

[142] Shao, Y.X. and Shanmugam, J.: Deflection creep of pultruded composite sheet piling, Journal of Composites for Construction 8 (2004), pp.471-479.

[143] Phanthien, N.: Time-temperature superposition principle of dilute polymer liquids, Journal of Rheology 23 (1979), pp.451-456.

[144] Kitagawa, M. and Matsutani, T.: Effect of time and temperature on nonlinear constitutive equation in polypropylene, Journal of Materials Science 23 (1988), pp.4085-4090.

[145] Han, C.D. and Kim, J.K.: On the use of time-temperature superposition in multicomponent multiphase polymer systems, Polymer 34 (1993), pp.2533-2539.

[146] Oconnell, P.A. and McKenna, G.B.: Large deformation response of polycarbonate: Time-temperature, time-aging time, and time-strain superposition, Polymer Engineering and Science 37 (1997), pp.1485-1495.

[147] Li, R.Z.: Time-temperature superposition method for glass transition temperature of plastic materials, Materials Science and Engineering A-Structural Materials Properties Microstructure and Processing 278 (2000), pp.36-45.

[148] Tajvidi, M., Falk, R.H. and Hermanson, J.C.: Time-temperature superposition principle applied to a kenaf-fiber/high-density polyethylene composite, Journal of Applied Polymer Science 97 (2005), pp.1995-2004.

[149] Wortmann, F.J. and Schulz, K.V.: Stress-relaxation and time-temperature superposition of polypropylene fibers, Polymer 36 (1995), pp.315-321.

[150] Brostow, W.: Time-stress correspondence in viscoelastic materials: an equation for the stress and temperature shift factor, Materials Research Innovations 3 (2000), pp.347-351.

[151] Jazouli, S., Luo, W.B., Bremand, F. and Vu-Khanh, T.: Application of time-

stress equivalence to nonlinear creep of polycarbonate, Polymer Testing 24 (2005), pp.463-467.

[152]   Kolarik, J.: Tensile creep of thermoplastics: Time-strain superposition of non-iso free-volume data, Journal of Polymer Science Part B-Polymer Physics 41 (2003), pp.736-748.

[153]   Kolarik, J. and Pegoretti, A.: Non-linear tensile creep of polypropylene: Time-strain superposition and creep prediction, Polymer 47 (2006), pp.346-356.

[154]   Zheng, G.F., Kang, Y.L., Sheng, J., Qin, Q.H., Wang, H.W. and Fu, D.H.: Influence of moisture content and time on the mechanical behavior of polymer material, Science in China Series E-Engineering and Materials Science 47 (2004), pp.595-607.

[155]   Fujieda, H., Sekine, N., Nakada, M., Miyano, Y., Kuraishi, A. and Tsai, S.W.: Applicability of time-temperature-water absorption superposition principle for flexural strength of CFRP laminates, Jsme International Journal Series a-Solid Mechanics and Material Engineering 46 (2003), pp.467-472.

[156]   DIN EN ISO 527-2. Determination of tensile properties - Part 2: Test conditions for moulding and extrusion plastics. Berlin: Deutsches Insitut fuer Normung 1996.

[157]   ASTM D 2990-01. Standard test methods for tensile, compressive, and flexural creep and creep-rupture of plastics. West Conshohocken: ASTM International 2001.

[158]   Williams, M. L., Landel, R. F., Ferry, J. D.: The temperature dependence of relaxation mechanisms in amorphous polymers and other glass-forming liquids. Journal of the American Chemical Society 77(1955), pp.3701-3707.

[159]   Luo, W. B., Yang, T. Q., An, Q. L.: Time-temperature-stress equivalence and its application to nonlinear viscoelastic materials. Acta Mechanica Solida Sinica 14 (2001), pp.195-199.

[160]   van Dommelen, J. A. W, Parks, D. M., Boyce, M. C., Brekelmans. W. A. M., Baaijens, F. P. T.: Micromechanical modeling of the elasto-viscoplastic behavior of semi-crystalline polymers. Journal of Mechanics and Physics of Solids 51 (2003), pp.519-541.

[161]   Harren, S. V.: Toward a new phenomenological flow rule for orientationally hardening glassy-polymers. Journal of Mechanics and Physics of Solids 43 (1995), pp.1151-1173.

[162]   Zhang, H., Zhang, Z., Yang, J. –L., and Friedrich, K.: Temperature dependence of crack initiation fracture toughness for polyamide nanocomposites. Polymer 47 (2006), pp.679-689.

[163]   Brechet, Y., Cavaille, J. Y. Y., Chabert, E., Chazeau, L., Dendievel, R., Flandin, L., and Gauthier, C.: Polymer based nanocomposites: Effect of filler-filler and filler-matrix interactions. Advanced Engineering Materials 3 (2001),

pp.571-577.

[164] Aktas L, Hamidi YK, Altan MC. Characterisation of nanoclay dispersion in resin transfer moulded glass/nanoclay/epoxy composites. Plastics, Rubber and Composites 33 (2004), pp.267-272.

[165] Davy, P. J., and Guild, F. J.: The distribution of interparticle distance and its application in finite-element modeling of composite-materials. Proceedings of the Royal Society of London Series a-Mathematical Physical and Engineering Sciences 418 (1988), pp.95-112.

[166] Berlyand, L., and Kolpakov, A.: Network approximation in the limit of small interparticle distance of the effective properties of a high-contrast random dispersed composite. Archive for Rational Mechanics and Analysis 159 (2001), pp.179-227.

[167] Sweeney, J., and Ward, I. M.: A constitutive law for large deformations of polymers at high temperatures. Journal of Mechanics and Physics of Solids 44 (1996), pp.1033-1049.

[168] Harren, S. V.: A yield surface and flow rule for orientationally hardening polymers subjected to arbitrary deformations. Journal of Mechanics and Physics of Solids 45 (1997), pp.1-20.

[169] Wilding, M. A., and Ward, I. M.: Tensile creep and recovery in ultrahigh modulus linear polyethylenes. Polymer 19 (1978), pp.969-976.

[170] Wilding, M. A., and Ward, I. M.: Creep and recovery of ultra high modulus polyethylene. Polymer 22 (1981), pp.870-876.

[171] Yu, M. F., Yakobson, B. I., and Ruoff, R. S.: Controlled sliding and pullout of nested shells in individual multiwalled carbon nanotubes. The Journal of Physical Chemistry B 104 (2000), pp.8764-8767.

[172] Wagner, H. D., Lourie, O., Feldman, Y. and Tenne, R.: Stress-induced fragmentation of multiwall carbon nanotubes in a polymer matrix. Applied Physics Letter 72 (1998), pp.188-190.

[173] User's manual of creep rupture test machine - Model 2002. Dortmund: COESFELD GmbH and Co. KG 2002.

List of Publications

A. Refereed journal papers

1. Yang, J.L., Zhang, Z., Schlarb, A. and Friedrich, K.: "Creep resistance of polymer nanocomposites reinforced with multiwalled carbon nanotubes", submitted to Macromolecular Rapid Communications.

2. Starkova, O., Yang, J.L., Zhang, Z.: "Modeling of long-term creep of polyamide 66 filled with various size nanoparticles", submitted to Composite Science and Technology.

3. Lietz, S., Yang, J.L., Bosch, E., Sandler, J.K.W., Zhang, Z. and Altstaedt. V.: "Improvement of the mechanical properties and creep resistance of poly(styrene-b-butadiene-b-styrene) block copolymers by nanoclay fillers", Macromolecular Materials and Engineering 292(1), 23-32 (2007).

4. Yang, J.L., Zhang, Z., Schlarb, A. and Friedrich, K.: "On the characterization of tensile creep resistance of polymer nanocomposites. Part II: Modeling and prediction of long-term performance", Polymer 47(19), 6745-6758 (2006).

5. Yang, J.L., Zhang, Z., Schlarb, A. and Friedrich, K.: "On the characterization of tensile creep resistance of polymer nanocomposites. Part I: Experimental results and general discussions", Polymer 47(8), 2794-2804 (2006).

6. Zhang, H., Zhang, Z., Yang, J.L.: "Temperature dependence of crack initiation fracture toughness for polyamide nanocomposites", Polymer, 47(2), 679-689 (2006).

7. Yang, J.L., Zhang, Z., Zhang, H.: "The essential work of fracture of polyamide 66 filled with TiO_2 nanoparticles", Composite Science and Technology, 65(15-16), 2374-2379 (2005)

8. Zhang, Z., Yang, J.L., Friedrich, K.: "Creep resistant polymeric nanocomposites", Polymer, 45(10), 3481-3485 (2004).

9. Hu, X.F., Yang, J.L., Wu, X.P., et al. "A study on the damage evolution of internal structure for Bi-2223/Ag HTS tapes", Journal of Experimental Mechanics (Chinese) 19, 67-71 (2004).

10. Yang, J.L., Hu, X.F., Wu, X.P.: "Experiments on fiber optic displacement sensor for cryogenic environment", Journal of Experimental Mechanics (Chinese) 17, 55-61 (2002).

B.   Conference presentations and proceedings

11. Yang, J.L., Zhang, Z., Friedrich, K.: Tensile Creep Behaviour of Nanoparticle Filled PA66 under Different Loads and Elevated Temperatures, in *China International Conference on Nanoscience and Technology (ChinaNano2005)*, Beijing, China, June 9-11, 2005.

12. Zhang, Z., Yang, J.L., Zhang, H., Friedrich, K.: Fatigue crack propagation of inorganic nanoparticle filled polyamide 6,6, in the *11th International Conference on Fracture*, Turin, Italy, March 20-25, 2005.

13. Yang, J.L., Zhang, Z., Zhang, H.: The work-of-fracture of TiO_2 nanoparticle filled polyamide 6,6, in the *International Symposium on Engineering Plastics (EP'2004)*, Lanzhou, China, August 15-20, 2004.

14. Yang, J.L., Zhang, Z., Zhang, H.: The fracture work of polyamide 6,6 filled with TiO_2 nanoparticles, in *EUROPE-CHINA SYMPOSIUM on Reinforced Polymers*, CD-ROM edited by C. G'Sell and S.-L. Bai. (Apollor Association, Nancy, 2004)

15. Yang, J.L., Hu, X.F., Wu, X.P.: Experimental study of the test system for HTS Bi2223/Ag tapes under tension, in *The 3rd International Conference on Experimental Mechanics,* edited by X.P. Wu et al. (Proceedings of SPIE Vol. 4537, Beijing 2002), pp.143.

16. Hu, X.F., Yang, J.L., Jiang, Z.Y.: Investigation on internal microstructure and damage evolution in Bi-2223/Ag HTS tapes by synchrotron radiation, in *The 3rd International Conference on Experimental Mechanics,* edited by X.P. Wu et al. (Proceedings of SPIE Vol. 4537, Beijing 2002), pp.237.